



**DEVELOPMENT OF OPTICAL PHASE EVALUATION
TECHNIQUES: APPLICATION TO FRINGE PROJECTION
AND DIGITAL SPECKLE MEASUREMENT**

BY

CHEN LUJIE

(B. Eng.)

**A THESIS SUBMITTED
FOR THE DEGREE OF DOCTOR OF PHILOSOPHY
DEPARTMENT OF MECHANICAL ENGINEERING
NATIONAL UNIVERSITY OF SINGAPORE**

2005

ACKNOWLEDGEMENTS

The author would like to take this opportunity to express his sincere gratitude to his supervisors **Assoc. Prof. Quan Chenggen** and **Assoc. Prof. Tay Cho Jui**. It is their indefatigable encouragement and guidance that enable him to complete this work and be awarded the honor of the “President’s Graduate Fellowship”.

Special thanks to all staff of the Experimental Mechanics Laboratory and the Strength of Materials Lab. Their hospitality makes the author enjoy his study in Singapore as an international student.

The author would also like to thank his peer research students, who contribute to perfect research atmosphere by exchanging their ideas and experience.

Finally, the author would like to thank his family for all their support.

TABLE OF CONTENTS

ACKNOWLEDGEMENTS		i
TABLE OF CONTENTS		ii
SUMMARY		v
LIST OF FIGURES		vii
LIST OF SYMBOLS		xi
CHAPTER 1	INTRODUCTION	1
1.1	Optical techniques and applications	1
1.2	Data-processing methods	4
1.3	Objective of study	6
1.4	Outline of thesis	7
CHAPTER 2	LITERATURE REVIEW	8
2.1	Fringe projection measurement	8
2.1.1	Fourier transform profilometry	9
2.1.2	Phase-measuring profilometry	13
2.1.3	Spatial phase detection profilometry	17
2.1.4	Linear coded profilometry	20
2.1.5	Removal of the carrier phase component	21
2.2	Digital speckle measurement	25
2.2.1	Difference of phases	27
2.2.2	Phase of differences	31
2.2.3	Direct phase-extraction	34
2.3	Quality-guided phase unwrapping	37
CHAPTER 3	DEVELOPMENT OF THEORY	41
3.1	Wrapped phase extraction	41
3.1.1	Three-frame phase-shifting algorithm with an unknown phase shift	41

3.1.1.1	Processing of fringe patterns	42
3.1.1.2	Processing of speckle patterns	43
3.1.2	Phase extraction from one-frame sawtooth fringe pattern	45
3.2	Phase quality identification	48
3.2.1	Spatial fringe contrast (SFC) quality criterion	49
3.2.2	Plane-fitting quality criterion	51
3.2.3	Fringe density estimation by wavelet transform	53
3.3	Carrier phase component removal	57
3.3.1	Carrier fringes in the x direction	58
3.3.2	Carrier fringes in an arbitrary direction	63
CHAPTER 4	EXPERIMENTAL WORK	65
4.1	Fringe projection system	65
4.1.1	Equipment	65
4.1.2	Experiment	67
4.2	Digital speckle shearing interferometry system	68
4.2.1	Equipment	68
4.2.2	Experiment	70
4.3	Specimens	72
CHAPTER 5	RESULTS AND DISCUSSION	75
5.1	Wrapped phase extraction	75
5.1.1	Three-frame algorithm with an unknown phase shift	75
5.1.1.1	Processing of fringe patterns	75
5.1.1.2	Processing of speckle patterns	77
5.1.1.3	Accuracy analysis	81
5.1.2	Sawtooth pattern profilometry	83
5.1.2.1	Intensity-to-phase conversion	83
5.1.2.2	Accuracy analysis	88
5.2	Phase quality identification	91
5.2.1	Spatial fringe contrast (SFC)	91
5.2.1.1	Selection of processing window size	91

5.2.1.2	Performance comparison of unwrapping algorithms	95
5.2.2	Comparison of conventional and plane-fitting quality criteria	101
5.2.3	Fringe density estimation	106
5.2.3.1	1-D fringe density estimation	106
5.2.3.2	2-D fringe density estimation	110
5.2.3.3	Accuracy analysis	113
5.3	Carrier phase component removal	114
5.3.1	Carrier fringes in the x direction	115
5.3.2	Carrier fringes in an arbitrary direction	117
CHAPTER 6	CONCLUSIONS AND RECOMMENDATIONS	122
REFERENCES		126
APPENDICES		135
A.	C++ source code for Nth-order surface-fitting	135
B.	List of publications	138

SUMMARY

The integration of an optical measurement system with computer-based data-processing methods has recently brought many researchers to the field of optical metrology. In this thesis, several optical phase evaluation techniques for fringe projection and digital speckle measurement have been proposed. The reported methods encompass three stages of optical fringe processing, namely wrapped phase extraction, phase quality identification, and post-processing of an unwrapped phase map.

Algorithms for wrapped phase extraction aim to reduce the complexity in conventional data-recording procedures. A three-frame phase-shifting algorithm is developed to reduce the number of frames necessary for the Carré's technique. A sawtooth fringe pattern profilometry method achieves intensity-to-phase conversion through a simple linear translation instead of phase-shifting or Fourier transform. Experimental results have proven the viability of the methods but indicated the necessity of accuracy enhancement.

Phase quality identification based on the spatial fringe contrast (SFC) and a plane-fitting scheme deals with phase unwrapping problems, such as the profile retrieval of an object with discontinuous surface structure and the error minimization for shadowed phase data. The proposed phase quality criteria are compared with the conventional criteria: the temporal fringe contrast (TFC), the phase derivative variance, and the pseudo-correlation. It is shown that SFC criterion would have potential to replace TFC completely and the plane-fitting criterion had an advantage in detecting projection shadow. A fringe density estimation method based on the continuous wavelet transform is described also. According to the open literature, fringe density

information is beneficial for many spatial filtering techniques in improving their adaptation and automation. Simulated results have demonstrated the viability of the present algorithm on a fringe pattern with added noise.

For post-processing of an unwrapped phase map, a generalized least squares approach is proposed to remove carrier phase components introduced by carrier fringes. With a series expansion method incorporated, the algorithm is able to remove a nonlinear carrier and will not magnify the phase measurement uncertainty. As indicated by a theoretical analysis and subsequent results, the linearity of the phase-to-height conversion can be retrieved after carrier removal and the calibration process of a measurement system can be significantly simplified.

It is concluded that the proposed phase evaluation techniques have provided solutions to overcome some existing problems in the field of optical fringe analysis. However, the accuracy and robustness of the proposed wrapped phase extraction methods and the fringe density estimation algorithm still require further improvements. This could form the basis for future research.

A list of publications arising from this research project is shown in Appendix B.

LIST OF FIGURES

Fig. 2.1	Typical fringe projection measurement system	8
Fig. 2.2	Crossed-optical-axes geometry	10
Fig. 2.3	Band-pass filter in the frequency spectrum	11
Fig. 2.4	Computer-generated fringe patterns projected by a LCD projector	16
Fig. 2.5	(a) Wrapped phase map; (b) Unwrapped phase map; (c) Object shape-related phase distribution	16
Fig. 2.6	Carrier fringes in the x direction	18
Fig. 2.7	(a) Right-angle triangle and (b) isosceles triangle pattern	20
Fig. 2.8	(a) Original and (b) shifted frequency spectrum	22
Fig. 2.9	Difference of phases	28
Fig. 2.10	Phase of differences	31
Fig. 3.1	Theoretical sawtooth fringe pattern	46
Fig. 3.2	(a) Sinusoidal signal with high frequency at the center; (b) CWT magnitude map	55
Fig. 3.3	(a) Geometry of the measurement system; (b) Vicinity of E	59
Fig. 4.1	Schematic setup of fringe projection system	66
Fig. 4.2	Setup of fringe projection system	67
Fig. 4.3	Setup of DSSI system	69
Fig. 4.4	Piezosystem Jena, PX300 CAP, PZT stage	69
Fig. 4.5	Schematic setup of DSSI system	70
Fig. 4.6	Determination of the amount of shearing incorporated	71
Fig. 4.7	Specimen A	72
Fig. 4.8	Specimen B	72

Fig. 4.9	Specimen C	73
Fig. 4.10	Specimen D	73
Fig. 4.11	Specimen E	74
Fig. 4.12	Specimen F	74
Fig. 5.1	Fringe pattern on specimen A	75
Fig. 5.2	Background intensity difference of FFT and phase-shifting	76
Fig. 5.3	(a) Wrapped phase map; (b) phase difference map	77
Fig. 5.4	Speckle fringe pattern (1.2 N load)	78
Fig. 5.5	(a) Smoothened fringe pattern by band-pass filtering; (b) Wrapped phase map (1.2 N load)	78
Fig. 5.6	(a) Wrapped phase map obtained using 3-frame algorithm; (b) Phase map smoothened by sine / cosine filter (1.2 N load)	79
Fig. 5.7	Speckle fringe pattern (5.3 N load)	80
Fig. 5.8	(a) Smoothened fringe pattern by band-pass filtering; (b) Wrapped phase map (5.3 N load)	80
Fig. 5.9	Smoothened wrapped phase map by 3-frame algorithm (5.3 N load)	81
Fig. 5.10	(a) Calculated and theoretical phase shift; (b) Absolute mean difference between calculated and theoretical deformation phase	82
Fig. 5.11	Comparison of the slope distribution of section A-A indicated in Fig. 5.10 obtained by the proposed method and by the theoretical predication of thin-plate-deformation	83
Fig. 5.12	CCD camera-recorded intensity	84
Fig. 5.13	Cross-section after resetting the intensity of intermediate pixels	85
Fig. 5.14	Wrapped phase values obtained from intensities	85
Fig. 5.15	Sawtooth fringe pattern projected on specimen C	86
Fig. 5.16	Intensity along section A-A on Fig. 5.15	87
Fig. 5.17	Section A-A after modification of intermediate pixel's intensity	87
Fig. 5.18	Phase values of section A-A converted from intensities	88

Fig. 5.19	Wrapped phase map extracted from the sawtooth fringe pattern	89
Fig. 5.20	Profile of section <i>B-B</i> , indicated in Fig. 5.18, obtained by (a) one-frame sawtooth profilometry method and contact profilometer; (b) PMP and contact profilometer	90
Fig. 5.21	Projected fringe pattern on specimen D	92
Fig. 5.22	3-D plot of region (a) ABCD <i>x</i> -direction pattern change, (b) EFGH <i>y</i> -direction pattern change, in Fig. 5.21	92
Fig. 5.23	The effect of (a) 30°, (b) 60° phase shift in <i>y</i> direction on SFC	93
Fig. 5.24	(a) Effect of <i>x</i> direction phase shift on SFC; (b) fitting error	94
Fig. 5.25	Wrapped phase map of specimen D	95
Fig. 5.26	(a) Branch-cuts generated by the branch cut algorithm; (b) results of the branch cut unwrapping algorithm	97
Fig. 5.27	(a) TFC map; (b) results by TFC-guided unwrapping	98
Fig. 5.28	(a) SFC map (without fitting error); (b) results by SFC-guided unwrapping (without fitting error)	99
Fig. 5.29	(a) SFC map (with fitting error); (b) results by SFC-guided unwrapping (with fitting error)	100
Fig. 5.30	(a) Phase derivative variance map; (b) unwrapped results guided by variance map	103
Fig. 5.31	(a) Pseudo-correlation quality map; (b) Unwrapped results guided by pseudo-correlation map	104
Fig. 5.32	(a) Plane-fitting quality map; (b) Unwrapped results guided by plane-fitting map	105
Fig. 5.33	(a) Sinusoidal signal with high frequency at the center; Density curve obtained by setting the scale increment step (b) with 1.0; (c) with 0.2; (d) with 1.0 and a mean filter	107
Fig. 5.34	(a) Sinusoidal signal with additive noise; (b) CWT magnitude map; Density curve obtained by setting the scale increment step (b) with 1.0; (c) with 0.2; (d) with 1.0 and a mean filter	109
Fig. 5.35	Vertical fringe pattern	110
Fig. 5.36	(a) Intensity along sections A-A and B-B; Density curve along A-A and B-B (b) without noise reduction weight; (c) with weight	111

Fig. 5.37	Density map of the vertical fringe pattern	112
Fig. 5.38	Circular fringe pattern with parabola density distribution	113
Fig. 5.39	Density map of the circular fringe pattern	114
Fig. 5.40	(a) Specimen E with carrier fringes in the x direction; (b) unwrapped phase map.	115
Fig. 5.41	Phase distribution after removal of (a) a linear carrier; (b) a carrier obtained by 2 nd -order line-fitting.	116
Fig. 5.42	Comparison of results obtained by 2 nd order curve-fitting, linear carrier removal, and contact profiler	117
Fig. 5.43	(a) Specimen E with carrier fringes in an arbitrary direction; (b) phase distribution after the removal of a carrier obtained by independent line-fitting in the x and y directions.	118
Fig. 5.44	Specimen F with carrier fringes in an arbitrary direction	119
Fig. 5.45	Phase distribution after the removal of (a) a linear carrier; (b) a carrier obtained by 2 nd -order surface fitting.	120
Fig. 5.46	Comparison of results obtained by 2 nd order surface-fitting, linear carrier removal, and contact profiler	121

LIST OF SYMBOLS

a	Scale parameter of continuous wavelet transform
a_r	Scale of a wavelet ridge
b	Shift parameter continuous wavelet transform
den	Fringe density
den_x	Fringe density component in the x direction
den_y	Fringe density component in the y direction
Er	Least squares error (penalty) function
f	Frequency of the carrier fringes
h	Height of object
I	Light intensity
I_0	Background light intensity
I_A	Light intensity after loading of an object
I_B	Light intensity before loading of an object
I_{exp}	Experimentally recorded light intensity
I_i	Light intensity of i th frame
I_M	Modulation light intensity
I_{max}	Maximum intensity value
I_{min}	Minimum intensity value
I_o	Light intensity of object speckle field
I_r	Light intensity of reference speckle field
j	$\sqrt{-1}$
$K_{x,y}$	Slope criterion of a plane

l	Distance from the exit pupil of imaging optics to the reference plane
m, n	Variables
M, N	Constant
Mor	Morlet wavelet function
Q	Phase quality
s	Signal function
S	Continuous wavelet transform (CWT) coefficient function
t_1, t_2	Translating parameters
U	Set of pixels
x, y	Variables
δ	Phase shift between fringe or speckle patterns
δ_i	Phase shift introduced in the i th phase-shifted fringe patterns
ϕ	Phase of a physical quantity to be measured
ϕ_E	Phase measurement error
ϕ_c	Carrier fringes-related phase component
ϕ_{obj}	Unwrapped phase map in the measurement of an object
ϕ_{ref}	Unwrapped phase map in the measurement of a reference plane
ϕ_s	Shape-related phase component
ϕ_w	Wrapped phase
γ	Fringe contrast
γ_S	Spatial fringe contrast (SFC)
γ_T	Temporal fringe contrast (TFC)
θ	Speckle-related phase
ω_0	Frequency of the Morlet wavelet

ω_s	Instantaneous frequency of a signal
\mathbf{A}	Series coefficient vector
\mathbf{B}	Experimental phase data vector
\mathbf{X}	Spatial variable matrix
$\text{Im}[\]$	Imaginary part of a complex-valued argument
$\text{Re}[\]$	Real part of a complex-valued argument
$\text{sign}[\]$	Sign of an argument
$W[\]$	Wrapping operator that wraps a phase angle into $[-\pi, \pi]$
$\langle \ \rangle$	Average operator

CHAPTER ONE

INTRODUCTION

The basic approach in optical metrology is to use an optical technique to record a physical quantity of interest. The recorded data are subsequently analyzed manually or automatically to provide quantitative evaluation of the physical quantity. For this reason, an optical measurement process is normally composed of data recording and processing.

1.1 Optical techniques and applications

Optical data-recording techniques encompass a broad range of coherent and incoherent light based methods. The former are based on the physical properties of light wave such as interference and diffraction; while the latter are related to the geometrical features of light beams. Typical coherent methods are interferometric optical testing, holography, speckle interferometry and shearography.

Interferometers such as Newton and Fizeau interferometers are most widely used in testing the quality of optical systems and components (Malacara, 1991). The basic setups of these interferometers have been known for a long time, but depending on applications, they can be modified into various forms. Moreover, a well adjusted interferometric system can even produce interference pattern from incoherent light fields; therefore, Newton and Mirau interferometers also play a significant role in applications of white (incoherent) light interferometry.

The implementation of holography technique essentially relies on the coherent light source – laser. Though the fundamental theory of holography was proposed by

Garbo in 1948, a flourish of this technique in the early 1980s was brought on by the advent of laser. Owing to the large number of researchers in this area, the applications of holography are abundant. From static deformation measurement with double-exposure technique to dynamic event study using sandwich holography setup, holography has established itself as one of the most promising techniques in the field of optical metrology.

In exploring the measurement limits of holography, researchers discovered a new phenomenon called speckle (Dainty, 1984). Speckle, formed by self-interference of a large number of random coherent light beams, hinders high-resolution hologram microscopy; and therefore in the past researchers tried different methods to reduce speckles (McKechnie, 1975). The turning point occurred when it was realized that the speckle, a seemingly random phenomenon, is also an information carrier that could record displacement, surface roughness or shape. Nowadays, the study of speckle-related methods has become a self-contained research discipline. The electronic speckle pattern interferometry (ESPI) has many advantages over traditional techniques. The most significant improvement is that optical data are recorded in digital form that facilitates the integration of optical measurement with computer-based data processing.

Speckle shearing interferometry called Shearography (Leendertz and Butters, 1973; Hung, 1974) is a branch of speckle method that generates the derivatives of displacement. Compared with speckle interferometry, shearography is more insensitive to environmental vibration and therefore suitable for in-situ measurement. Shearography has been successfully applied to nondestructive testing in the car industry and other areas.

In contrast to coherent methods, incoherent methods are able to work with a broad-band light source. Typical examples are photoelasticity, moiré, fringe projection

and digital image correlation. Photoelasticity is the earliest optical technique that gained wide acceptance in industry (Hearn, 1971). Currently, it is used on problems that cannot be easily solved by other methods. Moiré (Durelli, 1970), on the other hand, did not receive much attention at its early days. The specimen-grating preparation and relatively low sensitivity restricted the application of moiré for large deformation measurement. Over the years, the versatility of moiré method was explored in an increasing number of applications such as the measurement of in-plane, out-of-plane deformation, slope, curvature, and topographic contouring. Furthermore, the development in the ability to manufacture and print high-frequency specimen gratings has enabled moiré methods to reach interferometric sensitivities.

Fringe projection technique (Takeda, 1983) was proposed to achieve rapid, non-contact, full-field assessment of an object surface profile. Depth information of an object is encoded into deformed fringe patterns recorded by an image acquisition sensor. The decoding process is implemented in a computer based on similar data processing methods used for interferometric, speckle and moiré fringe patterns. The advantage of fringe projection technique is that using a digital projection device such as programmable liquid crystal display (LCD) projector, fringe density, intensity and pitch can be changed digitally without modifying the physical setup. This greatly facilitates research and development work and enables compact measurement systems based on fringe projection.

Digital image correlation (Chu, 1986) is relatively new in optical metrology. It largely relies on the latest computer technology. The measurement system contains one or two digital cameras that capture an object surface image before and after deformation. Using advanced image correlation algorithms, images at two states are compared patch by patch resulting in a displacement pattern. Digital image correlation

has been applied to analyze a variety of engineering problems such as the measurement of crack-tip displacements and velocity of the fluid flow.

After all, driven by the requirement of industry for nondestructive, high precision measurement, optical techniques are playing a much more important role in field of metrology today than ever before. New methods and techniques are proposed at an increasing rate. Smart measurement systems that originate in the research field today would become commercially available in the market a few years later. This is mainly due to the development of computer technology that offers rapid data acquisition and automatic data processing. A computer-based measurement system provides high-speed analysis and systematic management of results. The ongoing trend of optical measurement system with computer interface would in return bring in new topics into the realm of research.

1.2 Data-processing methods

A number of optical data-recording techniques such as holography, speckle interferometry, moiré and fringe projection record physical quantities like deformation, shape, temperature, refractive index and other parameters, into a specific form of image data – fringe pattern. A fringe pattern is produced either by coherent interference of light fields or by incoherent projection of a periodical light structure onto a test object surface. It encodes physical quantities of interest into intensity fluctuations. In order to retrieve the measurement results, a process known as fringe analysis must be incorporated. Techniques for fringe pattern analysis are as old as interferometric methods. However, before integrating with computer technology, fringe analysis was confined to manual fringe-counting. The real boost in automatic fringe analysis began in early 1980s. Processed by computer-based algorithms, a fringe

pattern is converted to a phase map that provides direct assessment of the physical quantities being measured.

In early 1990s, research in automatic fringe analysis gradually split into two domains. The first deals with a process that extracts a wrapped phase map from fringe patterns. Wrapped phase refers to a phase value that is wrapped in one cycle: $(-\pi, \pi]$ or $[0, 2\pi)$. The choice of wrapped phase extraction algorithm is related to the data-recording techniques used. Although a few algorithms are generally applicable to various measurement setups, a large number of processing methods are specifically designed for a particular optical technique. The second domain studies phase unwrapping problems. In a phase unwrapping process, a wrapped phase map with multiples of 2π jumps between fringe periods is converted to an unwrapped phase map with a continuous distribution. Normally, an unwrapped phase value is related to the physical quantity of interest and the measurement results are readily obtainable through a phase-to-actual quantity conversion. Phase unwrapping is relatively independent from optical techniques and an unwrapping algorithm is generally applicable to wrapped phase maps extracted by different methods.

The separation of wrapped phase extraction and phase unwrapping is essentially owing to two factors. Firstly, it is easier to retrieve a phase value wrapped in one cycle at an early stage without considering the fringe order because intensity fluctuation in a fringe pattern is continuous and no apparent periodical indicator for fringe order is available. When a wrapped phase map is obtained, there would be 2π phase jumps between fringe periods. This information facilitates the determination of fringe order, based on which one can add or subtract multiples of 2π from a phase value. Secondly, research in phase unwrapping is not restricted to optical metrology. Researchers in other disciplines such as synthetic aperture radar (SAR), acoustic

imaging, medical imaging, and aperture synthesis radio astronomy, also put a lot of effort in developing various phase unwrapping algorithms (Ghiglia, 1998). Since the input of an unwrapping algorithm is a wrapped phase map regardless of how it is obtained, many effective algorithms developed in these disciplines are brought into optical metrology. Consequently, the fringe analysis process gradually evolves into wrapped phase extraction and phase unwrapping.

In recent years, with the rapid development of computer technology, automatic fringe analysis has received unprecedented enthusiasm. Several new areas are explored. One of them is the direct retrieval of continuous phase map from a fringe pattern without the intermediate step of wrapped phase extraction. This approach works well in an environment with good signal to noise ratio but its application needs to be further extended. Another area is the temporal fringe analysis, in which the spatial operation of phase unwrapping is completely avoided. Temporal approach is able to solve many problems, such as discontinuous profile measurement, that are difficult to handle in phase unwrapping. However, it requires large amount of data and the data-processing is extensive. The third area is technique-oriented fringe analysis. In this domain, data processing methods are proposed based on specific measurement techniques to solve very special problems. Although they may not be applicable for general purpose, they could provide a good solution for a particular problem under consideration.

1.3 Objective of study

The main objective of this study is to develop optical phase evaluation techniques for fringe projection and digital speckle measurement, and to overcome existing problems in the area of optical fringe analysis. Specifically, (1) In the first stage, a three-frame wrapped-phase-extraction method and a sawtooth profilometry method are developed

to simplify data-recording procedure. (2) In the second stage, a spatial-fringe-contrast and a plane-fitting phase quality criteria are developed to facilitate the phase unwrapping process and a fringe density estimation method is proposed to enhance the performance of various spatial filtering techniques. (3) In the final stage, which deals with post-processing of unwrapped phase maps, a carrier phase component removal technique is proposed.

1.4 Outline of thesis

The thesis is organized into six chapters. In Chapter 1, a brief introduction of different optical techniques and data-processing methods is given.

In Chapter 2, the fringe projection and digital speckle methods together with their specific data-processing algorithms are reviewed. Existing carrier removal strategies are discussed. The significance of phase quality in facilitating a phase unwrapping process is also emphasized.

In Chapter 3, the theory of the proposed phase evaluation techniques, including wrapped phase extraction, phase quality identification, and carrier phase component removal, is presented.

In Chapter 4, the experimental work based on fringe projection and digital speckle shearing interferometry is presented. The specifications of specimens used in this study are included.

In Chapter 5, results obtained by the conventional and proposed methods are compared. The advantages, disadvantages and accuracy of the proposed methods are analyzed in detail.

In Chapter 6, the findings of this study are concluded and future research directions are recommended.

CHAPTER TWO

LITERATURE REVIEW

2.1 Fringe projection measurement

Fringe projection was a technique suitable for measurement of three dimensional (3-D) shape of an object and, depending on the incorporated data-processing strategy, it was also referred to as a certain profilometry method such as Fourier transform profilometry (FTP) or phase measuring profilometry (PMP). A good review paper on optical methods for 3-D shape measurement (Chen et al, 2000) showed that compared with other optical methods, the measurement system of the fringe projection technique was relatively simple, as illustrated in Fig. 2.1.

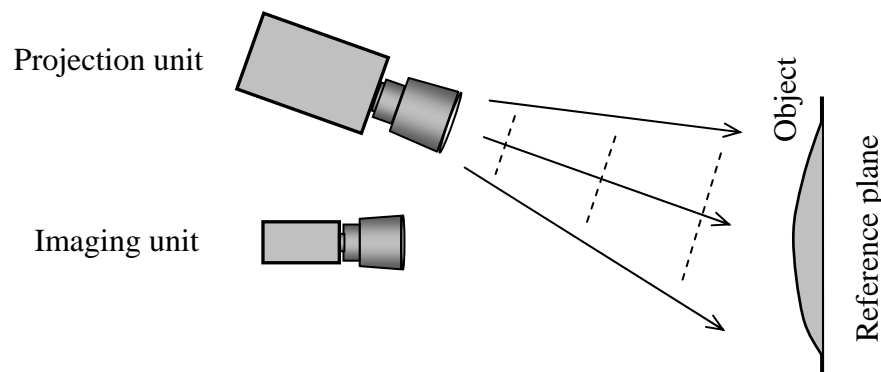


Fig. 2.1 Typical fringe projection measurement system

The system consisted of a projection and an imaging unit. Fringe patterns from the projection unit could be generated in several ways. A square or sinusoidal pattern grating was commonly used as the source of the fringes (Takeda and Mutoh, 1983; Li et al, 1990) before the advent of the digital projection device. A fringe projection system with a digital projector, such as the liquid crystal display (LCD) projector or

the digital mirror device (DMD), would be much more flexible than that using a physical grating (Quan et al, 2001). With a digital projection unit, the phase shifting, fringe density, intensity and other parameters could be changed digitally without modifying the measurement setup. Furthermore, the digital instruments enabled new data-processing strategies (Fang and Zheng, 1997; Sjodahl and Synnergren, 1999) as well as compact measurement systems. In contrast to the diverse choices of a projection unit, the imaging unit currently adopted was almost unexceptionally a charged couple device (CCD) camera, since it provided convenient means for access to an analogue image.

Based on the fundamental principle of triangulation, a fringe pattern projected onto a test object would encounter shape deformation due to the surface height variation. The objective of data-processing is to retrieve the object height distribution from the deformed fringe pattern. The following sections provide a thorough review of wrapped phase extraction methods for the fringe projection technique.

2.1.1 Fourier transform profilometry

Fourier transform profilometry (FTP) was introduced by Takeda et al. (1983). In the paper, Takeda analyzed two kinds of experimental setup originally used in projection moiré topography (Idesawa et al, 1977): crossed-optical-axes and parallel-optical-axes geometry. The former was more applicable to FTP, since it would lead to a compact projection unit. It was also widely adopted in digital projection devices. Figure 2.2 shows the crossed-optical-axes geometry. The projection axis P_1P_2 and imaging axis E_1E_2 intersect at point O on a reference plane. The distance between P_2 and E_2 (the exit pupil of the projection and imaging optics, respectively) is d , and the distance from E_2

to the reference is l . Point A is arbitrary point on the object surface. Points B and C are the intersections of P_2A and E_2A with the reference plane, respectively.

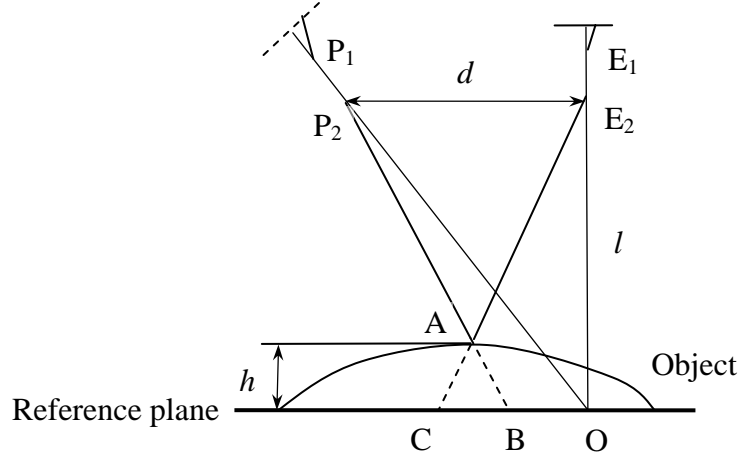


Fig. 2.2 Crossed-optical-axes geometry

A periodical light structure, called carrier fringes, was projected onto the object surface. The recorded intensity variation can be expressed by a Fourier expansion

$$I(x, y) = I_0(x, y) + \frac{1}{2} I_M(x, y) \sum_{n=1}^{\infty} c_n \exp[2\pi f x + n\phi(x, y)] + \frac{1}{2} I_M(x, y) \sum_{n=-\infty}^{-1} c_n \exp[2\pi f x + n\phi(x, y)] \quad (2.1)$$

where I is the recorded intensity, I_0 represents the background intensity, I_M represents the modulation intensity, c_n is the coefficients of the Fourier series, f is the frequency of the carrier fringes, and ϕ is the phase modulation due to the height variation. The intensity pattern was transformed to the frequency domain, where a band-pass filter was applied to select the positive fundamental frequency component ($n = 1$), as shown in Fig. 2.3. Frequency components outside the filtering window were set to zero and an inverse Fourier transform of the filtered spectrum would give a complex-valued intensity distribution

$$I'(x, y) = \frac{1}{2} I_M(x, y) \{ \cos[2\pi f x + \phi(x, y)] + j \sin[2\pi f x + \phi(x, y)] \} \quad (2.2)$$

where I' is the intensity given by the inverse Fourier transform, and j represents $\sqrt{-1}$.

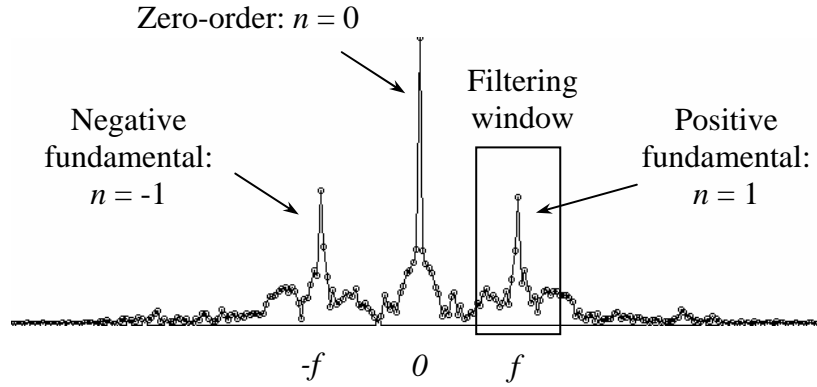


Fig. 2.3 Band-pass filter in the frequency spectrum

Subsequently, a wrapped phase map could be obtained from I'

$$W[2\pi f x + \phi(x, y)] = \arctan \frac{\text{Im}[I'(x, y)]}{\text{Re}[I'(x, y)]} \quad (2.3)$$

where $W[]$ denotes a wrapping operator that wraps a phase angle into $[-\pi, \pi]$, $\text{Im}[]$ and $\text{Re}[]$ denotes the imaginary and the real part of a complex-valued argument. A phase unwrapping process could remove 2π phase jumps and retrieve a continuous phase distribution. The resultant phase distribution contained a carrier phase component $2\pi f x$ and the object shape-related phase ϕ . In order to remove the carrier phase component introduced by carrier fringes, Takeda and Mutoh (1983) proposed to measure the phase distribution of a reference plane without an object. On subtracting the phase map measured without the object from the one with the object, the shape-related phase map could be obtained. Other researchers did also propose alternative approaches for the carrier removal, which will be discussed in detail in a later section.

After carrier removal, the object height could be retrieved by

$$h(x, y) = \frac{l\phi(x, y)}{\phi(x, y) + 2\pi fd} \quad (2.4)$$

Generally, FTP was considered a milestone in automatic fringe analysis. An object height distribution was retrieved at each pixel in the field of view; whereas the moiré topography relied on interpolation to obtain height information between discrete contour lines. However, despite its merits, FTP left many important issues for further improvement. One of them was the system sensitivity. In the filtering process, for accurate extraction of the fundamental component, the object height variation could not exceed a threshold determined by the frequency of the carrier fringes. This restriction imposed a maximum limit of the system sensitivity. Li et al (1990) enhanced the FTP sensitivity by using a quasi-sine projection integrated with a π phase shifting technique. In the case of measurement of a coarse object with speckle-like surface, Lin and Su (1995) extended FTP to two-dimensional (2-D) Fourier transform. They showed that a 2-D filtering window could not only extract the fundamental component of the carrier fringes but also remove speckle noise. The above approaches were confined to continuous surface profile measurement. To address the problem of discontinuous steps or spatially isolated surface measurement, Taketa et al (1997) further proposed frequency-multiplex FTP.

Another disadvantage of FTP was that the optimal value of cut-off frequencies for the band-pass filter was determined by trial and error; and therefore it was difficult to develop a fully-automatic measurement process. In the next section, the author will review a profilometry method that has a higher sensitivity to height variation and requires less human intervention.

2.1.2 Phase-measuring profilometry

Similar to FTP, which borrowed its idea from the interferometric fringe processing based on Fourier transform (Takeda et al, 1982), the phase-measuring profilometry (PMP) brought another well known interferometric data processing approach to the field of fringe projection measurement. The approach was called phase-shifting technique. It required several phase-shifted fringe patterns as the input and gave a wrapped phase map as the output. The phase-shifting approach had various forms, such as 3-frame with $\pi/2$ or $2\pi/3$ phase shift (Wyant et al, 1984; Joenathan, 1994), 4-frame (Quan et al, 2002) or 5-frame with $\pi/2$ phase shift (Hariharan et al, 1987). Each of them had advantages in certain aspects, such as the capability of isolation of vibration or insensitivity to phase-shifting errors. However, a general form of the phase-shifting algorithm (Morgan, 1982) encompassed almost all the special cases. Based on the work of Morgan (1982), Greivenkamp (1984) proposed an even more powerful algorithm, in which the phase shift between consecutive frames need not be a constant.

The fringe pattern intensity produced by the interference of two coherent light fields can be expressed as (Hecht, 2002)

$$I(x, y) = I_0(x, y) + I_M(x, y) \cos \phi(x, y) \quad (2.5)$$

where I_0 and I_M are respectively the background and modulation intensity, and ϕ is the phase difference related to the optical path difference (OPD) between two light fields. The phase-shifting algorithm was able to solve the three unknowns I_0 , I_M and ϕ based on parallel equations that were generated by the introduction of a known phase shift δ in the phase difference. In interferometry, the phase shift could be employed by using a

piezo-electric transducer (PZT) or a polarization optical component. The intensities of phase-shifted fringe patterns are given by

$$I_i(x, y) = I_0(x, y) + I_M(x, y) \cos[\phi(x, y) + \delta_i] \quad (2.6)$$

where I_i is the intensity of i th frame and δ_i is the phase shift introduced in the i th frame.

Greivenkamp (1984) rewrote Eq. (2.6) as

$$I_i(x, y) = a_0(x, y) + a_1(x, y) \cos \delta_i + a_2(x, y) \sin \delta_i$$

where $a_0(x, y) = I_0(x, y)$

$$a_1(x, y) = I_M(x, y) \cos \phi(x, y)$$

$$a_2(x, y) = -I_M(x, y) \sin \phi(x, y) \quad (2.7)$$

and defined a least squares error (penalty) function

$$Er(a_0, a_1, a_2) = \sum_{i=0}^N [a_0(x, y) + a_1(x, y) \cos \delta_i + a_2(x, y) \sin \delta_i - I_{i,\text{exp}}(x, y)]^2 \quad (2.8)$$

where $I_{i,\text{exp}}$ denotes the experimentally recorded intensity of the i th frame and N is the number of frames. To minimize the error, the partial derivatives of Er with respect to a_0 , a_1 , and a_2 were set to zero. The resultant equations were written in a matrix form

$$\begin{bmatrix} N & \sum \cos \delta_i & \sum \sin \delta_i \\ \sum \cos \delta_i & \sum \cos^2 \delta_i & \sum \cos \delta_i \sin \delta_i \\ \sum \sin \delta_i & \sum \cos \delta_i \sin \delta_i & \sum \sin^2 \delta_i \end{bmatrix} \begin{bmatrix} a_0 \\ a_1 \\ a_2 \end{bmatrix} = \begin{bmatrix} \sum I_{i,\text{exp}} \\ \sum I_{i,\text{exp}} \cos \delta_i \\ \sum I_{i,\text{exp}} \sin \delta_i \end{bmatrix} \quad (2.9)$$

Based on Eq. (2.9), a_0 , a_1 , and a_2 could be solved. The phase angle of interest was given by

$$\phi(x, y) = \arctan \frac{-a_2(x, y)}{a_1(x, y)} \quad (2.10)$$

Depending on the sign of a_1 , and a_2 , the phase value could be determined in a modulus of 2π (Creath, 1993).

The phase-shifting algorithm described above was originally for interferometric data processing and was therefore called phase-measurement interferometry (PMI). In 1984, Srinivasan et al pointed out that the same analysis could be applied on fringe projection measurement. By projecting either the interference pattern of two plane wave fronts or the image of a grating with sinusoidal transmission distribution, Srinivasan et al showed that the recorded intensity variation on an object surface was similar to that produced by interference. Hence, the phase-shifting approach of PMI, well known for its accuracy, was applicable to phase-measuring profilometry (PMP).

The phase shift in PMP could be introduced by several means. If the source of projected fringes was the interference pattern of two plane wave fronts, the phase shift could be employed by a PZT. If the image of a grating was used for projection, the phase shift could be introduced by the translation of the grating. Furthermore, if a digital projection device was incorporated, the phase shift could be simply employed by computer-generated, phase-shifted fringe patterns without physical movement of the experimental setup.

Figure 2.4 shows four phase-shifted fringe patterns projected on a lion model. The phase-shifting algorithm is applied to extract a wrapped phase map, as shown in Fig. 2.5(a). A phase unwrapping process would produce a continuous phase distribution (Fig. 2.5(b)). The unwrapped phase map contains a carrier phase component and the object height related phases. After the carrier phase component is removed, the shape-related phase distribution can be obtained, as shown in Fig. 2.5(c).

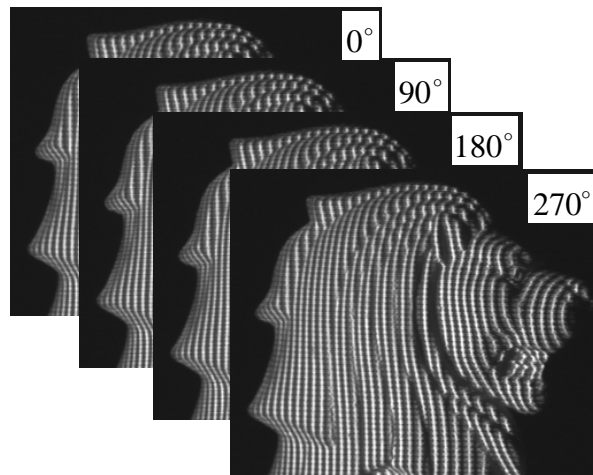
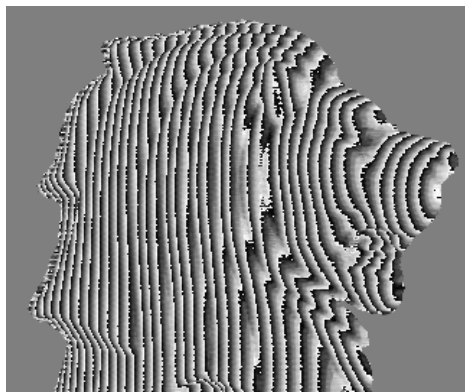


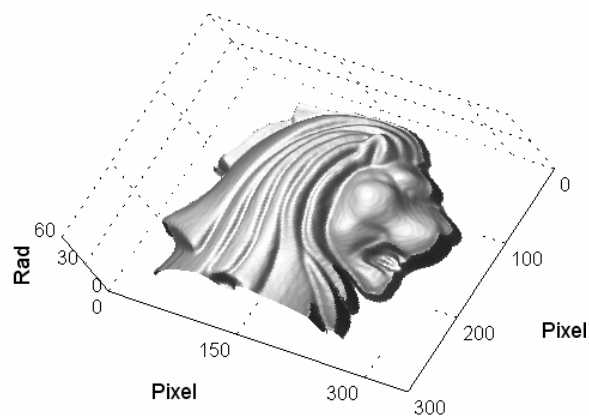
Fig. 2.4 Computer-generated fringe patterns projected by a LCD projector



(a)



(b)



(c)

Fig. 2.5 (a) Wrapped phase map; (b) Unwrapped phase map;
(c) Object shape-related phase distribution

The process for phase-to-height conversion was similar to that in FTP, since both methods are based on the principle of triangulation (Fig. 2.2). Compared with FTP, a significant advantage of PMP was that measurement accuracy was not affected by the frequency of the carrier fringes. However, as PMP required the projection and acquisition of several fringe patterns, it was difficult to apply PMP on dynamic event studies.

Huang et al (1999) proposed a color-encoded PMP technique that could overcome the problem of relatively long data-recording process. The idea was to combine three $2\pi/3$ phase-shifted fringe patterns into a color image with each of the red, green, and blue (RGB) components representing a fringe pattern. A color image projector and a color CCD camera were used as the projection and imaging unit. In data-processing, the RGB components of a recorded color image were separated and a 3-frame phase-shifting algorithm was employed to extract a wrapped phase map. Although this approach could broaden the applications of PMP, the major problem lay in the separation of RGB components. As was common to all RGB cameras, the three channels had overlapping frequencies and hence it was necessary to compensate the overlapping effect by calibration.

In conclusion, despite the fact that PMP was inherently not suitable for dynamic measurements, its accuracy would not be affected by the carrier fringes. In the next section, another profilometry method that integrates the advantage of FTP and PMP in some special situations will be reviewed.

2.1.3 Spatial phase detection profilometry

Spatial phase detection profilometry was proposed by Toyooka and Iwaasa (1986). Its idea was from a corresponding interferometric data-processing technique (Toyooka

and Tominaga, 1984) and it was another good example to show that interferometric and projected fringe patterns had common features. Spatial phase detection extracted the phase value of a pixel by evaluating the intensity of several neighboring pixels. Similar spatial approaches were also reported, such as phase locked loop profilometry (Rodriguez-Vera and Servin, 1994), complex phase tracing (Kozlowski and Serra, 1997) and regularized filter profilometry (Villa et al, 1999). Unlike FTP, these methods performed filtering in the spatial rather than the frequency domain.

Principle of the spatial phase detection algorithm was based on a sinusoidal fitting to the recorded intensity distribution. An important assumption of the method was that the carrier fringes were generated in the x direction, as shown in Fig. 2.6.

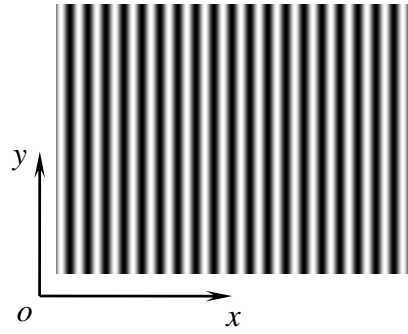


Fig. 2.6 Carrier fringes in the x direction

Toyooka and Iwaasa (1986) showed that if the frequency of the carrier fringes was sufficiently large, the phase value of a pixel was related to the ratio of two correlation coefficients

$$\phi(x, y) = -\arctan \frac{\sum_{x \in U} I(x, y) \sin(2\pi f x)}{\sum_{x \in U} I(x, y) \cos(2\pi f x)} \quad (2.11)$$

where $\sum_{x \in U} I(x, y) \sin(2\pi f x)$ and $\sum_{x \in U} I(x, y) \cos(2\pi f x)$ are the correlation between the intensity of a cross-section with a sine and cosine curve, respectively; and U represents

a set of neighboring pixels of (x,y) along x direction. A wrapped phase map could be obtained by repeating the same process for each pixel in the image.

Theoretically, the spatial approach combined the advantage of FTP and PMP. In data-recording, only one fringe pattern needed to be captured, which enabled the method for dynamic measurement. In data-processing, the correlation process functioned similarly as a least squares method that would result in accurate phase measurement. Practically, however, the algorithm had some critical drawbacks. For example, if the carrier fringes were in an arbitrary instead of in the x direction, the correlation was not applicable. Moreover, an object with non-uniform reflectance would lead the recorded intensity to deviate from a sine pattern and produce uncorrelated coefficients. This might result in phase measurement error. On the other hand, PMP was relatively insensitive to reflectance and thus was superior to the spatial approach. A review paper by Berryman et al (2003) compared the measurement accuracy of FTP, PMP and spatial phase detection under different noise levels. It was found that spatial phase detection could show advantage only with noisy fringe pattern. However, such situation was seldom encountered in fringe projection measurement because, as long as an incoherent light source was used, there would be little speckle noise. Hence, it was suggested that PMP and FTP should be considered prior to spatial phase detection in a practical application.

Although the spatial approach lacks accuracy in phase retrieval, this thesis will propose an effective phase quality criterion based on spatial analysis. Instead of detecting phases, the method detects modulation intensity and phase reliability, which will be addressed later. The following section reviews a profilometry method that does not have a counterpart algorithm for interferometric data processing.

2.1.4 Linear coded profilometry

In the 1990s, with the commercial availability of the digital projection device, a digital projector which was compact, flexible and powerful, gradually replaced gratings as the projection unit. Profilometry methods based on a digital projector, such as random pattern profilometry (Sjodahl and Synnergren, 1999) and linear coded profilometry (Fang and Zheng, 1997), were proposed. A mutual feature of these methods was that they did not project a sinusoidal pattern and data-processing techniques for interferometric fringe pattern analysis were not applicable.

Linear coded profilometry (LCP) employed a phase-shifting algorithm for two types of sawtooth patterns. The first type was a right-angle triangle and the second was an isosceles triangle, as shown in Fig. 2.7. The projection of such sawtooth patterns could only be achieved through a digital projector.

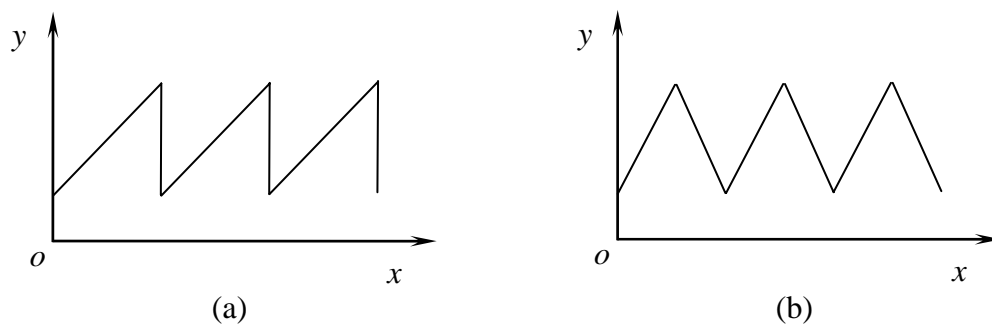


Fig. 2.7 (a) Right-angle triangle and (b) isosceles triangle pattern

The sawtooth pattern phase-shifting algorithm developed by Fang and Zheng (1997) was based on a least squares approach. For the right-angle triangle pattern, a minimum of two phase-shifted images were needed; while for the isosceles triangle pattern, three images were needed. The major advantage of LCP over PMP was in the speed of processing. The sawtooth pattern phase-shifting algorithm was achieved by simple addition and multiplication; while the sinusoidal pattern phase-shifting algorithm was

based on triangular functions that required longer computation time. The disadvantage of LCP was the low tolerance to non-uniform reflectance of an object surface and the sensitivity to defocus-related errors. This was especially true for the right-angle triangle pattern, since abrupt intensity changes and the defocus of the system might severely distort the recorded intensity from the theoretical distribution.

2.1.5 Removal of carrier phase component

Carrier fringes are widely incorporated in various optical measurement procedures. They serve as an information carrier for data-recording but would introduce a carrier phase component in the phase extraction process. The carrier phases must be removed from the overall phase distribution for the evaluation of measurement results. Several authors have proposed different schemes for carrier removal.

Takeda et al (1982) reported in the paper on Fourier transform method for fringe pattern analysis that the carrier phase component could be removed in frequency domain via a spectrum shift, as illustrated in Fig. 2.8. The center of the fundamental frequency component was shifted to the center of the frequency spectrum. Subsequently, an inverse Fourier transform would produce a phase distribution without the carrier phases. The principle of this approach was based on a property of Fourier transform: a spectrum shift of distance $-f$ in the frequency domain is equivalent to the subtraction of a linear component $2\pi fx$ in the spatial domain. Although theoretically correct, the discrete Fourier transform (DFT) could only measure f in terms of an integer number of pixels; while the actual value could be in a fractional pixel. Hence, the spectrum shift with integer pixel accuracy would leave a considerable amount of residual carrier phases unaffected. Another limitation of this method was that it could

only remove a linear carrier component. If the frequency of the carrier fringe was not constant, the spectrum shift scheme was not applicable.

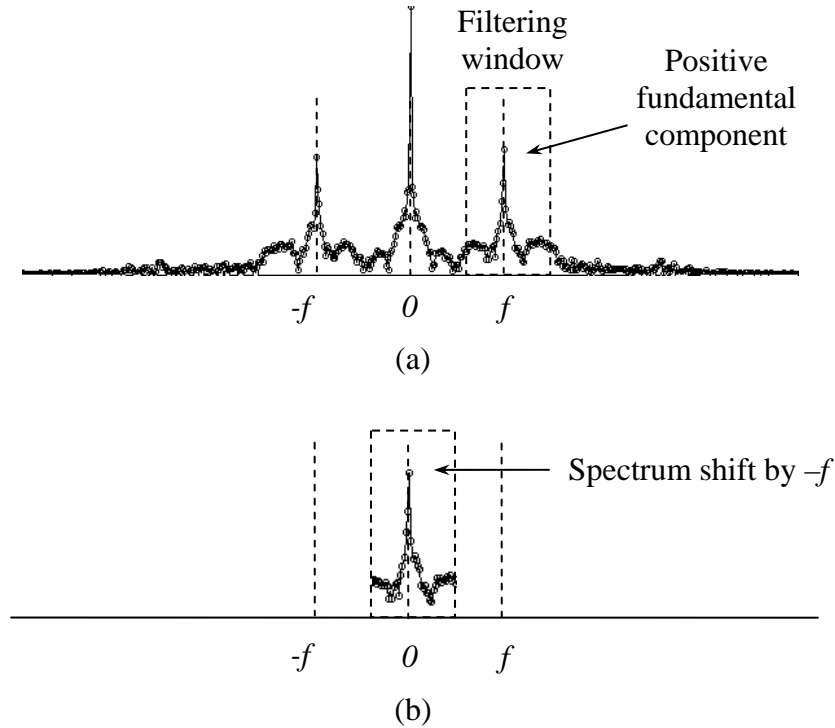


Fig. 2.8 (a) Original and (b) shifted frequency spectrum

In the paper on FTP (1983), Takeda and Mutoh proposed a more robust reference-subtraction method. The unwrapped phase maps of a reference plane and an object were measured. The phase map of the reference plane contained only the carrier phase component and that of the object had both the carrier and shape-related phases. The subtraction of the reference phase map from the object phase map would give the phase distribution of the object profile.

This approach was robust in that, whatever the nature of the carrier, it could be obtained by the measurement of a reference; and hence the subtraction process could remove even a nonlinear carrier as well. However, the method required two measurements and the relative position of the reference and the object need careful

adjustment to reduce system errors. Moreover, phase measurement uncertainty was doubled in the subtraction process, as can be seen in the following equations.

$$\phi_{obj} = \phi_c + \phi_s \pm \phi_E \quad (2.12)$$

$$\phi_{ref} = \phi_c \pm \phi_E \quad (2.13)$$

where ϕ_{obj} and ϕ_{ref} represent respectively the unwrapped phase value of a point on the object and the reference planes; ϕ_c and ϕ_s represent respectively the carrier and the shape-related phase components; and ϕ_E is the maximum error. The measurement uncertainty is in the range $[-\phi_E, \phi_E]$. The subtraction of ϕ_{ref} from ϕ_{obj} results in

$$\phi_{obj} - \phi_{ref} = \phi_s \pm 2\phi_E \quad (2.14)$$

The uncertainty range was doubled because each point in the two measurements had random phase errors that would be magnified, rather than being canceled, by subtraction. Consequently, the overall uncertainty was increased by twice.

An improvement upon the above phase subtraction approach was reported by Srinivasan et al (1985), who proposed a phase mapping approach. This method did not require an additional measurement of a reference plane and therefore the experimental procedure was simplified. One only need put a test object on a reference plate and carry out one measurement process. When the unwrapped phase map was obtained, an arbitrary point on the object was mapped onto a point with an identical phase value on the reference. The distance between these two points on the image could be converted to the actual distance for known system geometrical parameters, such as the projection angle, the relative position of the projection and imaging optics. The object height could then be calculated based on the distance and geometrical parameters. This phase

mapping approach, although facilitated data-recording, still had the problem of magnifying the phase measurement uncertainty during the mapping process.

In 1998, Li et al reported a carrier removal technique that would not magnify the phase measurement uncertainty. Basically, the method removed the carrier phases by subtracting the first derivative from a phase map. Based on Eq. (2.3), the first derivative of the phase distribution contains the slope of the carrier and of the shape-related phases. Li showed that the average of the first derivative over the whole phase map was a good approximation to the slope of the carrier phase component

$$\frac{1}{N} \sum \frac{d(2\pi f x + \phi)}{dx} = 2\pi f + \frac{1}{N} \sum \frac{d\phi}{dx} \quad (2.15)$$

where N is the total number of pixels in the image. Since the slopes of the shape-related phases were positive at some locations and negative at others, they would be averaged out. Hence, the subtraction of the average slope removed the carrier phase component. This method did not magnify measurement uncertainty because the accumulated random error was zero in a statistical average, and subsequently, the subtraction would not bring in extra uncertainty. However, as the method essentially relied on the detection of a constant slope, it was only applicable to linear carrier removal.

The above methods deal with carrier removal through a direct estimation of the carrier. The following discusses methods that do not explicitly handle the carrier. Instead, they establish a phase-to-height relationship by estimation of relevant system geometrical parameters.

Zhou and Su (1994) proposed a method that could be used to measure large objects in a divergent projection condition. The system geometrical parameters were estimated by measurement of at least three different parallel reference planes. Provided

that the geometrical parameters were accurately quantified, a phase value consisted of both the carrier and shape-related components could be used to obtain a height value. However, the calibration process was completed and the estimation error of the geometrical parameters would significantly reduce the accuracy of the phase-to-height conversion.

Salas et al (2003) proposed a coordinate transform scheme to establish the phase-to-height relationship. The method was based on a minimization process to estimate up to seven unknown geometrical parameters. Due to such a large number of unknowns, the minimization algorithm might converge to erroneous solutions and human intervention was required to direct the progress of the program. Another similar approach was reported by Pavageau et al (2004). Instead of using a minimization process to obtain all the geometrical parameters, Pavageau et al suggested that one could calculate only three of them from the unwrapped phase map by a least squares method and directly measure all the rest. Nevertheless, in doing so, the measurement error of geometrical parameters would reduce the overall measurement accuracy and make the accuracy difficult to be evaluated.

2.2 Digital speckle measurement

The phenomenon of speckles was first observed in the 1960s. When a coherent light illuminates an object, a remarkable granular structure of light field would be produced and it is called a “speckle pattern”. In its early days, speckle attracted research interest in developing new methods for high sensitivity measurement (Dainty, 1975). In the mid-1980s, with the rapid development of computer technology and the introduction of automatic fringe analysis, digital speckle methods based on electronic devices gradually replaced traditional speckle techniques that require cumbersome film

developing process. Digital speckle method refers to a broad range of speckle metrology techniques including TV holography (Butters and Leendertz, 1971), digital speckle photography (Burch and Tokarski, 1968), electronic speckle pattern interferometry (ESPI) (Butters et al, 1978), and digital speckle shearing interferometry (DSSI) (Ganesan et al, 1988; Hung, 1989). These techniques are adapted to measure a wide variety of physical quantities, such as in-plane and out-of-plane displacement, slope of displacement, curvature, and 3-D shape. In a book by Rastogi (2001), many applications of digital speckle methods have been reviewed. This section will focus on the data-processing techniques for speckle pattern interferometry.

In contrast to a fringe pattern that is able to record a physical event in an individual frame, a single speckle pattern only records random intensity variations. It is a pair of speckle patterns recorded at different states of an object that preserves the information-related phase. Two mathematical expressions for such speckle patterns are given by

$$I_B(x, y) = I_0(x, y) + I_M(x, y) \cos \theta(x, y) \quad (2.16)$$

$$I_A(x, y) = I_0(x, y) + I_M(x, y) \cos[\theta(x, y) + \phi(x, y)] \quad (2.17)$$

where I_B and I_A represent the intensities before and after loading of an object, I_0 and I_M are the background and modulation intensities, θ is the speckle-related phase, and ϕ is the phase component due to a state change. Statistically, I_0 , I_M and θ are random variables with no obvious connections to the macroscopic properties of the illuminated object (Goodman, 1975). The phase of interest ϕ could be related to the deformation or the slope of deformation of the object, depending on the data-recording techniques employed. The objective of speckle pattern analysis is to retrieve ϕ from one or several pairs of speckle patterns.

During the years of development of automatic fringe analysis, many remarkable phase extraction algorithms for fringe patterns including Fourier transform and phase-shifting have been successfully applied on speckle patterns. At the same time, methods unique to speckle pattern analysis have also been proposed. All of them form an overwhelmingly abundant collection of the speckle pattern data-processing techniques that could not possibly be covered even in a book. However, most, if not all, of the methods can be classified into one of the three approaches: difference of phases, phase of differences, and direct phase-extraction. The following sections will review the most important techniques in each of the approaches.

2.2.1 Difference of phases

The “difference of phases”, as shown in the flow chart (Fig. 2.9), was essentially based on the subtraction of phase maps to retrieve the deformation-related phases. The approach required several phase-shifted speckle patterns at each state of the object. A phase-shifting algorithm could extract a first phase map that contained the random speckle phase θ , and a second that contained the speckle and the deformation phase $\theta + \phi$. The difference of the phase maps would remove the speckle phase component θ . Thereafter, an optional filtering process was incorporated to improve the quality of the deformation phase map for later phase unwrapping.

The phase shift of the speckle patterns was normally employed by a PZT device, which had a relatively linear response to the voltage applied by a digital-to-analogue converter installed in a computer. Most of the phase-shifting algorithms mentioned in section 2.1.2 for PMP were applicable to speckle phase extraction as well (Robinson, 1986). As these phase-shifting algorithms assumed a known phase shift, the response of the PZT to the applied voltages must be calibrated. Cheng and Wyant

(1985) described several techniques to calibrate a linear PZT phase shifter. They also proposed a few methods to evaluate small nonlinearity of a PZT. Based on their work, other authors including Joenathan and Khorana (1992), Jambunathan et al (1995), Ochoa and Huntley (1998), Brug (1999), and Chen et al (2000) proposed alternative means for PZT calibration and the research focus moved from simple linear calibration tasks to *in situ* calibration and nonlinear problems.

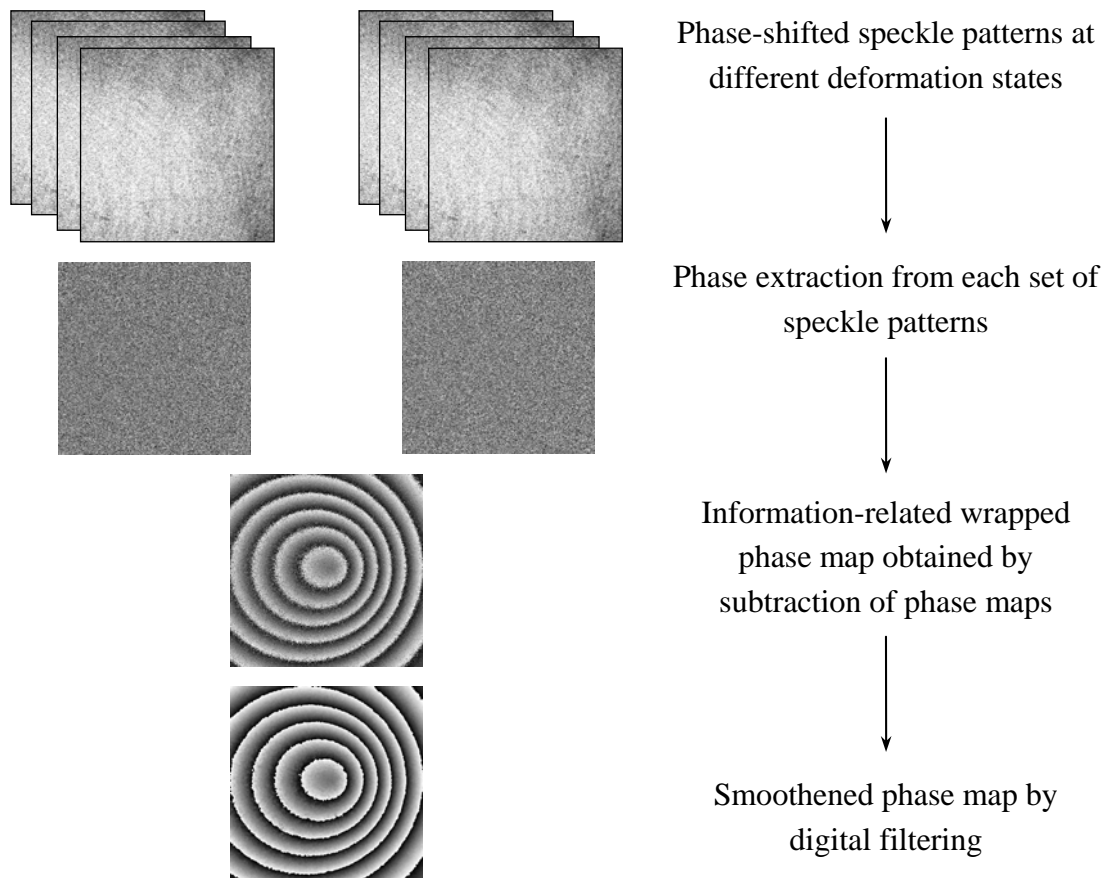


Fig. 2.9 Difference of phases

Provided that a PZT phase shifter was accurately calibrated, the approach of “difference of phases” could provide the best phase measurement accuracy of all the three approaches. However, in many situations, it was only the linearity of a PZT that was known; while the relationship between the phase shift value and the applied voltage is not available. This relationship was mainly dependent on the geometry of an

experimental setup and therefore additional calibration work was needed for the phase-shifting algorithms that required a known phase shift value.

Fortunately, there was another branch of phase-shifting techniques that assumed an unknown phase shift. The most well-known algorithm was called Carré technique (Carré, 1966). It required four fringe patterns with a constant phase shift δ between consecutive intensity measurements expressed by

$$I_1 = I_0 + I_M \cos\left(\phi - \frac{3\delta}{2}\right) \quad (2.18)$$

$$I_2 = I_0 + I_M \cos\left(\phi - \frac{\delta}{2}\right) \quad (2.19)$$

$$I_3 = I_0 + I_M \cos\left(\phi + \frac{\delta}{2}\right) \quad (2.20)$$

$$I_4 = I_0 + I_M \cos\left(\phi + \frac{3\delta}{2}\right) \quad (2.21)$$

The information-related phase ϕ at each pixel could be calculated by:

$$\phi = \arctan\left\{\frac{\sqrt{[(I_2 - I_3) + (I_1 - I_4)][3(I_2 - I_3) + (I_1 - I_4)]}}{(I_2 + I_3) - (I_1 + I_4)}\right\} \quad (2.22)$$

This novel algorithm was initially proposed by Carré in 1966 but was not applied on speckle pattern analysis until 1985 by Creath. Creath's method applied Carré technique twice, firstly on four phase-shifted speckle patterns recorded before an object deformation and secondly on another four after deformation. The difference of the resultant phase maps provided deformation phases. In 1987, based on the work of Schwider et al (1983), Hariharan et al (1987) proposed a five-frame algorithm with unknown phase shift, which was an improvement upon Carré technique. When the

constant phase shift was close to π , Carré technique would produce large errors; but the five-frame algorithm could avoid such problems. Recently, Novak (2003) further studied the properties of a group of five-frame algorithms, such as their computation time, optimal phase shift, and tolerance to nonlinearity error.

The above reviewed algorithms were applicable to many applications of speckle interferometry. However, the deformation phase map normally contained noise due to speckle de-correlation (Creath, 1985). An optional filtering process could be incorporated to remove the noise. The reason that the filtering was “optional” was clarified by Aebischer and Waldner (1999). Their comments on this issue are quoted as follows:

“In our opinion, ..., the problem of evaluating phase fringe patterns can be attacked from two extreme points of view. In the first one, all efforts are put into improving the filter algorithm. If a sufficiently high degree of quality can be achieved, then, ..., there is no need for a fancy unwrapping algorithm. In the second point of view, all efforts are put into improving the unwrapping algorithm. If this algorithm can directly unwraps unfiltered phase fringe patterns, then, ..., there is then no need for a special algorithm for filtering phase fringe patterns.”

As stated above, some unwrapping algorithms had very high tolerance to noise, making the filtering of a wrapped phase map “optional”. Aebischer and Waldner (1999) also showed that for the general purpose of noise removal, a simple iterative application of the very standard sine / cosine filter outperformed many complicated filter algorithms, including scale-space filter (Kaufmann et al, 1995) and Pfister’s partially recursive filter (Pfister, 1993). In this thesis, a sine / cosine filter was used for phase map filtering whenever necessary.

2.2.2 Phase of differences

The approach of “difference of phases” was able to extract phase from phase-shifted speckle patterns at different states but, as it relied on the phase shifting process before and after an object state change, it was difficult to be used for transient event studies. However, the approach of “phase of differences” is suitable for dynamic measurement. A flow chart of the “phase of differences” approach is given in Fig. 2.10.

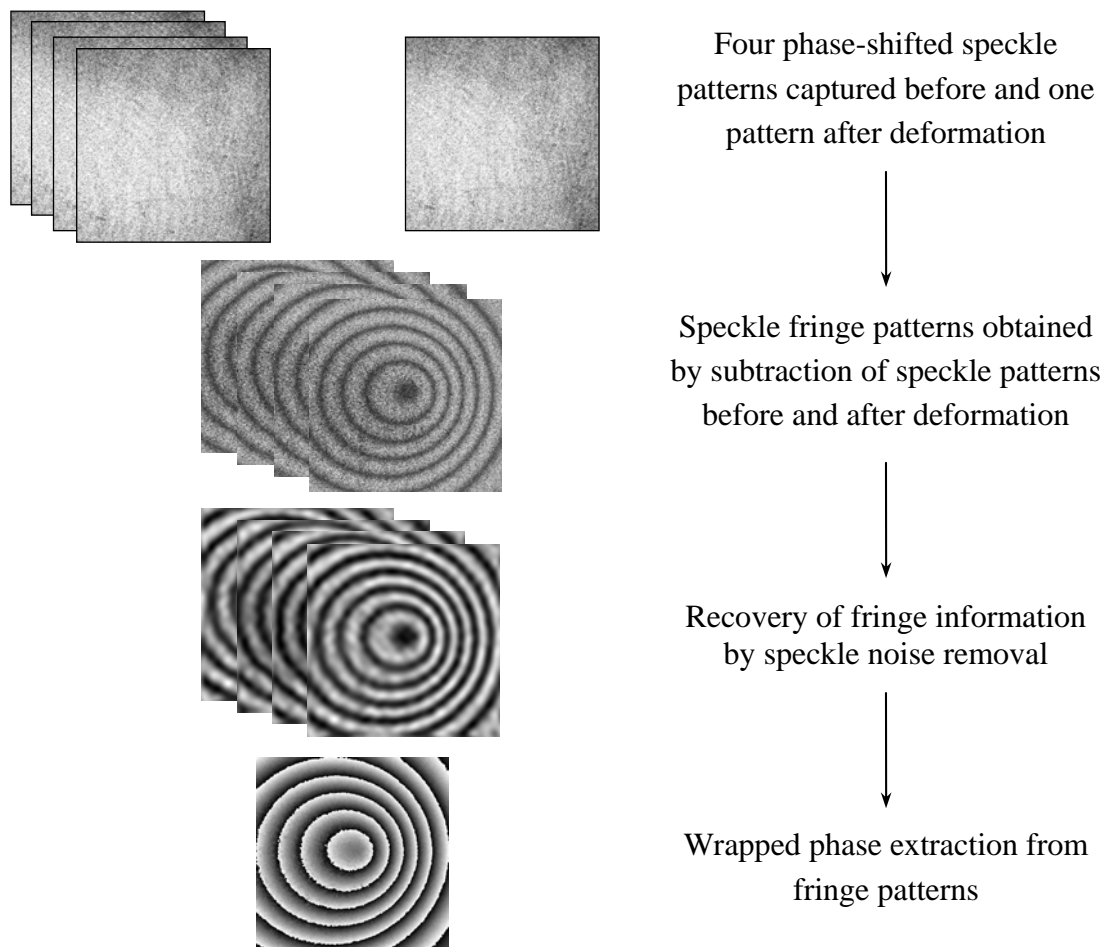


Fig. 2.10 Phase of differences

In this approach, the phase-shifting process was only required when the object is at a static state. During deformation, one speckle pattern was captured at an arbitrary instance. The intensity difference of the speckle patterns before and after deformation

would produce a speckle fringe pattern (Lehmann, 2001), which can be expressed by the subtraction of Eq. (2.16) from Eq. (2.17)

$$I_A - I_B = -2I_M \sin\left(\theta + \frac{\phi}{2}\right) \sin \frac{\phi}{2} \quad (2.23)$$

As can be seen in Eq. (2.23), the fringe term $\sin(\phi/2)$ is multiplied by a random speckle noise term $\sin(\theta + \phi/2)$. The recovery of the fringe information was crucial. If this could be done with considerable accuracy, the differences of the speckle patterns before deformation with the one after deformation could be converted to several phase-shifted fringe patterns. The subsequent phase extraction would be similar to that for interferometric fringe patterns. The flow chart also indicates that for transient event measurement, a series of speckle patterns could be captured, one at an instance of deformation. Combined with the speckle patterns recorded at the static state, a series of phase distributions corresponding to the deformation patterns of the transient event could be retrieved.

Typical methods of this approach were reported by Nakadate and Saito (1985) and Kao et al (2002). Nakadate and Saito used simple spatial low-pass filtering to recover the fringe information. A speckle fringe pattern was filtered by five iterations averaging over 3×3 sample points. A 4-frame $\pi/2$ phase-shifting algorithm was then used to extract a phase map. Kao et al (2002) proposed to extract phases from smoothened fringe patterns by the five-frame algorithm with unknown phase shift (Hariharan et al, 1987). An ultimate method for minimizing the number of frames was introduced by Santoya et al (1988). It was initially applied on interferometric fringe patterns. The so called “single step phase-shifting” technique assumed a couple of $\pi/2$ phase-shifted fringe patterns. Their background frequency component was filtered out

in frequency domain. The quotient of the filtered fringe patterns was fed into an arctangent function to retrieve a wrapped phase map. In the case of speckle fringe patterns (Kerr et al, 1990), a band-pass filter with proper cut-off frequencies could be used to remove both the background (low-frequency) and the speckle noise (high-frequency) components (Kreis, 1986; Kerr et al, 1989). It was shown that, as long as the speckle noise was removed, the resultant fringe patterns could be handled in the same manner as interferometric fringe patterns.

However, fringe recovery was the most difficult part. Normally, considerable amount of errors might be introduced in this step, which accounted for the lower accuracy of this approach compared to the “difference of phases”. Fringe recovery aimed to balance noise reduction and signal preservation. Most algorithms tackled this problem either by frequency band-pass filtering or by spatial operations. According to previously published papers, it was found that the spatial analysis was relatively more versatile, while the frequency-based band-pass filtering (Kreis, 1986; Kerr et al, 1989) always had a strong side effect of blurring high-frequency signals.

The simplest spatial operation was the average or mean filter (Varman and Wykes, 1982; Nakadate and Saito, 1985) but it performed unsatisfactorily in most situations. Varman and Wykes (1982) showed that polynomial fitting could be used to improve the fringe quality; however, the outcome was dependent on the fringe direction. Zhi and Johansson (1991) proposed an adaptive filter for noise removal. This method took into account the image’s local structures, such as the fringe direction, in the filtering process and it could produce better results in preserving signals. The authors also pointed out that an important parameter of the filter, the processing window (kernel) size, was related to the minimum spatial frequency of the fringes. In the mid-1990s, Davila et al (1994, 1995 and 1996) did a lot of work in introducing

noise reduction filters developed in other research disciplines into the speckle fringe processing. They evaluated the behavior of the geometric filter (Crimmins, 1985), the adaptive filter (Frost et al, 1982), the sigma filter (Lee, 1986) and the scale-space filter (Witkin, 1983; Ruiz and Kaufmann, 1998) in application to speckle removal. It is worth noting that except the geometric filter, all the others were dependent on the selection of a suitable processing window size.

In fact, this crucial parameter determines the behavior of most spatial filters. Generally, a small processing window (3×3 to 7×7) should be used for fringe patterns with high fringe density, since filtering within such a small region would not bring unacceptable blurring effect into the signal fringes. However, a large window (21×21 to 35×35) should be used on a fringe pattern with added noise because the noise reduction capability would be greatly enhanced when a large number of (more than 100) data points are taken into consideration. Moreover, due to the wide fringe spacing, there is strong tolerance to the blurring effect. Hence, the processing window size directly controls the quality of the filtered fringe pattern.

In the next section, the importance of processing window size will be further discussed.

2.2.3 Direct phase-extraction

This approach actually encompassed several methods that were not related to each other in principle but a mutual feature of these methods was that phase signal was directly obtained from speckle patterns or a speckle fringe pattern.

The first method was called “single phase step” (Sesselmann and Albertazzi, 1998) or “2 buckets phase step” (Brug and Somers, 1999) technique, in which two $\pi/2$ phase-shifted speckle patterns were recorded before and after an object deformation.

$$I_{B1} = I_0 + I_M \cos \theta \quad (2.24)$$

$$I_{B2} = I_0 + I_M \cos\left(\theta + \frac{\pi}{2}\right) \quad (2.25)$$

$$I_{A1} = I_0 + I_M \cos(\theta + \phi) \quad (2.26)$$

$$I_{A2} = I_0 + I_M \cos\left(\theta + \phi + \frac{\pi}{2}\right) \quad (2.27)$$

The deformation phase ϕ at each pixel could be calculated by

$$\phi = 2 \arctan\left(\frac{I_{A2} - I_{B2} + I_{A1} - I_{B1}}{I_{A2} + I_{B2} - I_{A1} - I_{B1}}\right) \quad (2.28)$$

As only one phase shift at each state was required, a spatial phase-shifting strategy (Kujawinska, 1993) could be used to simultaneously record two phase-shifted speckle patterns. An interesting application of this algorithm for dynamic measurement was reported by Baik et al (2001).

The second method was called direct correlation (Schmitt and Hunt, 1997), which was based on the statistical property of speckles. It was assumed that the speckle phase was a random variable with a uniform probability density function (Goodman, 1975). The correlation coefficient between speckle patterns before (I_B) and after (I_A) deformation was directly related to the deformation phase ϕ :

$$\frac{\langle I_B I_A \rangle - \langle I_B \rangle \langle I_A \rangle}{\left(\langle I_B^2 \rangle - \langle I_B \rangle^2\right)^{\frac{1}{2}} \left(\langle I_A^2 \rangle - \langle I_A \rangle^2\right)^{\frac{1}{2}}} = \frac{1}{2} (1 + \cos \phi) \quad (2.29)$$

where I_B and I_A are as defined in Eqs. (2.16) and (2.17). $\langle \rangle$ denotes an average operator based on a processing window. The phase value obtained from Eq. (2.29) was in the range $[0, \pi)$ and hence phase-shifting was needed to get 2π wrapped phases. For

this reason, direct correlation was often used as a speckle removal filter for other phase extraction algorithms (Kao et al, 2002), despite it being able to directly retrieve the phases. It is worth noting that the direct correlation algorithm was a spatial analysis technique and was dependent on the manual selection of a processing window size.

The last method reviewed in this section is the regularized phase-tracking technique proposed by Servin et al (1997). The method was based on an adaptive signal processing scheme that tracked the phase distribution of a (speckle) fringe pattern by iteratively minimizing an energy function. Marroquin et al (1999) and Servin et al (2001) published relevant papers describing the versatility of the novel phase extraction approach, where details of the algorithm could be found. What is emphasized here is that the regularized phase-tracking technique was also a spatial operation and, although it was claimed to be fully automatic, the parameter of the processing window size still had to be manually chosen based on the prior knowledge of the fringe density in a (speckle) fringe pattern.

It is clearly shown from the spatial methods reviewed in this and the previous sections that an automatic fringe density estimation method would be very helpful for the spatial analysis techniques to achieve higher automation. However, throughout the literature review, it is found that published papers on fringe density estimation are relatively few. Marroquin et al (1998) showed that fringe density could be obtained by a decoupled estimation of the local fringe orientation, direction and frequency magnitude, and the density information could be subsequently used to improve the efficiency of an adaptive quadrature filter (Marroquin et al, 1997). Marklund (2001) proposed a wrapped phase fringe density estimation method. It was shown that the phase fringe density would benefit the tile-based phase unwrapping algorithm

(Stephenson et al, 1994) and could be useful for the phase map filtering and segmentation.

This thesis describes a fringe density estimation method by continuous wavelet transform (CWT). Due to its capability of localized analysis, CWT has drawn more and more attention in optical fringe analysis. Cherbuliez et al (1999) applied CWT on temporal phase extraction. Federico and Kaufmann (2001) studied several wavelet methods in de-noising of ESPI fringes. Liu et al (2003) showed that CWT was superior to Fourier transform in terms of noise reduction. It will be shown that CWT is also applicable for fringe density estimation.

2.3 Quality-guided phase unwrapping

Phase unwrapping (Judge and Bryanston-Cross, 1994) is a big topic related to many research disciplines including optical metrology, synthetic aperture radar, acoustic imaging, magnetic resonance imaging (MRI) and microwave interferometry. An excellent book by Ghiglia and Pritt (1998) presented the fundamental theory and various algorithms of phase unwrapping and showed that a successful unwrapping algorithm could be generally applicable to diverse applications. The phase unwrapping process could be roughly categorized into two classes: path-following and minimum-norm methods. Since this thesis emphasizes the phase evaluation technique, this section will only focus on the quality-guided phase unwrapping approach. In this approach, a phase quality map generated by a certain phase evaluation criterion was incorporated to guide the unwrapping process.

Historically, the quality-guided phase unwrapping approach appeared as a branch of path-following methods. At its primitive stage, Kwon (1987) used the first derivative as a quality criterion to guide the unwrapping process. The quality values

were calculated dynamically and a weighting technique was used to choose the starting pixel. The drawback of the method was that if the start pixel begins from a region of poor data, the resultant unwrapped phase map was unreliable. Bone (1991) proposed a phase quality measure based on the second order partial-derivatives of the phases and applied a threshold to produce a quality mask. This criterion enabled the detection of phase discontinuities that caused integer fringe shifts, which was not possible with the use of the first-difference-based criterion. A pixel would be unwrapped only when it was indicated valid by the mask. Consequently, masked phase data would not introduce error propagation across the continuous phase map. Quiroga et al (1995) improved Bone's method by applying an adaptive threshold so that human intervention was reduced. Lim et al (1995) further enhanced the robustness of the algorithm by allowing the threshold to increase as the unwrapping progressed. This had the effect of unwrapping the high-quality pixels at an early stage, followed by increasingly lower-quality pixels until all pixels were unwrapped. Roth (1995) brought these approaches to maturity by directly using quality values to define the order of unwrapping without the need for thresholds.

Since the quality-guide approach took more information into consideration, it naturally showed superiority to other approaches. With the importance of phase quality became widely recognized, researchers put a lot of effort in modifying existing unwrapping algorithms to make them compatible with the phase quality information. A typical example was the "mask cuts" algorithm (Flynn, 1996), which was a quality-guided version of the classic "branch cut" method (Goldstein et al, 1988; Huntly and Buckland, 1995). The idea of quality-guide was also extended to minimum-norm methods, such as the preconditioned conjugate gradient (PCG) approach (Ghiglia and

Romero, 1994), and the multigrid approach (Pritt, 1996). Both had versions either with or without phase quality to facilitate the unwrapping process.

In recent years, with so many smart phase unwrapping methods compatible with the quality information, researchers began to realize that the success of an unwrapping process was more dependent on the accuracy of the phase quality than on the implementation of a specific algorithm. If a good quality map was available, most algorithms would perform satisfactorily; whereas if the quality criterion was misleading, even the most intelligent algorithm would be trapped in errors. Hence, the study on the evaluation criterion of phase data deserves equivalent, if not more, importance to the research on new phase unwrapping algorithms.

Conventionally, phase quality criteria based on pseudo-correlation (Roth, 1995), phase derivative variance (Pritt, 1996), and maximum phase gradient (Ghiglia and Pritt, 1998) were applicable to phase maps obtained by different means. These quality measures were directly extracted from the wrapped phase map. Although they were capable of detecting noise, they sometimes lacked accuracy in analyzing phase data with special features. Other types of quality criteria, like the correlation map for synthetic aperture radar (Xu and Cumming, 1996), were not derived from the phase data alone. They were generated by the raw data used to produce the wrapped phase map. Theoretically, these criteria were the best quality indicator for the corresponding phase map because they inherently carried the quality or reliability information of the phases.

In the domain of optical fringe pattern analysis, the most well known quality criterion was the fringe modulation (Xu and Ai, 1993; Dirksen et al, 1993; Strobel, 1996). An advanced form was the fringe contrast defined by the ratio of the modulation intensity with the background intensity (Creath, 1993). These parameters

were widely incorporated to facilitate unwrapping, filtering, masking and improving visualization of phase fringes, since they inherently described the visibility of the recorded fringe pattern. The standard phase-shifting algorithm could be employed to calculate the fringe contrast. Based on Eq. (2.7), the fringe contrast is given by

$$\gamma_T = \frac{(a_1^2 + a_2^2)^{1/2}}{a_0} \quad (2.30)$$

Naturally, the higher the contrast, the better was the quality. Compared with other criteria, the fringe contrast was superior in detecting shadows and low reflectance regions. However, Li and Su (2002) showed that in fringe projection measurement, noise introduced by CCD saturation, drastically changing surface reflectance and quasi-speckle structure in the fringes might not be accurately identified by the fringe modulation (contrast). They proposed to incorporate the fitting error given by Eq. (2.8) into the quality criterion. Their new criterion proved to be more robust in phase quality evaluation.

Except for the above mentioned quality criteria, open literature shows that published work on phase quality evaluation is relatively little. It is also suggested by Ghiglia and Pritt (1998) that more research efforts should be expected in exploring new phase quality evaluation methods. In this thesis, two phase quality criteria, the plane-fitting-based and the spatial fringe contrast-based evaluation algorithms, are proposed. It will be shown that the proposed methods could be used to solve some special problems that are difficult to handle by conventional techniques.

CHAPTER THREE

DEVELOPMENT OF THEORY

The theoretical development of the proposed optical phase evaluation techniques is organized in three sections corresponding to three stages of optical fringe analysis. The first stage is the wrapped phase extraction from fringe or speckle patterns. Specifically, a three-frame phase-shifting algorithm and a one-frame sawtooth pattern profilometry method are presented. In the second stage, the issue of phase quality identification is discussed. Phase quality criteria based on the spatial fringe contrast (SFC) and the least squares plane-fitting scheme will be shown in facilitating of the phase unwrapping process. The fringe density-estimation method, beneficial for various spatial analysis techniques, will be developed based on the continuous wavelet transform (CWT). The last stage focuses on post-processing of an unwrapped phase map. It presents the theory of the carrier phase component removal.

3.1 Wrapped phase extraction

3.1.1 Three-frame phase-shifting algorithm with an unknown phase shift

According to open literature, there are basically two branches of phase-shifting algorithms: the first with a known phase shift and the other with an unknown phase shift. The proposed three-frame algorithm belongs to the latter and it is developed to reduce the number of frames required by Carré's technique (Carré, 1966). The equations are first derived based on processing of projected fringe patterns in shape measurement, and subsequently, the method is extended to the processing of speckle patterns for deformation measurement.

3.1.1.1 Processing of fringe patterns

The general expression for the intensity of a fringe pattern is given by

$$I_i = I_0 + I_M \cos(\phi + \delta_i) \quad (3.1)$$

where I_i represents the light intensity of the i th frame, I_0 is the background intensity, I_M is the fringe modulation intensity, ϕ is the phase to be measured, and δ_i is the phase shift introduced. Carré's technique (Carré, 1966) needs four frames with a constant δ to extract a wrapped phase value, since there are four unknowns I_0 , I_M , ϕ and δ . However, several authors (Kreis, 1986; Santoyo et al, 1988; Cuellar, 2003) implemented background removal before phase extraction. As I_0 is a slow-varying variable compared to ϕ , it can be removed in the frequency domain. In doing so, an unknown variable is eliminated and the number of frames required by the Carré's technique is reduced.

A high-pass filter is used to remove the background frequency component from the frequency spectrum. The intensity of three frames after inverse Fourier transform can be written as

$$I_1 = I_M \cos(\phi - \delta) \quad (3.2)$$

$$I_2 = I_M \cos \phi \quad (3.3)$$

$$I_3 = I_M \cos(\phi + \delta) \quad (3.4)$$

where δ is the constant phase shift introduced in each step. It is easy to show that ϕ can be obtained by a four-quadrant arctangent function

$$\phi = \arctan \left[\frac{I_1 - I_3}{\sqrt{4I_2^2 - (I_1 + I_3)^2}} \right] \quad (3.5)$$

$$\text{sign}[\sin \phi] = \text{sign}[I_1 - I_3] \quad (3.6)$$

$$\text{sign}[\cos \phi] = \text{sign}[I_2] \quad (3.7)$$

where $\text{sign}[\]$ denotes the sign of an argument. Based on Eqs. (3.5-3.7), ϕ is determined in $[-\pi, \pi]$ and the constant phase shift δ is also retrieved in $[0, \pi]$ by

$$\delta = \arccos\left(\frac{I_1 + I_3}{2I_2}\right) \quad (3.8)$$

There are two special cases, in which the value of ϕ cannot be directly obtained from the above equations. First case: $I_2 = 0$. As indicated by Eq. (3.3), if I_2 is zero, ϕ is either $\pi/2$ or $-\pi/2$. Since $\sin \phi$ has the same sign as $I_1 - I_3$ (Eq. (3.6)), a positive value of $I_1 - I_3$ would result in $\phi = \pi/2$; whereas a negative value results in $\phi = -\pi/2$.

Second case: $|I_1 + I_3| > |2I_2|$ and $I_2 \neq 0$. In an ideal sinusoidal distribution, $|I_1 + I_3|$ should be smaller than or equal to $|2I_2|$, as indicated by Eqs. (3.2-3.4). In practice, the situation $|I_1 + I_3| > |2I_2|$ may arise for small $|I_2|$ due to noise. Hence, it would introduce few error by approximating the value of I_2 to zero for $|I_1 + I_3| > |2I_2|$, and subsequently, this case can be handled as in previous, where $I_2 = 0$.

3.1.1.2 Processing of speckle patterns

In speckle interferometry, such as electronic speckle pattern interferometry (ESPI) and digital speckle shearing interferometry (DSSI), a speckle pattern is produced by the interference of the object and reference speckle fields.

$$I_B = I_o + I_r + 2\sqrt{I_o I_r} \cos \theta \quad (3.9)$$

$$I_A = I_o + I_r + 2\sqrt{I_o I_r} \cos(\theta + \phi) \quad (3.10)$$

where I_B and I_A represent the speckle pattern intensities before and after an object deformation, I_o and I_r are respectively the intensities of the object and reference speckle fields, θ is the speckle related phase, and ϕ is the deformation related phase. The difference between a speckle pattern background $I_o + I_r$ and a fringe pattern background I_o lies in that the former is a high-frequency variable and cannot be separated from ϕ in frequency domain.

A conventional approach (Santoyo F. M. et al, 1988) takes the difference of two speckle patterns and applies a band-pass filter to remove speckle fringe background and speckle noise in the frequency domain. This method, however, may reduce high-frequency phase signal. In this thesis, a special background removal technique for speckle pattern is developed. Three phase-shifted speckle patterns are recorded before and after deformation, respectively, and the intensities are given by

$$\begin{cases} I_1 = I_o + I_r + 2\sqrt{I_o I_r} \cos(\theta - \delta) \\ I_2 = I_o + I_r + 2\sqrt{I_o I_r} \cos \theta \\ I_3 = I_o + I_r + 2\sqrt{I_o I_r} \cos(\theta + \delta) \end{cases} \quad (3.11)$$

$$\begin{cases} I_4 = I_o + I_r + 2\sqrt{I_o I_r} \cos(\theta + \phi - \delta) \\ I_5 = I_o + I_r + 2\sqrt{I_o I_r} \cos(\theta + \phi) \\ I_6 = I_o + I_r + 2\sqrt{I_o I_r} \cos(\theta + \phi + \delta) \end{cases} \quad (3.12)$$

A point-wise average intensity pattern is calculated

$$\frac{1}{6} \sum_{i=1}^6 I_i = I_o + I_r + \frac{2\sqrt{I_o I_r}}{3} (1 + 2 \cos \delta) \cos \left(\theta + \frac{\phi}{2} \right) \cos \frac{\phi}{2} \quad (3.13)$$

Since the last term of Eq. (3.13) contains multiple cosine functions with δ , θ , and ϕ as undetermined arguments, it is highly probable to be a small value. Hence, the dominant component of the average intensity pattern is the speckle background. In this study, the average intensity is taken to be the approximate background intensity and subtracted from each of the speckle patterns. Subsequently, the approach of difference of phases is used (Creath, 1985). The three-frame algorithm is applied twice to obtain wrapped phase maps before and after deformation. On subtraction of the wrapped phase maps, a deformation related phase map is obtained.

Although the three-frame phase-shifting algorithm with unknown phase shift is applicable to fringe as well as speckle patterns, it could be more useful for the latter, since in fringe projection profilometry the phase shift is normally known. The next section will develop a one-frame sawtooth fringe pattern profilometry method, in which the phase extraction process does not rely on phase-shifting or Fourier transform.

3.1.2 Phase extraction from one-frame sawtooth fringe pattern

The sawtooth fringe pattern analysis method is specifically proposed for the fringe projection measurement. In contrast to conventional techniques, such as Fourier transform profilometry (Takeda, M. and K. Mutoh 1983), phase-measuring profilometry (Srinivasan, V. et al, 1984), which projects a sine pattern, the proposed technique projects a sawtooth pattern. Since the a wrapped phase distribution also has sawtooth characteristics, the benefit of encoding surface profile with a sawtooth pattern is that wrapped phase extraction can be achieved by simple intensity-to-phase conversion; while phase-shifting or Fourier transform is not needed.

A sawtooth fringe pattern is generated for projection, as shown in Fig 3.1, which can be expressed as

$$I(x, y) = I_0 + I_M W[2\pi f x + \phi(x, y)] \quad (3.14)$$

where I_0 and I_M are background and modulation intensity respectively; $W[]$ wraps a phase angle into $[-\pi, \pi]$, f is the spatial fringe frequency, and ϕ is related to the surface height.

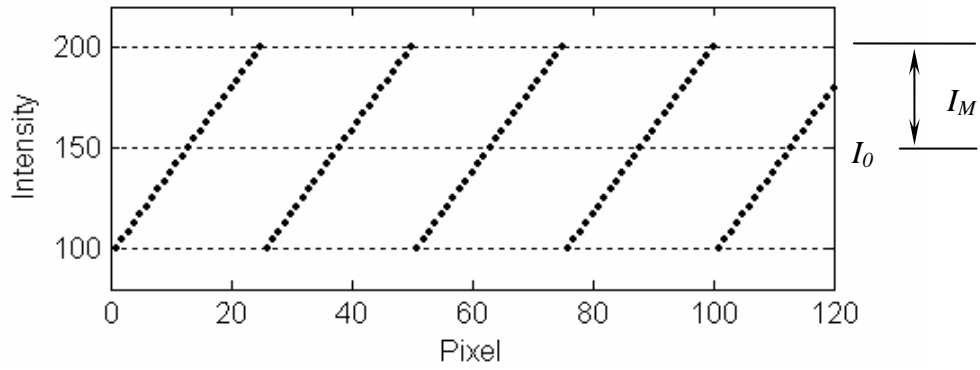


Fig. 3.1 Theoretical sawtooth fringe pattern

Since I_0 and I_M are computer-generated constant, the intensity $I(x, y)$ is related to the wrapped phase angle

$$\phi_w(x, y) = W[2\pi f x + \phi(x, y)] \quad (3.15)$$

Hence, a linear translation function can be used to obtain a wrapped phase angle from an intensity level.

$$\phi_w(x, y) = t_1 I(x, y) + t_2 \quad (3.16)$$

where t_1 and t_2 are translating parameters retrievable from the global maximum (I_{\max}) and minimum (I_{\min}) intensities of a sawtooth pattern.

$$\begin{cases} t_1 I_{\max} + t_2 = \pi \\ t_1 I_{\min} + t_2 = -\pi \end{cases} \Rightarrow \begin{cases} t_1 = \frac{2\pi}{I_{\max} - I_{\min}} \\ t_2 = -\pi \frac{I_{\max} + I_{\min}}{I_{\max} - I_{\min}} \end{cases} \quad (3.17)$$

The above relationship holds as long as the theoretical sawtooth pattern has constant value of I_0 and I_M . The maximum intensity (I_{\max}) corresponds to the maximum wrapped phase angle (π) and the minimum intensity (I_{\min}) corresponds to the minimum wrapped phase angle ($-\pi$). When t_1 and t_2 are determined, the intensity of each pixel is used in Eq. (3.16) to calculate the corresponding wrapped phase value. The resultant wrapped phase map can be unwrapped and the overall phase distribution would have a carrier phase component $2\pi fx$ as well as an object shape-related phase component ϕ .

The above presented is the fundamental principle for intensity-to-phase conversion. In practice, when the computer-generated sawtooth pattern is projected and imaged, the intensity distribution recorded would not be perfectly uniform. A sawtooth pattern is more appropriate when expressed in terms of a varying rather than constant background and modulation intensity.

$$I(x, y) = I_0(x, y) + I_M(x, y)\phi_w(x, y) \quad (3.18)$$

where I_0 and I_M undergo low-frequency variations in comparison to ϕ as long as the illumination and reflectance do not change drastically. Under such circumstance, if the global maximum and minimum intensities are used to determine the translating parameters t_1 and t_2 , a large error would be produced; because I is not globally, linearly related to ϕ_w . However, within one sawtooth fringe period at an arbitrary cross-section,

I can still be considered linearly varying with ϕ_w assuming that I_0 and I_M are slow-varying. Hence, in practice, the local maximum and minimum intensities should be used to determine a pair of t_1 and t_2 associated with each cross-sectional fringe period. Subsequently, the parameters are used for the intensity-to-phase conversion of the corresponding local region.

The three-frame algorithm and the sawtooth pattern profilometry method utilize pixel intensity to retrieve wrapped phase information, which forms the first stage of fringe analysis. A resultant wrapped phase map may contain invalid phase data caused by projection shadow or a mixture of speckle noise with high-frequency phase fringes. In the next section, theory of the phase quality evaluation is presented. Instead of focusing on retrieval of phase values, the phase quality evaluation aims to provide a measure of the validity of phase fringes. The quality information could inform other processing algorithms, such as phase unwrapping and spatial filtering, the localized reliability of a phase fringe pattern.

3.2 Phase quality identification

In a wrapped phase map, phase information is previously retrieved in one cycle of a fringe period. A phase unwrapping process is necessary to deduce the relative relationship between phases of different periods, thereby to obtain the continuous feature of a phase distribution. In this thesis, the quality-guided phase unwrapping approach is adopted and two phase quality measures are developed to facilitate the unwrapping process. A fringe density evaluation method is also proposed. The density information, instead of being applied to phase unwrapping, is beneficial for various existing spatial filtering techniques.

3.2.1 Spatial fringe contrast (SFC) quality criterion

SFC of a pixel is calculated by evaluating its $M \times N$ neighboring pixels' intensities and therefore this approach is processing window-based. For a sinusoidal fringe pattern projected on an object, the light intensity of an $M \times N$ pixel window with point (x, y) at the center can be expressed as:

$$I(m, n) = I_0(x, y) + I_M(x, y) \cos[2\pi f m + \phi(m, n)]$$

$$\text{where } m \in [x - M/2, x + M/2] \text{ and } n \in [y - N/2, y + N/2] \quad (3.19)$$

m and n are spatial variables, I_0 and I_M are the background and modulation intensity, respectively, ϕ is the object height-related phase and f is the carrier fringe frequency in the x direction. It is important to note that I_0 and I_M are associated with (x, y) but ϕ is associated with (m, n) . This is because I_0 and I_M are normally considered slow-varying compared to ϕ and therefore can be assumed to be constant in a pixel window.

Prior knowledge of the carrier frequency f , which can be measured in the frequency spectrum (Takeda et al, 1982), is required. The SFC is derived by a least squares method. Rewrite Eq. (3.19) as

$$I(m, n) = a_0(x, y) + a_1(x, y) \cos(2\pi f m) + a_2(x, y) \sin(2\pi f m)$$

$$\text{where } a_0(x, y) = I_0(x, y)$$

$$a_1(x, y) = I_M(x, y) \cos \phi(m, n)$$

$$a_2(x, y) = -I_M(x, y) \sin \phi(m, n) \quad (3.20)$$

An error function is defined as

$$Er(x, y) = \sum_{m=x-M/2}^{x+M/2} \sum_{n=y-N/2}^{y+N/2} [a_0(x, y) + a_1(x, y) \cos(2\pi f m) + a_2 \sin(2\pi f m) - I_{\text{exp}}(m, n)]^2 \quad (3.21)$$

where I_{exp} is the experimentally recorded intensity. A necessary condition for the minimal error is that the partial derivatives of Er with respect to a_0 , a_1 and a_2 are zero

$$\begin{cases} \frac{\partial Er}{\partial a_0} = 2 \sum \sum [a_0 + a_1 \cos(2\pi f m) + a_2 \sin(2\pi f m) - I_{exp}(m, n)] = 0 \\ \frac{\partial Er}{\partial a_1} = 2 \sum \sum \cos(2\pi f m) [a_0 + a_1 \cos(2\pi f m) + a_2 \sin(2\pi f m) - I_{exp}(m, n)] = 0 \\ \frac{\partial Er}{\partial a_2} = 2 \sum \sum \sin(2\pi f m) [a_0 + a_1 \cos(2\pi f m) + a_2 \sin(2\pi f m) - I_{exp}(m, n)] = 0 \end{cases} \quad (3.22)$$

Based on Eq. (3.22), the unknowns a_0 , a_1 and a_2 can be obtained. Subsequently, the SFC, γ_s , is given by:

$$\gamma_s(x, y) = \frac{[a_1^2(x, y) + a_2^2(x, y)]^{1/2}}{a_0(x, y)} \quad (3.23)$$

An SFC value is determined by two factors: the reflectivity of an object surface and the structure-related spatial phase shift in a fringe pattern. The first factor affects the SFC in a similar way as to the temporal fringe contrast (TFC). High reflectivity would result in a large SFC and vice versa. The second factor reflects the structure information of an object profile. To enhance the reliability of the phase quality, a method proposed by Li and Su (2002) is used. The fitting error Er obtained by substituting a_0 , a_1 and a_2 into Eq. (3.21) is incorporated, and a phase quality criterion is defined as

$$Q(x, y) = \frac{\gamma_s(x, y)}{1 + c \frac{Er(x, y)}{\gamma_s(x, y)}} \quad (3.24)$$

where c is an adjustable variable to control the significance of Er in the criterion.

Basically, SFC applies the N-frame phase-shifting algorithm (Greivenkamp, J. E.1984) in the spatial domain. As quality information (spatial fringe contrast) is obtained by the evaluation of spatially related pixels, SFC is more sensitive to spatial quality defects than the conventional temporal fringe contrast. In the next section, a similar plane-fitting quality criterion for phase quality evaluation is presented. In contrast to SFC that is applied on a fringe pattern, the plane-fitting quality criterion is applied on a wrapped phase map.

3.2.2 Plane-fitting quality criterion

The plane-fitting quality criterion generates phase quality information from a phase map.

$$z(x, y) = 2\pi fx + \phi(x, y) \quad (3.25)$$

where z is a phase angle, f and ϕ are as defined in Eq. (3.19). For a pixel under consideration, a quality value is generated by the evaluation of its $M \times N$ neighboring pixels. A plane in 3-D Cartesian coordinate is expressed as

$$z = k_x x + k_y y + z_0 \quad (3.26)$$

where (x, y) shows the location of a pixel in the phase map, $(-k_x, -k_y, 1)$ is the normal vector of the plane, and z_0 is the intersection of the plane with the z axis. To fit the plane to the phase data, an error function is defined

$$Er(x, y) = \sum_{m=x-M/2}^{x+M/2} \sum_{n=y-N/2}^{y+N/2} [mk_x + nk_y + z_0 - \phi_{\text{exp}}(m, n)]^2 \quad (3.27)$$

where m and n are spatial variables, and ϕ_{exp} refers to the experimentally obtained phase data. The partial derivatives of Er with respect to k_x , k_y and z_0 are set to zero.

This produces the following equations

$$\begin{cases} \frac{\partial Er}{\partial k_x} = 2 \sum \sum m [mk_x + nk_y + z_0 - \phi_{exp}(m, n)] = 0 \\ \frac{\partial Er}{\partial k_y} = 2 \sum \sum n [mk_x + nk_y + z_0 - \phi_{exp}(m, n)] = 0 \\ \frac{\partial Er}{\partial z_0} = 2 \sum \sum [mk_x + nk_y + z_0 - \phi_{exp}(m, n)] = 0 \end{cases} \quad (3.28)$$

The values of k_x , k_y and z_0 can be solved and on substituting these values into Eq. (3.27), the fitting error Er is obtained. The criterion for the phase quality is defined as

$$Q(x, y) = \frac{K_{x,y}}{c_1 + \frac{Er(x, y)}{K_{x,y}}}$$

$$\text{where } K_{x,y} = \frac{|k_x|}{c_2 + |k_y|} \quad (3.29)$$

and c_1 and c_2 are variable coefficients used to modulate the denominator and prevent it assuming a zero value. The parameter $K_{x,y}$ is related to the slope of the fitted plane. According to the carrier phase component $2\pi f x$ in the x direction, $|k_x|$ should be approximately $2\pi f$ and $|k_y|$ should be zero. In a shadowed or noisy area, either small $|k_x|$ or large $|k_y|$ would be found, which results in a small value of $K_{x,y}$. The fitting error Er describes the degree of uniformity of the phase data. Incorporating Er in the

quality criterion ensures that the larger the error, the less is the uniformity and thereby lower phase quality.

In summary, both the plane-fitting and the spatial fringe contrast criteria generate phase quality values by a least squares fitting process. They have inherent capability of detecting spatially related phase quality defects.

3.2.3 Fringe density estimation by wavelet transform

In this section, the estimation theory for fringe density, which is useful for processing window-based spatial filtering techniques, is presented. Similar to the Fourier transform which analyzes a signal by a superposition of sine and cosine functions, the continuous wavelet transform (CWT) analyze a signal in terms of wavelet functions

$$S(a, b) = \frac{1}{a} \int_{-\infty}^{+\infty} s(x) \text{Mor}\left(\frac{x-b}{a}\right) dx \quad (3.30)$$

where $s(x)$ is the signal, $S(a, b)$ is the CWT coefficient function, a and b are the scale and shift parameters respectively, and $\text{Mor}(x)$ is a wavelet function. A signal in spatial domain is transformed into time-scale domain, which means that the CWT coefficient is associated with a scale describing the feature of interest, such as details (small scale) or approximations (large scale), and a shift specifying a local region being analyzed. The time-scale approach is a major advantage of CWT over Fourier transform and enables CWT to local fringe density estimation.

CWT is a correlation process, where high similarity between a signal and a wavelet would show a large coefficient and vice versa. As a fringe pattern is modulated by a sine function, a suitable choice of wavelet function is the complex Morlet wavelet (Cherbuliez et al, 1999)

$$Mor(x) = \exp\left(-\frac{x^2}{2}\right) \exp(j\omega_0 x) \quad (3.31)$$

where $j = \sqrt{-1}$ and ω_0 is the frequency of the Morlet wavelet that is normally set to 2π for simplicity. The first part of the Morlet wavelet represents a fast decaying Gaussian envelop that reflects the localization property of CWT. The second part is a complex function with sinusoidal characteristics. A CWT coefficient is a correlation between the signal and the scaled, shifted version of the wavelet. As a complex Morlet wavelet is used, the resultant coefficient is also a complex number whose magnitude would reveal the time-scale feature of the signal.

When a signal is transformed into the time-scale domain, the maximum coefficient along the scale direction is called a CWT ridge at a specific position. Figure 3.2(a) shows a 1-D fringe signal with high instantaneous frequency at the center. A CWT magnitude map is shown in Fig. 3.2(b). (To avoid the inherent edge distortion error, 50 pixels at the boundary are excluded.) The bright stripe is the CWT ridge, where CWT magnitude is the largest along the scale direction.

Mathematically, a fringe pattern (Eq. (3.1)) with slow-varying modulation intensity I_M has a ridge function given by (Liu et al, 2003)

$$S(a_r, b) = \frac{\sqrt{2\pi}}{2} I_M \exp\left(\pm \frac{j\omega_0 b}{a_r}\right) \quad (3.32)$$

where $a_r = \omega_0/\omega_s$ is the scale of the ridge, and ω_s is the instantaneous frequency of the signal at position b . As the local fringe density can be described by an instantaneous frequency, the fringe density estimation is equivalent to a measure of the scale at CWT ridge.

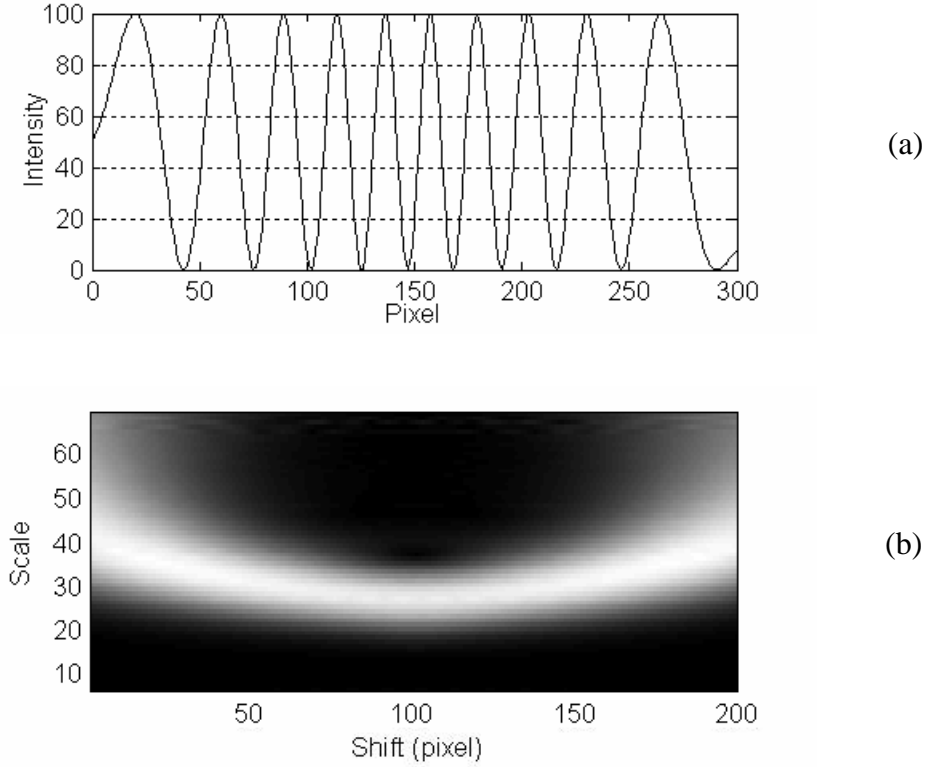


Fig. 3.2 (a) Sinusoidal signal with high frequency at the center;
(b) CWT magnitude map.

The ridge detection algorithm used is a global maximum extraction method

$$a_r(b) = \max \{ |S(a, b)|, \quad a \in [a_{\min}, a_{\max}] \} \quad (3.33)$$

where $a_r(b)$ represents the scale of the ridge point associated with position b , $|S(a, b)|$ is the magnitude of CWT coefficients with a varying in a prior chosen range $[a_{\min}, a_{\max}]$, and $\max\{\dots\}$ denotes the global maximum. A global instead of a local maximum is used because the signal is assumed to have only one dominant frequency. However, the local maxima extraction should be used when analyzing a signal with multiple dominant frequency components (Mallat, 1999). The fringe density is given by

$$den(b) = \frac{1}{M} \sum_{m=b-M/2}^{b+M/2} \frac{\omega_0}{a_r(m)} \quad (3.34)$$

where $den(b)$ represents the fringe density at position b , and M is number of neighboring points used in filtering.

When a 2-D signal is studied, the CWT is applied to each row and column respectively. The fringe density components in the x and y directions are

$$den_x = \frac{1}{MN} \sum_{m=x-M/2}^{x+M/2} \sum_{n=y-N/2}^{y+N/2} \frac{\omega_0}{a_{r,x}(m,n)} \frac{|S[a_{r,x}(m,n),b]|}{\sqrt{|S[a_{r,x}(m,n),b]|^2 + |S[a_{r,y}(m,n),b]|^2}} \quad (3.35)$$

$$den_y = \frac{1}{MN} \sum_{m=x-M/2}^{x+M/2} \sum_{n=y-N/2}^{y+N/2} \frac{\omega_0}{a_{r,y}(m,n)} \frac{|S[a_{r,y}(m,n),b]|}{\sqrt{|S[a_{r,x}(m,n),b]|^2 + |S[a_{r,y}(m,n),b]|^2}} \quad (3.36)$$

where den_x and den_y represent the x and y direction fringe density component at point (x, y) , $a_{r,x}$ and $a_{r,y}$ represent the scale of the ridge point (m, n) with CWT applied in the x and y direction respectively, M and N show the filtering window size, and the CWT magnitudes $|S[a_{r,x}, b]|$ and $|S[a_{r,y}, b]|$ measured respectively in the x and y directions are proportional to the fringe modulation I_M (Eq. (3.32)). The higher the magnitude (fringe modulation), the more reliable is the detected density component and vice versa. The overall 2-D fringe density can be approximated as

$$den(x, y) = \sqrt{den_x^2(x, y) + den_y^2(x, y)} \quad (3.37)$$

Based on the fringe density information, an algorithm can be developed to adaptively choose a suitable processing window size for spatial analysis techniques such as adaptive filtering (Zhi and Johansson, 1991; Davila et al, 1994, 1995 and 1996),

direct correlation (Schmitt and Hunt, 1997), and regularized phase-tracking (Servin et al, 1997). This could achieve an optimal balance between noise reduction and signal preservation.

After a phase fringe pattern is smoothened by a filtering technique and processed by a quality-guided phase unwrapping algorithm, noise and discontinuous 2π phase jumps should have been cleared. The relationship between phase values and physical quantities being measured is established. However, in some of the data-recording techniques such as the fringe projection profilometry, carrier fringes are incorporated to facilitate data recording. The carrier fringe will subsequently introduce a carrier phase component in an unwrapped phase map, which hinders the evaluation of measurement results. In the next section, a carrier phase component removal technique which forms the final stage of fringe analysis is developed.

3.3 Carrier phase component removal

Carrier fringes are widely incorporated in fringe projection measurement. A fringe pattern with carrier can be expressed as

$$I(x, y) = I_0(x, y) + I_M(x, y) \cos[2\pi f x + \phi(x, y)] \quad (3.38)$$

where f is the frequency of the carrier. The carrier fringes, $\cos(2\pi f x)$, serve as an information carrier for data-recording but would introduce a carrier phase component, $2\pi f x$, in the phase extraction process. Hence, the carrier must be removed from the overall phase distribution to evaluate the phase of interest ϕ .

For parallel illumination geometry, the projected fringes maintain equal spacing on a reference plane and would introduce a linear carrier phase component with a constant f . The linear carrier can be determined by a plane-fitting scheme.

However, in general the form of illumination is non-parallel: divergent for large objects and convergent for small objects; and even if an object is of suitable size, the adjustment of parallel illumination relies on subjective human intervention, which tends to produce errors. In these situations, fringe spacing is not a constant and a nonlinear carrier would be introduced. In this section, a general approach for the removal of a nonlinear carrier phase component is proposed. The theoretical analysis is based on divergent illumination geometry with carrier fringes projected in the x direction. The method is also extended to include a curved surface-fitting approach, which is applicable to various measurement system geometries.

3.3.1 Carrier fringes in the x direction

Figure 3.3(a) shows the geometry of a measurement system with a camera set at a normal view. A divergent beam is projected through grating AB on a reference plane CG. Line CA intersects GB at point O, which has a distance h from the reference plane. A light beam OE is directed at the reference plane at an angle α given by

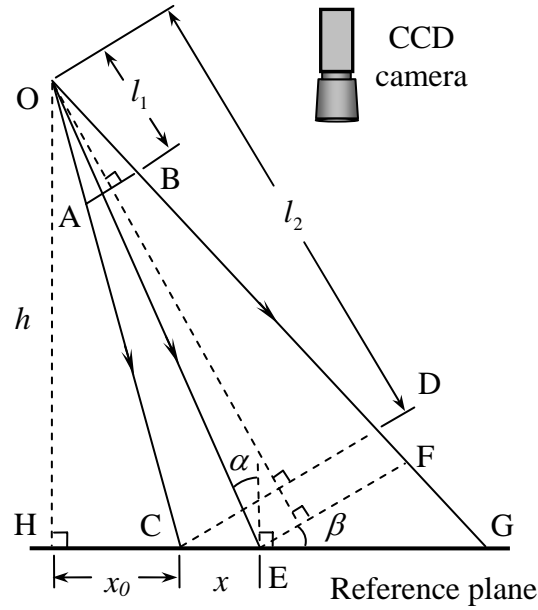
$$\tan \alpha = \frac{x_0 + x}{h} \quad (3.39)$$

where x is the distance between C and E, and x_0 is the distance from C to H. The following derivation expresses the carrier phase function on the reference plane in terms of x and the system geometrical parameters.

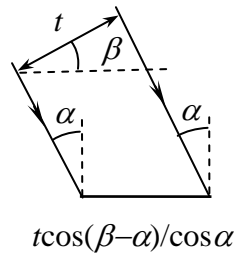
The distances from O to AB and CD are defined as l_1 and l_2 , respectively and lines CD and EF are parallel to AB. The frequency of the fringes in region EF, f_{EF} , is uniform and can be expressed in terms of the frequency of the projection grating f_{AB}

$$f_{EF} = \frac{l_1}{l_2 + x \sin \beta} f_{AB} \quad (3.40)$$

where β is the angle formed by the grating and the reference plane. It is worth noting that β , a constant angle, is different from α , a function of x .



(a)



(b)

Fig. 3.3 (a) Geometry of the measurement system; (b) Vicinity of E

The fringe frequency at x , $f(x)$, on the reference plane is given by

$$f(x) = \frac{f_{EF} \cos \alpha}{\cos(\beta - \alpha)} \quad (3.41)$$

The relationship is clearly seen in the vicinity of E, where at a large magnification, α can be considered to be a constant (Fig. 3.3(b)). A pitch width t is resolved into $t \cos(\beta - \alpha) / \cos \alpha$ on the reference plane and hence Eq. (3.41) can be obtained. Based on Eqs. (3.39-3.41), $f(x)$ can be expressed as

$$\begin{aligned}
 f(x) &= f_{AB} \frac{l_1}{(l_2 + x \sin \beta)} \frac{\cos \alpha}{\cos(\beta - \alpha)} \\
 &= f_{AB} \frac{l_1}{(l_2 + x \sin \beta)} \frac{1}{\cos \beta + \sin \beta \tan \alpha} \\
 &= f_{AB} \frac{l_1}{(l_2 + x \sin \beta)} \frac{h}{h \cos \beta + x_0 \sin \beta + x \sin \beta}
 \end{aligned} \tag{3.42}$$

Based on the geometry of Fig. 3.3(a), it can be seen that

$$l_2 = h \cos \beta + x_0 \sin \beta \tag{3.43}$$

Hence,

$$f(x) = f_{AB} \frac{l_1 h}{(l_2 + x \sin \beta)^2} \tag{3.44}$$

Since l_1 , l_2 , β , f_{AB} , and h are determined from the geometry of the measurement system, the expression for the carrier phase function on the reference plane can be written as

$$\begin{aligned}
 \phi_c(x) &= \int_0^x 2\pi f(u) du + \phi_c(0) \\
 &= 2\pi f_{AB} l_1 h \int_0^x (l_2 + u \sin \beta)^{-2} du + \phi_c(0)
 \end{aligned} \tag{3.45}$$

where $\phi_c(x)$ is the carrier phase function that contains only the carrier phase information, $\phi_c(0)$ is the initial carrier phase angle, and u is a dummy variable for integration. Normally, it is necessary to solve for the integral in Eq. (3.45) and determine the unknown geometrical parameters directly.

Instead of using a rigorous expression of $\phi_c(x)$, the proposed method uses a power series expansion of $\phi_c(x)$. In addition, instead of directly quantifying the geometrical parameters, the method determines unknown coefficients in the power series. It should be noted that the term in Eq. (3.45) is a binomial form. An analytical binomial form can be expanded as a power series within its convergence range. Hence, the term can be written as

$$(l_2 + u \sin \beta)^{-2} = \sum_{n=0}^{\infty} p_n \left(\frac{u \sin \beta}{l_2} \right)^n, \text{ converges with } \left| \frac{u \sin \beta}{l_2} \right| < 1 \quad (3.46)$$

where p_n are unknown coefficients. As the values of p_n are not of particular interest, Eq. (3.46) can be simplified in terms of unknown coefficients b_n

$$\sum_{n=0}^{\infty} p_n \left(\frac{u \sin \beta}{l_2} \right)^n = \sum_{n=0}^{\infty} b_n u^n \quad (3.47)$$

Further, provided that the convergence condition is satisfied, Eq. (3.47) remains a series after integration. Consequently, the carrier function can be rewritten in a simple expression

$$\phi_c(x) = \sum_{n=0}^{\infty} a_n x^n \quad (3.48)$$

where a_n are the coefficients to be determined. By comparing Eq. (3.43) with Eq. (3.48), it can be seen that instead of determining the geometrical parameters, it is only necessary to determine the coefficients in a power series.

A least squares method is developed to determine a_n for $n = 0, 1, \dots, N$, where N is a number that provides a reasonably good approximation to $\phi_c(x)$. An error function is defined as

$$Er(a_0, a_1, \dots, a_N) = \sum_{x \in U} [a_0 + a_1 x + \dots + a_N x^N - \phi_{c,\text{exp}}(x)]^2 \quad (3.49)$$

where U denotes the domain of all points on the reference plane, and $\phi_{c,\text{exp}}$ refers to an experimentally obtained unwrapped phase value. To fit the power series to $\phi_{c,\text{exp}}$ with minimal errors, the partial derivatives of Er with respect to a_0, a_1, \dots, a_N are set to zero. This would result in $N + 1$ linear equations, based on which $N + 1$ unknown coefficients can be obtained. The linear equations can be written in a matrix form

$$\mathbf{X}_{(N+1) \times (N+1)} \cdot \mathbf{A}_{(N+1) \times 1} = \mathbf{B}_{(N+1) \times 1}$$

where $\mathbf{X}_{(N+1) \times (N+1)} = \sum_{x \in U} \begin{bmatrix} 1 & x & \dots & x^N \\ x & x^2 & \dots & x^{N+1} \\ \dots & \dots & \dots & \dots \\ x^N & x^{N+1} & \dots & x^{2N} \end{bmatrix}$

$$\mathbf{A}_{(N+1) \times 1} = [a_0 \quad a_1 \quad \dots \quad a_N]^T,$$

$$\mathbf{B}_{(N+1) \times 1} = \sum_{x \in U} [\phi_{c,\text{exp}}(x) \quad \phi_{c,\text{exp}}(x)x \quad \dots \quad \phi_{c,\text{exp}}(x)x^N]^T, \quad (3.50)$$

where T represents the transpose. The coefficients a_0, a_1, \dots, a_N are subsequently substituted into Eq. (3.48) to obtain $\phi_c(x)$. This value is then subtracted from the overall phase distribution to remove the nonlinear carrier phase component.

3.3.2 Carrier fringes in an arbitrary direction

The theoretical development presented in the previous section is only applicable to a special case where the carrier fringes are in the x direction. This means that the carrier phases do not change with the spatial variable y . In this section, the least squares approach is extended to a general situation, in which the carrier phase component is a nonlinear function of both the x and y variables. For simplicity the theoretical derivation will not be based on a specific experimental setup, since there are many types of system geometry that would lead to a nonlinear carrier. Instead, it is assumed that the carrier phase function can be approximated by a series expansion.

Compared with the 1-D situation, which is essentially a higher-order curved line-fitting, the 2-D situation is basically a higher-order curved surface-fitting. The mathematical expression for a curved surface of the N th-order is given by

$$\begin{aligned} \phi_c(x, y) = & a_{0,0} + a_{0,1}x + \cdots + a_{0,N-1}x^{N-1} + a_{0,N}x^N \\ & + a_{1,0}y + a_{1,1}xy + \cdots + a_{1,N-1}x^{N-1}y \\ & + \cdots + \cdots + \cdots \\ & + a_{N-1,0}y^{N-1} + a_{N-1,1}xy^{N-1} \\ & + a_{N,0}y^N \end{aligned} \quad (3.51)$$

where there are $(N+1)(N+2)/2$ unknown coefficients. The terms that carry the form $x^{px}y^{py}$ (px and py represent the power of x and y , respectively) take into account rotation in the direction of the carrier fringes and distinguish surface-fitting from a simple combination of line-fitting in the x and y directions. An error function is defined as

$$Er(a_{0,0}, \dots, a_{0,N}, \dots, a_{N,0}) = \sum_{(x,y) \in U} [\phi_c(x, y) - \phi_{c,\text{exp}}(x, y)]^2 \quad (3.52)$$

where $\phi_c(x, y)$ represents a series (for simplicity); U and $\phi_{c,\text{exp}}(x, y)$ are as defined in Eq. (3.49). To minimize errors, the partial derivatives of Er with respect to each of the unknown coefficients are set to zero. This would produce $(N + 1)(N + 2)/2$ linear equations, from which the unknowns can be obtained. On substituting the calculated coefficients into Eq. (3.50), one can obtain an estimated carrier phase function with minimal error. By subtracting carrier phases from the overall phase distribution, the carrier phase component is removed.

The main difficulty in the implementation of the algorithm is in solving the $(N + 1)(N + 2)/2$ linear equations. A C++ source code package, in which a numerical analysis method (Vetterling et al, 2002) is incorporated for solving the linear equations, is shown in Appendix A.

CHAPTER FOUR

EXPERIMENTAL WORK

To verify the proposed theoretical work, experimental systems for the fringe projection and digital speckle shearing interferometry (DSSI) measurement were developed. The surface profile of several test specimens were obtained by the fringe projection system; and the deformation characteristics of a centrally loaded circular thin plate was recorded by the DSSI system. The equipment and experimental procedures are described in the following sections.

4.1 Fringe projection system

4.1.1 Equipment

The fringe projection system consisted of a programmable liquid crystal display (LCD) projector, a CCD camera, a 3-D translation stage and a computer, as shown in Fig. 4.1. The LCD projector (JENOPTIK Laser, Optik) is specifically designed for an application that required a flexible dynamic pattern generation. It consisted of an illumination unit (including fan, reflector, halogen lamp and condenser), a LCD-modulator and an objective lens. The LCD achieved a resolution of 832×624 pixels. Each pixel was assigned a relative transparency level between 0 and 254. A flexible lens holder was installed at the front end of the projector so that camera lenses of different magnifications could be used for specimens of different dimensions. For the measurement of a relatively large object, a camera lens with small magnification (< 1) could be used to project a divergent pattern on the specimen; while for a small object, a microscopic lens could be used to focus the pattern onto a smaller area.

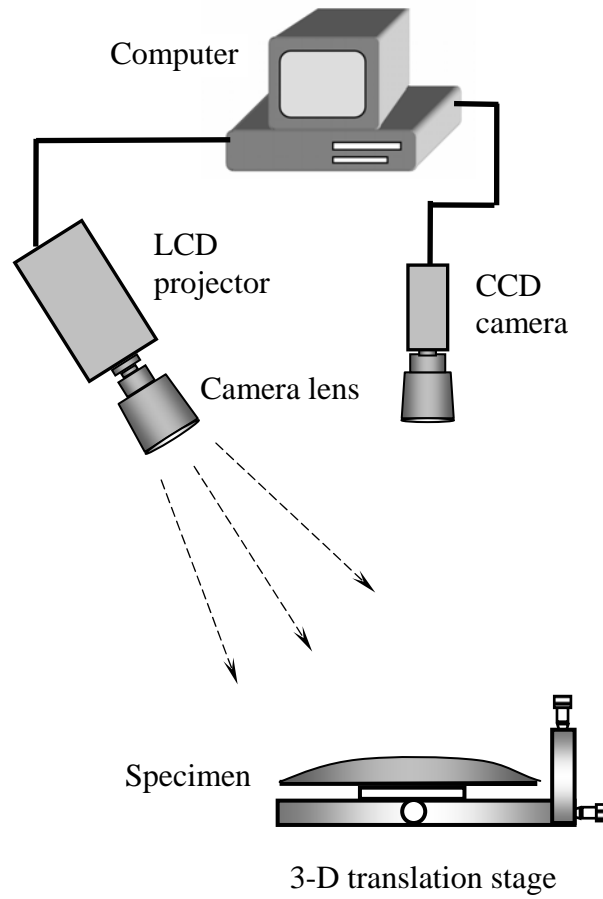


Fig. 4.1 Schematic setup of fringe projection system

The CCD camera was set at a normal view. Although alternative arrangements, such as oblique projection & oblique observation, or normal projection & oblique observation are applicable to 3-D shape encoding, the best observation manner is in a normal viewing angle. With this arrangement, the image distortion is minimal. Similar to the camera lens used for the LCD projector, the camera lens for the CCD should be accordingly selected based on the dimension of a specimen.

The 3-D translation stage functioned as a holder for the specimen. It provided a convenient and accurate means of alignment. Moreover, for calibration of the system, one could shift a specimen using the stage by a given distance and calculate the phase

difference of a point before and after shifting. The ratio of the shifted distance to the phase difference is used as a calibration factor for the phase-to-height conversion.

Figure 4.2 shows the actual experimental setup for the measurement of a fish model.

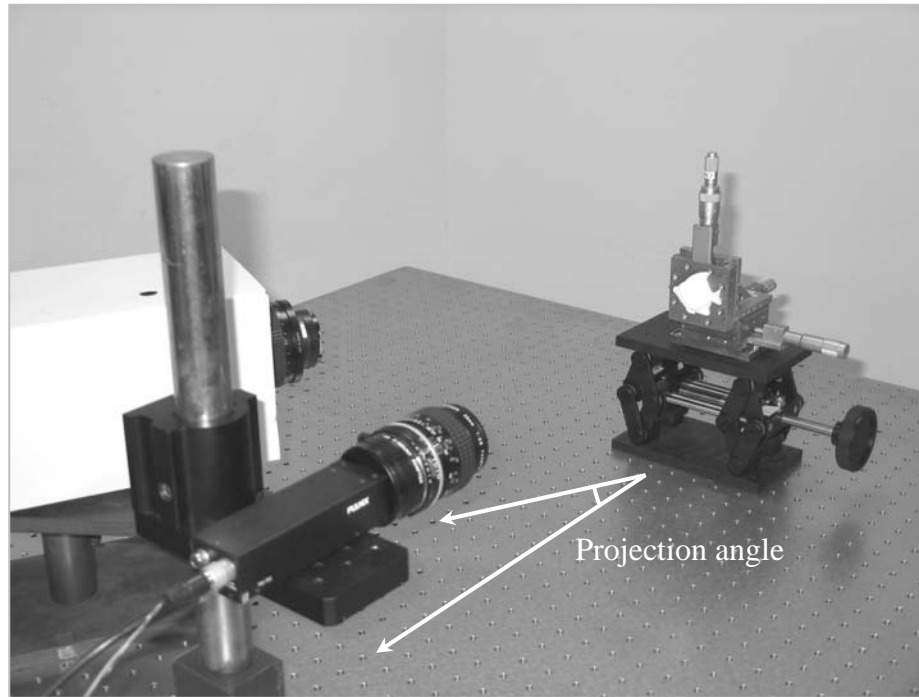


Fig. 4.2 Setup of fringe projection system

4.1.2 Experiment

The data-recording procedure was similar for most specimens, regardless of their particular features. Phase-shifted fringe patterns were generated by a computer and loaded onto a LCD projector through a serial port. The phase shift between consecutive fringe patterns was introduced digitally and thereby phase-shifting errors were negligible. The CCD camera captured the projected fringe pattern on the specimen surface and transferred the digital image data to the computer, which stored them for later processing. A specifically developed program synchronized the fringe

pattern generation, the LCD projection and the CCD camera image acquisition. Hence, the data-recording process was fully automatic.

Normally, there is a nonlinear effect in the system, which meant that a computer-generated sine pattern would encounter intensity distortion when it is projected on a specimen and imaged by a CCD camera. In this study, a simple experimental strategy was adopted to reduce the nonlinear effect. The system response was studied by projecting intensity patterns in a full transparency range $[0, 254]$ and the recorded intensity was plotted against the input transparency. The most linear part of system response was taken as the actual input to the LCD projector.

Theoretically, the system sensitivity would increase with the projection angle. However, a large angle would induce an undesirable shadow effect, which is an inherent problem of projection methods. Therefore, during the alignment of the experimental setup for each specimen, care should be taken to reduce projection shadow and maintain system sensitivity.

4.2 Digital speckle shearing interferometry system

4.2.1 Equipment

Figure 4.3 shows the actual experimental setup of the digital speckle shearing interferometry (DSSI) system, which was mounted on a vibration-isolation table (Newport RS 2000TM). Theoretically, DSSI is more insensitive to vibration than electronic speckle pattern interferometry (ESPI) due to its shorter optical path length of the objective and reference beams. Therefore, a vibration-isolation table is not indispensable, if one just needs qualitative analysis of DSSI speckle patterns. In this thesis, however, the proposed three-frame phase-shifting algorithm relied largely on the introduction of an accurate phase shift. Hence, vibration isolation was necessary,

which could prevent environmental noise from deteriorating the quality of a speckle pattern.

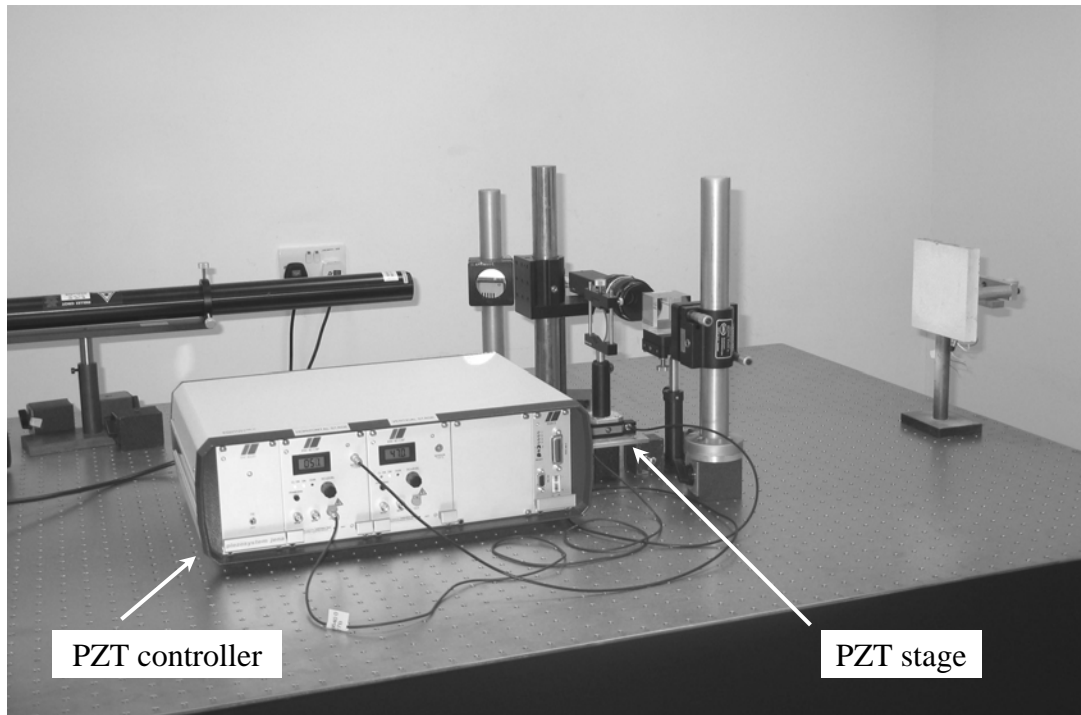


Fig. 4.3 Setup of DSSI system

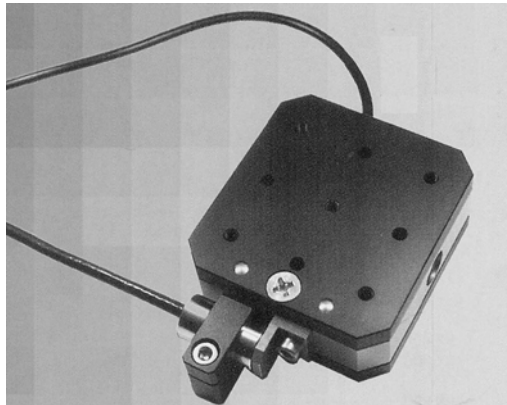


Fig. 4.4 Piezosystem Jena, PX300 CAP, PZT stage

The phase shift between speckle patterns was achieved by a PZT stage, as indicated in Fig. 4.3. It was of type PX300 CAP made by Piezosystem Jena (Fig. 4.4) and could produce a maximum horizontal displacement of 300 μm . Furthermore, it

could be closed-loop controlled with a position accuracy of 0.05% at a full motion and it provides a resolution of 5 nm.

4.2.2 Experiment

Figure 4.5 shows the schematic setup of the DSSI system. A coherent light beam emitted from a He-Ne laser (632.8 nm) was expanded and illuminated the test specimen (a circular thin plate). The plate was boundary fixed and loaded by a micrometer attached at the back. The laser beam reflected from the specimen surface was directed onto mirrors 1 and 2 via a beam splitter. The beam splitter also facilitated the superposition of the virtual images of the specimen. The resultant interferometric speckle pattern was recorded by a CCD camera.

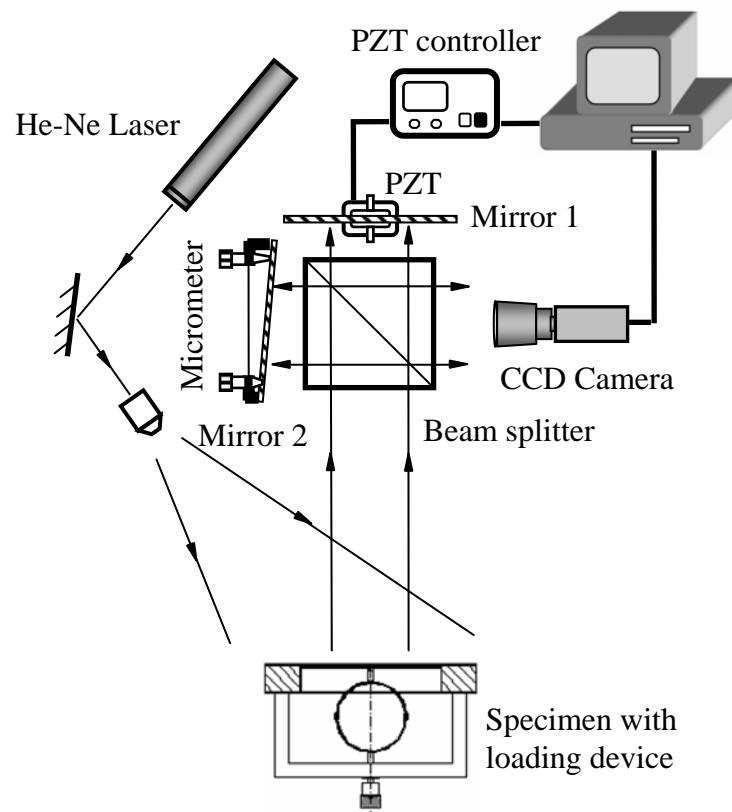


Fig. 4.5 Schematic setup of DSSI system

The distance from the mirrors to the beam splitter was less than 3 cm in the actual experiment. The short optical path length ensured high tolerance to environmental vibration. Mirror 1 was mounted on the PZT stage and mirror 2 was mounted on a rig fitted with a micrometer. The tilt of mirror 2, adjustable through the micrometer, provided the amount of shearing between images of the specimen recorded on the CCD camera. The larger the shearing, the higher is the system sensitivity to deformation change. However, a large shearing would produce high density fringes that hindered low-pass filtering noise removal. As the proposed three-frame algorithm had good tolerance to dense speckle fringes, a relatively large shearing (5 mm) was used in the experiment. The exact amount of shearing could be measured based on the image of a mark line labeled on the thin plate. Since the recorded image has two mark line images, as indicated in Fig. 4.6, the distance of shearing is the distance between the lines and can be conveniently measured in pixel unit. The coefficient of pixel-to-actual distance is the ratio between distances of plate corner points measured on the image (pixel) and on the specimen (actual distance), respectively.

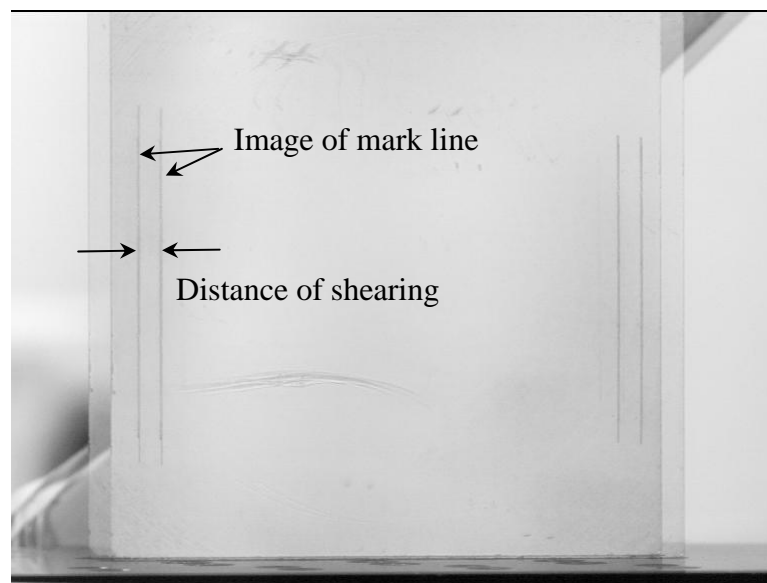


Fig. 4.6 Determination of the amount of shearing incorporated

In the data-recording process, control commands were initiated from a computer and converted to a voltage through a PZT controller. The image acquisition and PZT movement were synchronized by a program and the voltage increment applied on the PZT was constant. Subsequently, a constant phase shift between speckle patterns was achieved. Two sets of phase-shifted speckle patterns were captured before and after manually loading of the specimen. With conventional Carré's technique (four-frame algorithm), eight speckle patterns were required altogether; while based on the proposed three-frame algorithm, only six were needed.

4.3 Specimens

Various specimens were used to test the validity of the proposed phase evaluation techniques. Specimen A is a ridge-like object, as shown in Fig. 4.7.

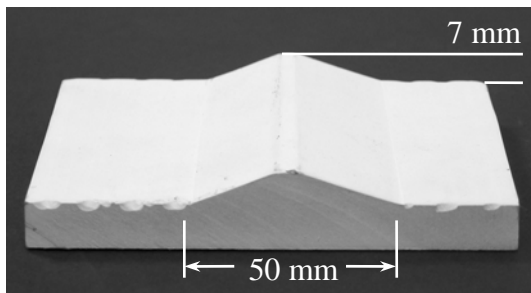


Fig. 4.7 Specimen A

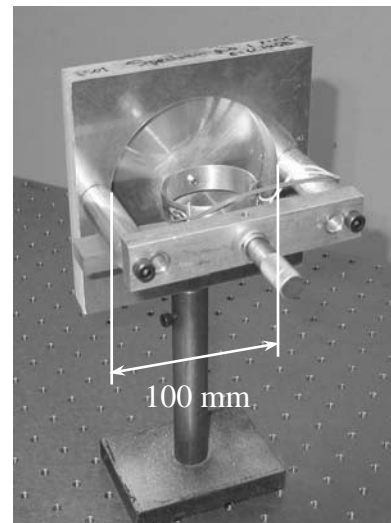


Fig. 4.8 Specimen B

Its shape was measured by the fringe projection system and the proposed three-frame phase-shifting algorithm was tested on projected fringe patterns. The three-frame algorithm was also validated on a circular thin plate (specimen B, Fig. 4.8) for speckle

pattern analysis. The deformation introduced by manually loading of the micrometer was recorded using the DSSI system.

Specimen C is a fish model shown in Fig. 4.9. The fin and tail of the fish model contained drastic surface profile changes, which hindered phase extraction and phase quality identification. A sawtooth profilometry method was used to retrieve a wrapped phase map and a plane-fitting quality criterion was developed to minimize unwrapping errors around the shadowed phase data. Specimen D, a hemisphere with a groove at the center (Fig. 4.10), represented another kind of challenge in a phase unwrapping process. Only with an advanced phase quality indicator, could the step changes at the top and bottom of the groove be detected. The temporal fringe contrast (TFC) and the proposed spatial fringe contrast (SFC) criteria were tested on the specimen.

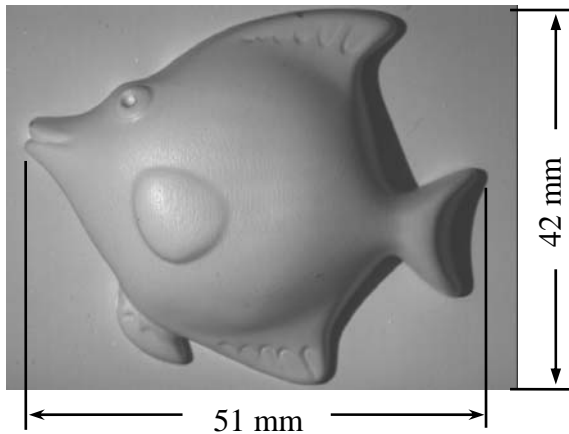


Fig. 4.9 Specimen C

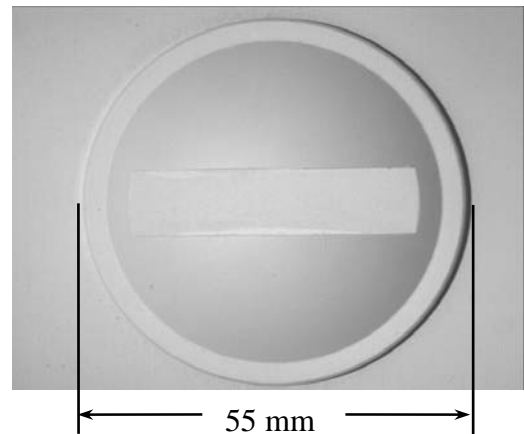


Fig. 4.10 Specimen D

Specimen E, a half ball (Fig. 4. 11), and specimen F, a Singapore coin (Fig. 4.12), were used to validate the proposed carrier removal technique. Since the proposed series expansion function (Eq. 3.51) can be used to approximate a diverse form of carrier phase function, the geometrical parameters of the experimental setup need not be measured precisely; however, they should satisfy the convergence conditions in Eqs. (3.46). In the experiment, the geometrical parameters including the

projection angle and various distances were measured based on marks (screw holes) on the vibration isolation table (as shown in Fig. 4.2). The projection angle β was set to 20° ; d and l_2 were respectively 20 cm and 60 cm. The distance h (distance between the LCD panel to the reference plane) was greater than 50 cm; while the distance corresponding to $x_0 + x_{\max}$ was less than 30 cm (x_{\max} refers to the maximum value of x in the field of view). Hence, both convergence conditions were satisfied. Since parameters h , d , x_{\max} , l_2 and β are interrelated, the convergence conditions necessitate the maximum projection angle to be less than 45° . This was readily satisfied in most fringe projection systems, since to avoid projection shadow and to achieve relatively uniform illumination intensity, the projection angle should normally be less than 45° .

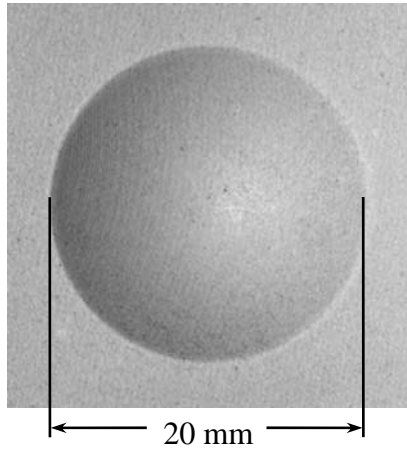


Fig. 4.11 Specimen E



Fig. 4.12 Specimen F

CHAPTER FIVE

RESULTS AND DISCUSSION

5.1 Wrapped phase extraction**5.1.1 Three-frame algorithm with an unknown phase shift**

The three-frame phase-shifting algorithm is first applied on the phase extraction from projected fringe patterns, followed by a speckle pattern analysis using the difference of phases.

5.1.1.1 Processing of fringe patterns

Figure 5.1 shows three phase-shifted fringe patterns (512×512 pixels) projected on specimen A (see section 4.3).

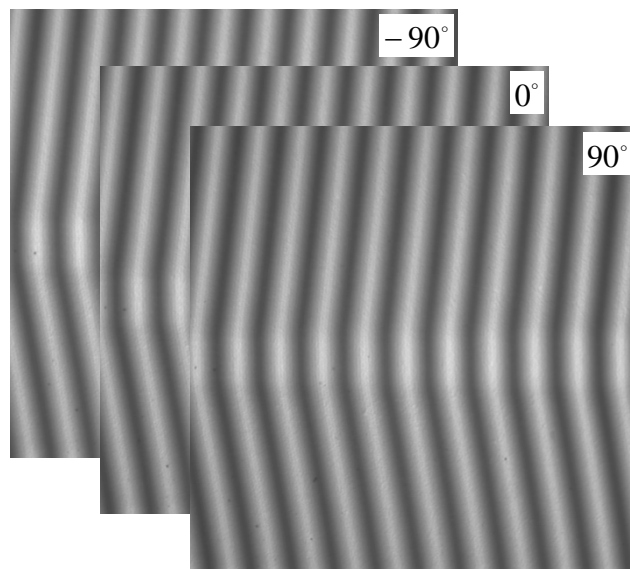


Fig. 5.1 Fringe pattern on specimen A

As the illumination intensity is uniform, the background frequency component can be separated from that of the phase signal in frequency domain (Kerr et al, 1989, 1990).

Firstly, the spectrum of the fringe pattern is calculated by Fast Fourier Transform (FFT) algorithm. An $N \times N$ pixel window at the spectrum center is then extracted as the background frequency component. A large value of N (e.g. 7 or 9) can be used if the background intensity variation is relatively large; while a small value of N (e.g. 1 or 3) can be used for highly uniform background. An optimal value is usually determined through trial and error, and in this study N is set to 5. On inversely transforming the background frequency component, the background intensity can be obtained.

Normally, it is difficult to investigate the accuracy of the background estimation with an unknown phase shift. In the present study, however, the accuracy could be accessed, since a known phase shift ($\pi/2$) is introduced digitally by a program and the actual background intensity is retrievable from the generalized phase-shifting algorithm (Morgan, 1982; Greivenkamp, 1984). Figure 5.2 shows the difference between background intensity obtained using FFT and phase-shifting.

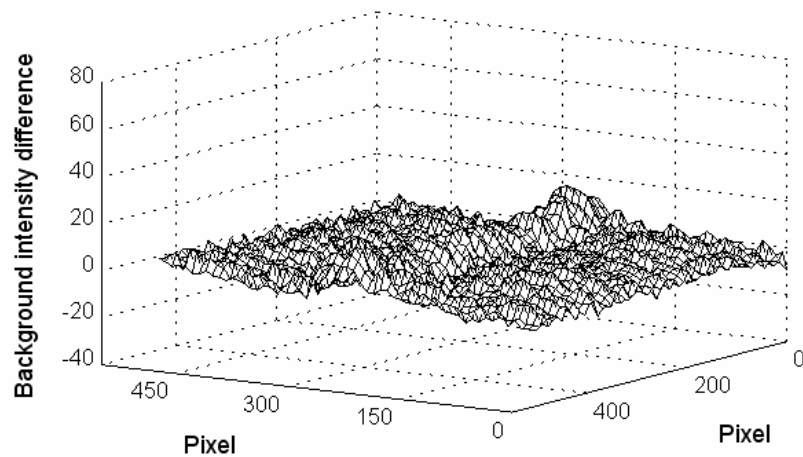


Fig. 5.2 Background intensity difference of FFT and phase-shifting

As can be seen, the maximum difference (15%) is at the center part of the specimen, where the surface receives a stronger light intensity than other regions (Fig. 5.1). In this region, the background intensity encounters a relatively higher variation and

therefore a 5×5 window is insufficient to capture the intensity changes. However, the mean difference is less than 3% (3 gray levels) and it can be ignored compared with the fringe modulation (200 gray levels).

After the background is removed, the proposed three-frame algorithm detects a 89.7° phase shift. Compared with the theoretical 90° phase shift, the discrepancy is less than 0.5%. An extracted wrapped phase map and a phase difference map (difference between wrapped phase map obtained by the proposed method and the standard 3-frame 90° phase-shifting algorithm) are shown in Fig. 5.3. It is seen that the maximum difference is less than 3%. The accuracy is mainly achieved by the background removal process. With uniform fringe pattern background, a high-pass filter could eliminate DC component and subsequent phase extraction would have comparable accuracy as the standard 3-frame 90° phase-shifting algorithm.

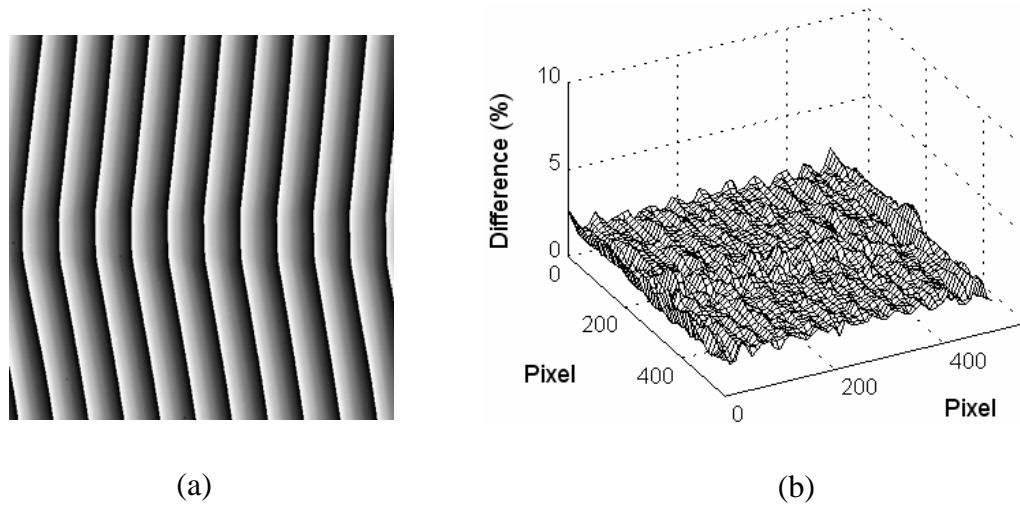


Fig. 5.3 (a) Wrapped phase map; (b) phase difference map

5.1.1.2 Processing of speckle patterns

Specimen B (see section 4.3) is studied using the DSSI system. Figure 5.4 shows a speckle fringe pattern of the specimen obtained by the subtraction of a speckle pattern

before and after deformation. Since a small load (1.2 N) is applied, the resultant fringe density is relatively low. The conventional approach (Santoyo F. M. et al, 1988) to the background and speckle removal by using band-pass filtering is first tested. The speckle fringe pattern is transformed to a frequency domain and a band-pass filter with properly chosen cut-off frequencies is used to remove both the background (low-frequency) and the speckle (high-frequency) components.

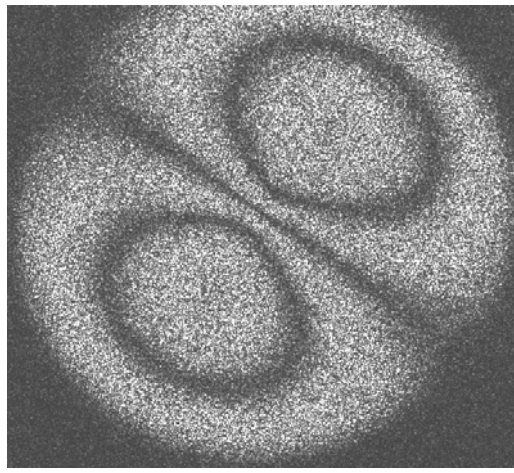
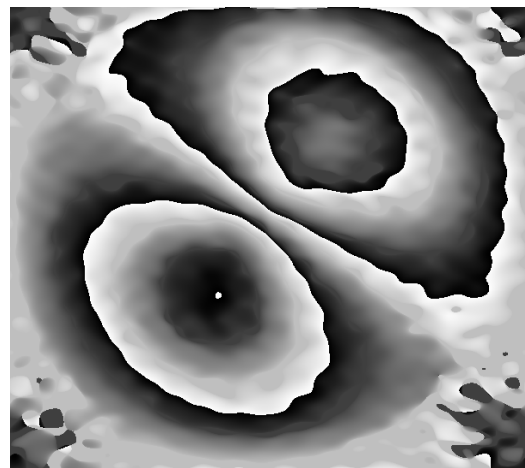


Fig. 5.4 Speckle fringe pattern (1.2 N load)



(a)



(b)

Fig. 5.5 (a) Smoothed fringe pattern by band-pass filtering;
(b) Wrapped phase map (1.2 N load)

On inversely transforming the filtered spectrum, a smoothened fringe pattern is obtained, as shown in Fig. 5.5(a). The subsequent phase extraction is performed on three filtered, phase-shifted fringe patterns, which are generated by subtracting each of the speckle patterns before deformation from the one after deformation. The extracted wrapped phase map is shown in Fig. 5.5(b). A key factor in this process, the cut-off frequencies of the band-pass filter, is chosen based on prior knowledge of the fringe pattern (Kerr, 1989). An optimal filtering window size can only be obtained through trial and error, which is a drawback of the method.

Figure 5.6(a) shows a wrapped phase map retrieved by three-frame algorithm. Although it contains noise due to speckle de-correlation (Creath, 1985), the phase signal is in fact better preserved than that shown in Fig. 5.5(b).

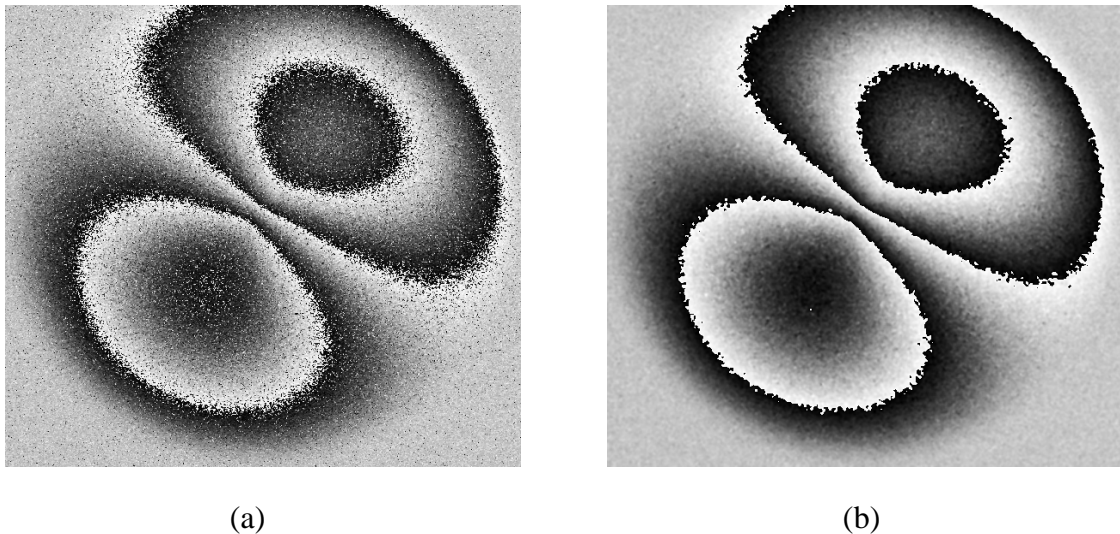


Fig. 5.6 (a) Wrapped phase map obtained using 3-frame algorithm;
(b) Phase map smoothened by sine / cosine filter (1.2 N load)

This is verified by applying a sine/cosine filter for noise reduction (Aebischer and Waldner, 1999). The sine and cosine of the wrapped phase are calculated and individually smoothened by a 3×3 mean filter. A filtered phase map (Fig. 5.6(b)) is obtained from the four-quadrant arctangent of the sine and cosine patterns. Compared

with Fig. 5.5(b), the present phase map is of better quality, especially at corners of the image, where the band-pass filtering method suffers from image boundary distortion inherent in the FFT process.

When a larger load (5.3 N) is applied on the specimen, the fringe density increases significantly, as shown in Fig. 5.7.

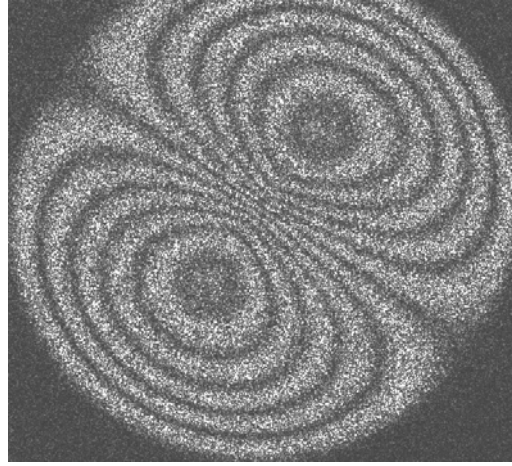
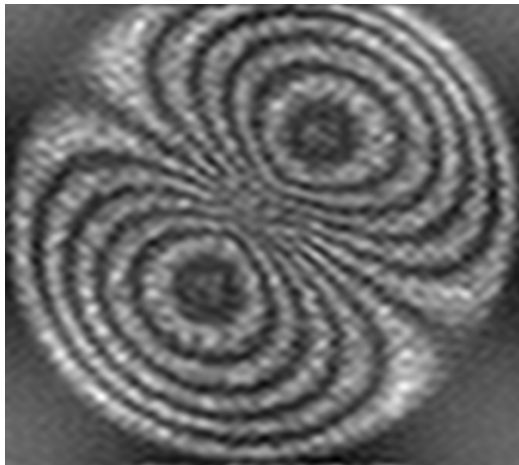


Fig. 5.7 Speckle fringe pattern (5.3 N load)



(a)



(b)

Fig. 5.8 (a) Smoothed fringe pattern by band-pass filtering;
(b) Wrapped phase map (5.3 N load)

A smoothed fringe pattern obtained by the band-pass filtering approach is shown in Fig. 5.8(a). It is seen that speckle noise as well as high-frequency fringes at the center

are removed. Subsequently, the wrapped phase map (Fig. 5.8(b)) shows erroneous phase values at the center. This indicates a serious drawback of the band-pass filtering approach, in which noise reduction would unavoidably deteriorate a phase signal. Figure 5.9 shows a smoothened wrapped phase map obtained by the proposed algorithm. It is especially important to note that the high-frequency phase signal at the center is correctly retrieved. Moreover, in contrast with the band-pass filtering, the proposed speckle background removal algorithm is independent of manual intervention. It also requires less computation time, since only a few mathematical operations are involved in the background intensity estimation.

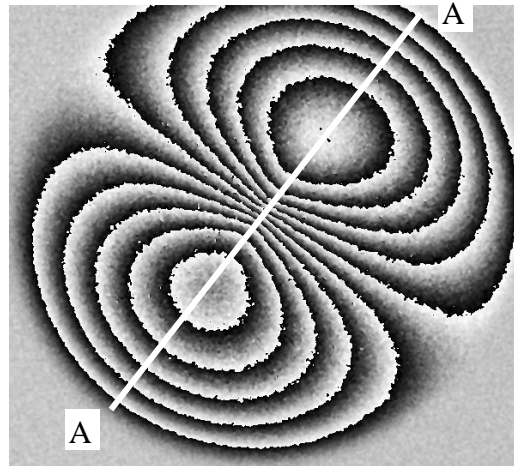


Fig. 5.9 Smoothened wrapped phase map by 3-frame algorithm (5.3 N load)

5.1.1.3 Accuracy analysis

The accuracy of the three-frame algorithm is dependent on the background intensity estimation. For a fringe pattern with slow-varying background, a 5×5 pixel window at the spectrum center can be used as the background frequency component. When inversely transformed, it would result in accurate background intensity. For a speckle pattern, however, the proposed technique provides an approximation to the actual speckle background. The accuracy in this case is related to the unknown phase shift

value. Seventeen sets of phase-shifted speckle patterns are simulated with phase shift in the range of 10° to 170° . Each set contains six speckle patterns with three before and three after deformation. The deformation phase map is also simulated. The proposed method is used to calculate the phase shift and the deformation phases for each set.

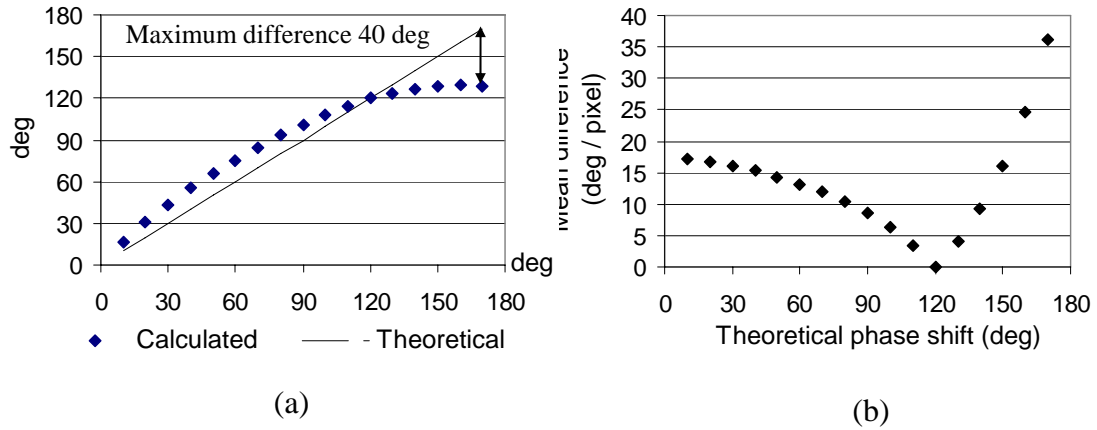


Fig. 5.10 (a) Calculated and theoretical phase shift; (b) Absolute mean difference between calculated and theoretical deformation phase

Figure 5.10(a) shows the calculated and theoretically introduced phase shifts. The most accurate phase shift is at 120° . This is also evident from Eq. (3.13), where the term $1 + 2 \cos \delta$ is zero when $\delta = 120^\circ$ and hence the average intensity equals the background intensity. Figure 5.10(b) shows the absolute mean difference (summation of phase value difference at each pixel divided by the total number of pixels in a phase map) between calculated and theoretical deformation phase. It is seen that the optimal phase shift is again at 120° . In addition, the results show that, for phase shift larger than 120° , discrepancies in the calculated deformation phase would increase drastically. This indicates a limitation of the present technique.

The slope distribution of section A-A indicated in Fig. 5.9 is further compared with the theoretical predication of thin-plate-deformation. As can be seen in Fig. 5.11,

the experimental and theoretical results agree well at the center of the specimen. However, at the boundary of the circular plate, Fig. 5.11 shows that measurement results deviate from the theoretical predication. This could be due to the fact that during manufacturing of the circular thin plate the thickness of the plate cannot be made uniform everywhere. Therefore, if one uses an average thickness to calculate the slope of deformation, the theoretical values would be different from the actual slope. The average difference between experimental and theoretical values is less than 5%, which proves the proposed background removal technique for speckle patterns is validate.

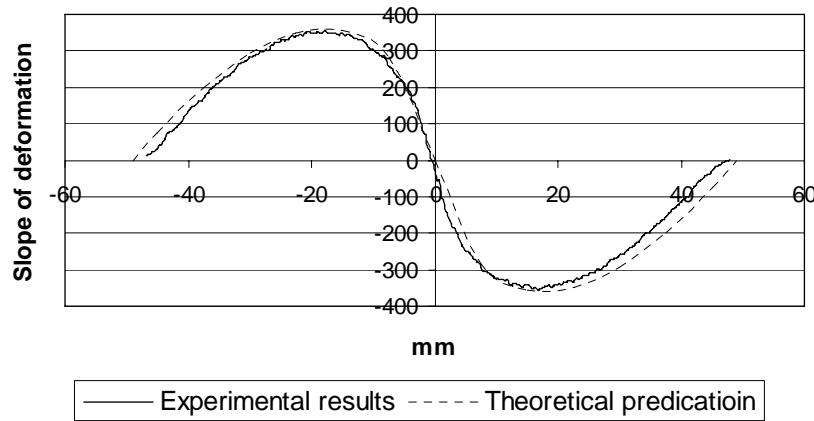


Fig. 5.11 Comparison of the slope distribution of section A-A indicated in Fig. 5.10 obtained by the proposed method and by the theoretical predication of thin-plate-deformation

5.1.2 Sawtooth pattern profilometry

5.1.2.1 Intensity-to-phase conversion

The extraction of phase information from a sawtooth fringe pattern is basically achieved through a linear translation, as described in section 3.1.2. In practice, a recorded sawtooth pattern would encounter shape distortion. Figure 5.12 shows a simulated intensity cross-section recorded on a CCD camera. There are several

intermediate pixels between a peak and valley due to defocus, which has a spatial averaging effect. The recorded intensity of a pixel is the average intensity of a small region on an object surface, which in turn is the average intensity of a few pixels on a LCD projector panel; therefore severe distortion would occur at a local region containing a peak and valley. The sharpness of a sawtooth pattern is reduced and the intermediate pixels do not encode the surface profile. Moreover, if such an intensity pattern is converted to a wrapped phase map, there will not be a 2π phase jump for phase unwrapping. Fang and Zheng (1997) proposed to overcome the problem by using multiple samples such as fringe patterns with different pitches. In this study, an image processing algorithm is used to reset the intensity of intermediate pixels.

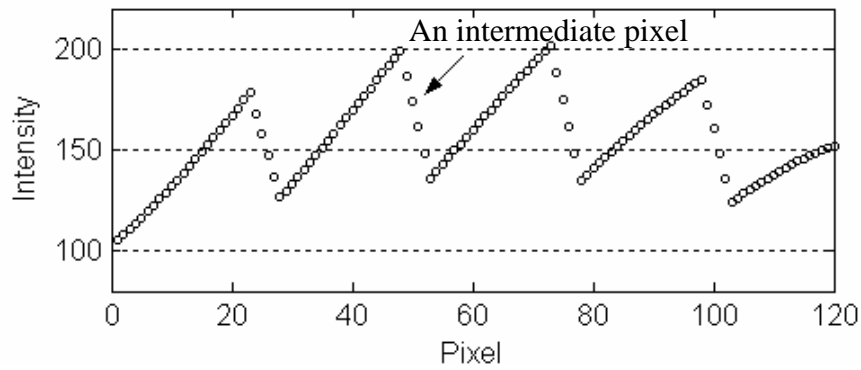


Fig. 5.12 CCD camera-recorded intensity

A program scans each cross-sectional fringe, identifying all of peak and valley values in pairs. An intermediate pixels' intensity is then reset based on the slope of a data line, since it preserves the trend of intensity variation that reflects the trend of shape change. For example, in Fig. 5.12 the intermediate pixel indicated by an arrow is closer to a peak. Its modified intensity would be $I_{peak} + slope \times dist$, where I_{peak} is the intensity of the nearby peak; $slope$ is the slope calculated using data points ahead of the peak; $dist$ represents the distance between the peak and the processed pixel. For an intermediate pixel closer to a valley, its modified intensity can be obtained in a similar

way. Figure 5.13 shows the intensity distribution after processing. As can be seen, the sharpness of the sawtooth pattern is restored and the arrow indicates the modified intensity of the pixel under consideration. Although theoretically the slope-based intensity modification does not retrieve the actual height information from intermediate pixels, it can effectively compensate phase measurement errors and benefits subsequent phase unwrapping process by recovering the data jumps between fringe periods.

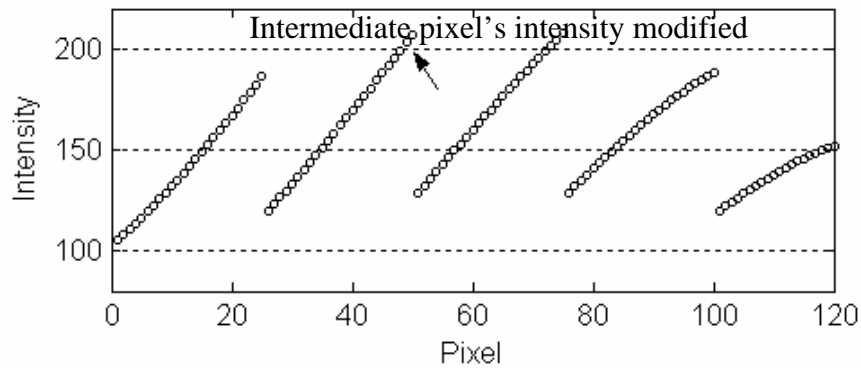


Fig. 5.13 Cross-section after resetting the intensity of intermediate pixels

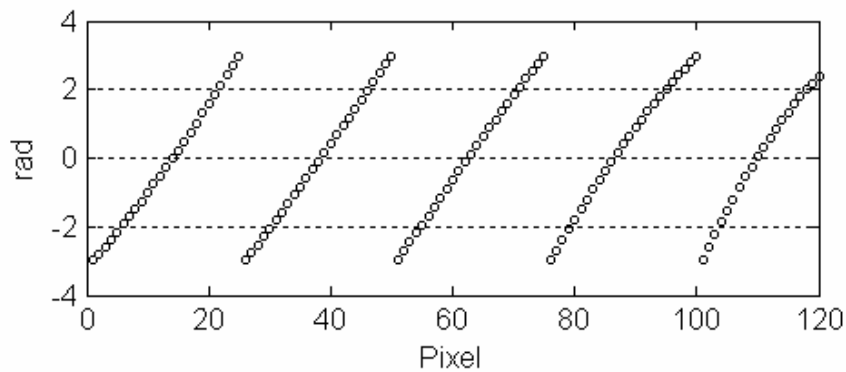


Fig. 5.14 Wrapped phase values obtained from intensities

Non-uniform illumination and reflectance also reduce the uniformity of the recorded intensity distribution, as shown in Fig. 5.13. The pattern has higher background intensity at the center and lower modulation intensity at the right part. As

indicated by the theoretical analysis, local rather than global extremes should be used to calculate the translating parameters for intensity-to-phase conversion. Figure 5.14 shows the wrapped phases obtained. The previously non-uniform background and modulation (Fig. 5.13) are unified.

An actual measurement is implemented on specimen C (see section 4.3). The projected sawtooth pattern is shown in Fig. 5.15. The intensity variations are similar to those in a wrapped phase map with carrier fringes in the x direction. Figure 5.16 shows the intensity along section A-A indicated in Fig. 5.15. As can be seen, there are several intermediate pixels between an adjacent peak and valley, which are similar to the simulated results shown in Fig. 5.12. The arrows point out two typical intermediate pixels that will hinder a phase unwrapping process.

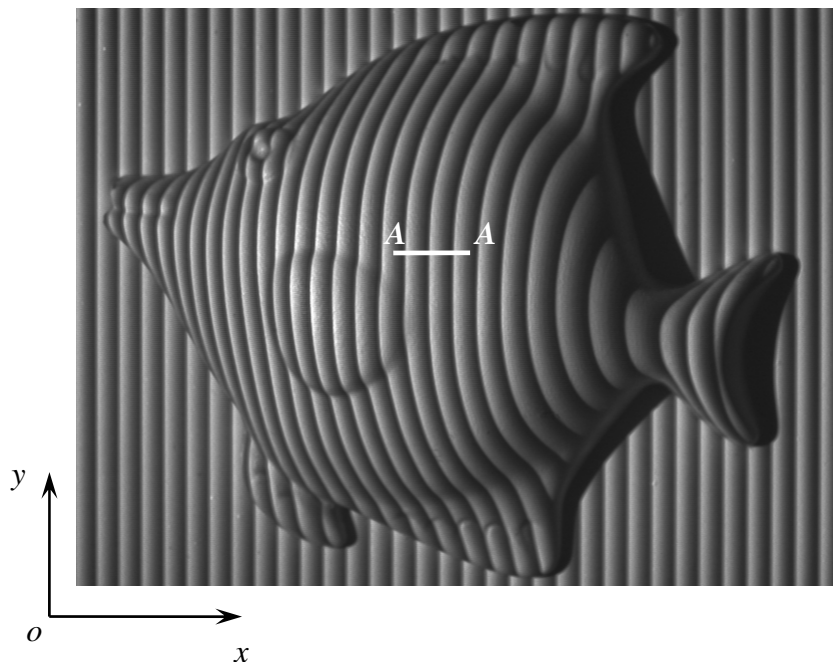


Fig. 5.15 Sawtooth fringe pattern projected on specimen C

Based on the image processing algorithm proposed, the intensity of the intermediate pixels is modified, as shown in Fig. 5.17. It is seen that the sharpness of the sawtooth pattern is retrieved. The intensity modification is based on the slope of

nearby data points. This strategy provides a good approximation to an ideal sawtooth-encoding situation.

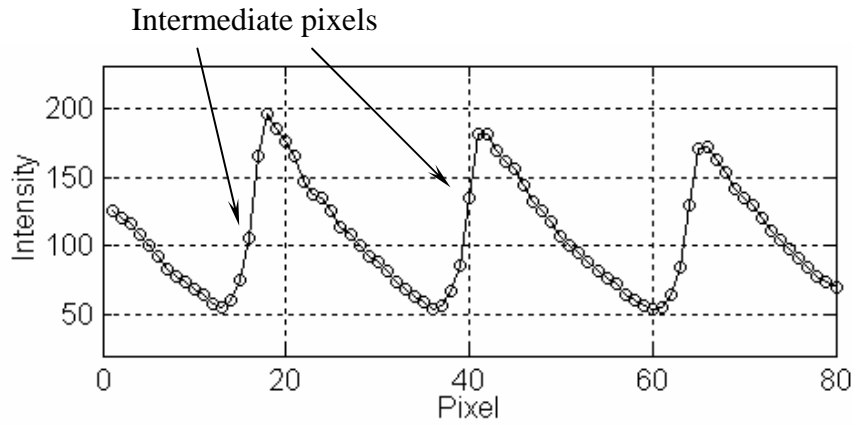


Fig. 5.16 Intensity along section A-A on Fig. 5.15

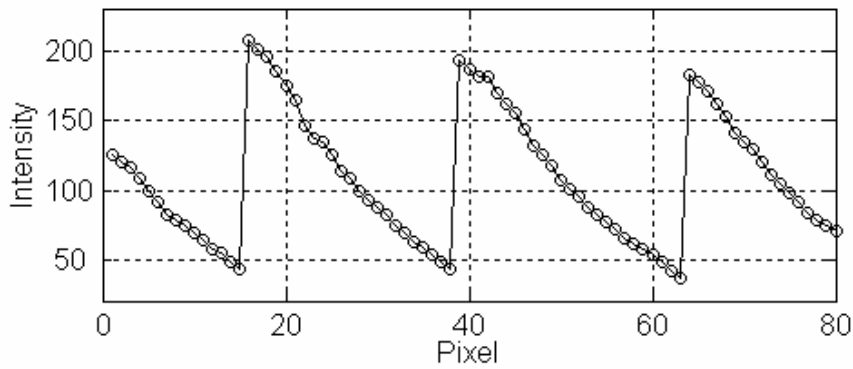


Fig. 5.17 Section A-A after modification of intermediate pixel's intensity

The key to the intensity-to-wrapped phase conversion is the identification of local maximum (peak) and minimum (valley) intensities so that the translating parameters t_1 and t_2 (Eq. (3.16)) associated with each cycle can be obtained. At the present stage, as the intermediate pixels are removed, peaks and valleys are always adjacent to each other, as shown in Fig. 5.17. A specifically developed program labels a local maximum as a peak only if it is accompanied by a local minimum. A similar procedure is applied to the identification of a valley. Such criterion is beneficial for the

reliability of the identification. Otherwise, if peaks and valleys are located only based on local extremes, numerous errors would be encountered because of the many local extremes in shadow areas which are hardly observable to the naked eye.

When local maxima (peaks) and minima (valleys) are located, the translating parameters associated with each cycle can be solved. The intensities of each cycle are then converted to phase angles. Figure 5.18 shows the phase distribution along section A-A after conversion. As can be seen, uniform values of peaks and valleys are obtained; while before conversion (Fig. 5.17), the peaks and valleys are non-uniform.

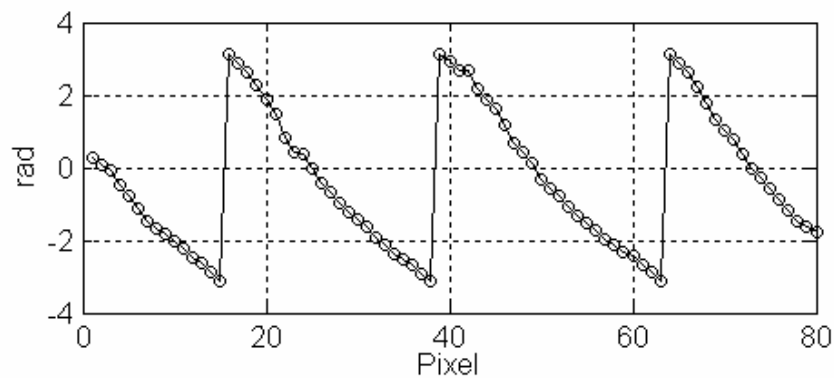


Fig. 5.18 Phase values of section A-A converted from intensities

Subsequently, a wrapped phase map shown in Fig. 5.19 is extracted. It is worth noting that, during data-processing, only one sawtooth pattern is required and therefore the method is potentially suitable for recording a transient event. To unwrap the wrapped phase map, a plane-fitting-based quality criterion is used, which will be discussed in the section on phase quality identification. The following section discusses the phase measurement accuracy of the sawtooth profilometry technique.

5.1.2.2 Accuracy analysis

The results of one-frame sawtooth pattern profilometry technique are compared with those of phase-measuring profilometry (PMP) (Srinivasan et al, 1984) using

measurement obtained from a contact profilometer. Figure 5.20(a) shows the height of section *B-B*, as indicated in Fig. 5.19.

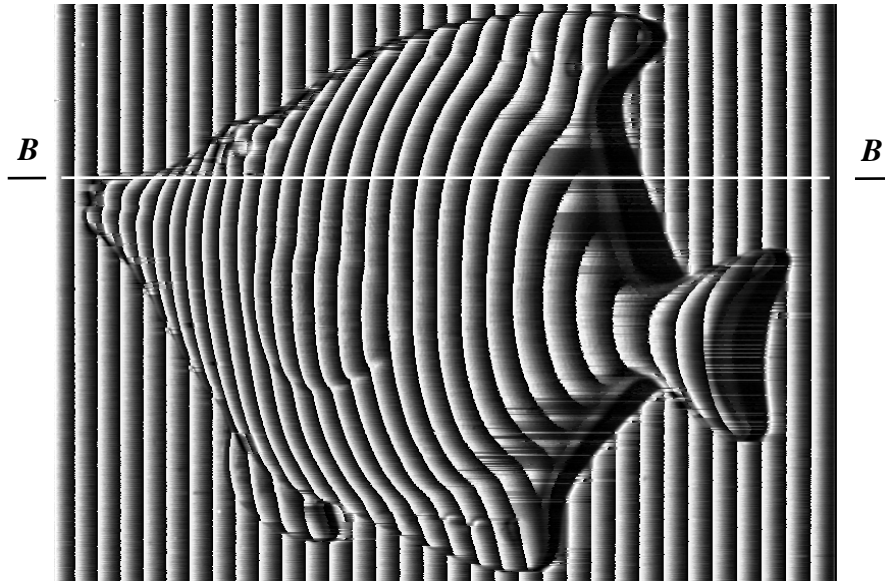


Fig. 5.19 Wrapped phase map extracted from a sawtooth fringe pattern

The triangular points are obtained by contact profilometer. As can be seen, the results do not agree well in the mouth and fin regions of the fish model, where the maximum error is over 60%. This can be explained by the fact that the projection shadow in these regions has distorted the recorded intensity and subsequently reduced the reliability and quality of the phase data. Figure 5.20(b) shows a comparison between the PMP and the contact profilometer for the same section. Since the phase-shifting algorithm is less dependent on intensity, it has successfully retrieved the profile at the mouth region (error < 5%). However, at the fin area as large shadow has completely removed the fringe signals, even the phase-shifting algorithm could not recover the actual profile (error > 60%).

It is also noted that at the main body of the fish model, the accuracy of PMP is higher (error < 5%); while the proposed method gave a profile containing erroneous ripples (error \approx 10%). Several factors such as system nonlinearity, non-uniform

reflectance, and random noise could affect the accuracy of the present method. The major source of error comes from system nonlinearity, which accounts for the shape distortion of a computer-generated sawtooth pattern. Reducing nonlinearity related errors should be the basis for future research.

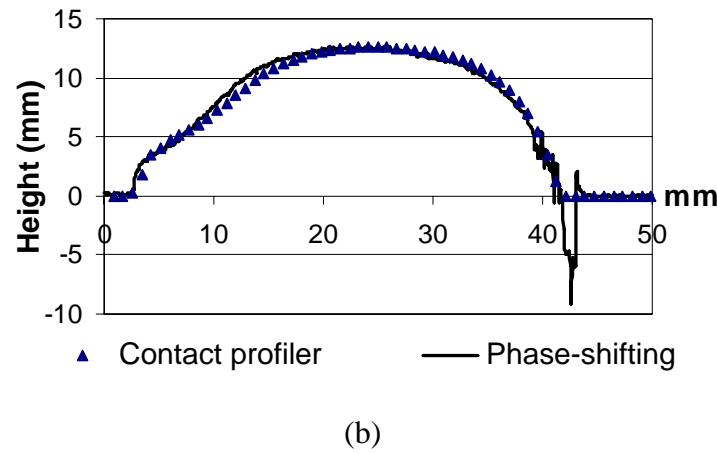
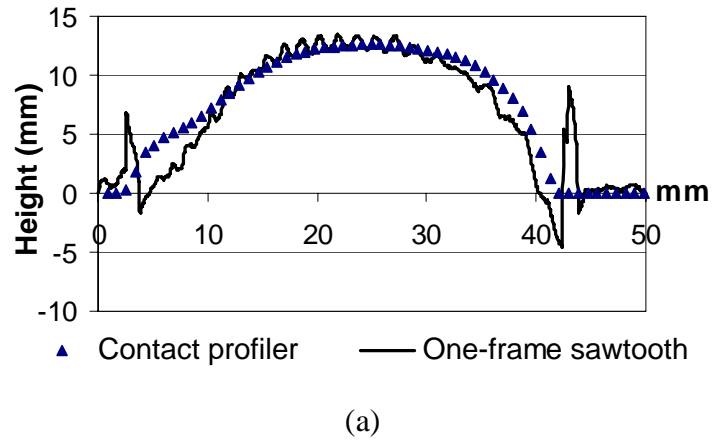


Fig. 5.20 Profile along section *B-B*, indicated in Fig. 5.19, obtained by
 (a) one-frame sawtooth profilometry method and contact profilometer;
 (b) PMP and contact profilometer;

Non-uniform reflectance is another source of error. Since intensity and phase value are coupled as shown in Eq. (3.18), any change in reflectance would introduce a phase change. Although the translation from intensity to phase is performed locally to enhance the tolerance to non-uniform reflectance, the method is more dependent on the

modulation intensity than the phase-shifting algorithm and therefore the latter produced better results at certain regions.

Random noise, such as exceptionally high or low intensity pixels, is not frequently encountered in this study. Nevertheless, if encountered, it would introduce errors in the identification of peak and valley intensities. With proper arrangement of the experimental setup and by using high quality projection and imaging devices, random noise can be minimized.

5.2 Phase quality identification

5.2.1 Spatial fringe contrast (SFC)

Specimen D (see section 4.3) is used to show the application of SFC in facilitating a phase unwrapping process. The processing window size parameter for the generation of SFC is discussed and the specimen profiles obtained by different phase quality criteria-guided unwrapping process are presented.

5.2.1.1 Selection of processing window size

Figure 5.21 shows specimen D with projected sinusoidal fringe pattern. As can be seen, the deformation of the fringe pattern reflects the structure of the specimen. The SFC is used to detect fringe pattern changes so as to identify drastic structure changes. Two examples are given in Fig 5.22, which shows 3-D plot of region ABCD and EFGH indicated in Fig. 5.21. Each region contains a phase shift in the x (Fig. 5.22(a)) or y (Fig. 5.22(b)) direction caused by a step change.

The effect of a y direction phase shift on SFC is illustrated in Fig. 5.23. Three curves (dotted) in Fig. 5.23(a) represent the intensity of three adjacent rows with a 30° phase shift in between. The solid curve is obtained by the least squares sine fitting. The

difference in the fringe modulation of the solid curve is less than 10 gray levels compared with that of the dotted curves. However, in Fig. 5.23(b), the SFC of the corresponding solid curve shows a decrease (30 gray levels) owing to a larger phase shift (60°). This comparison indicates that SFC would decrease with the increase in the y direction phase shift.

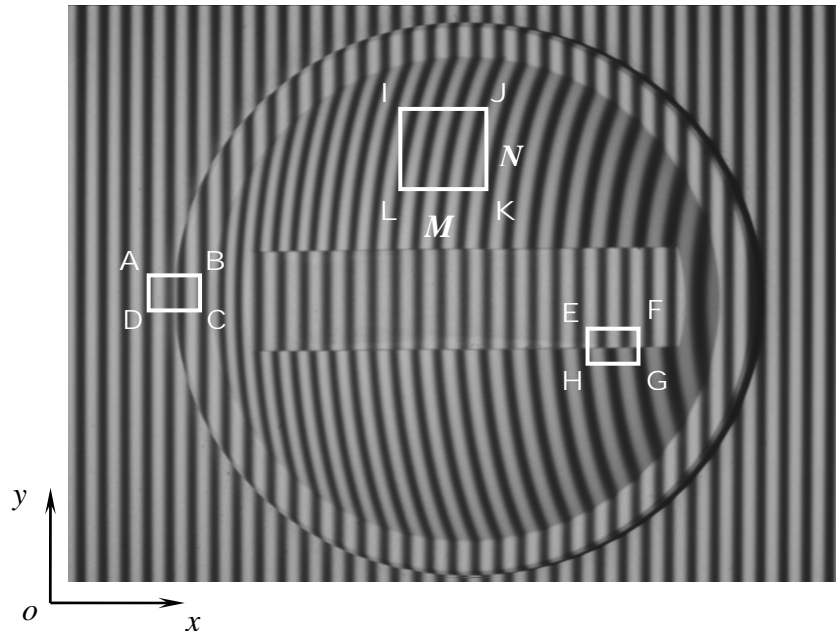


Fig. 5.21 Projected fringe pattern on specimen D

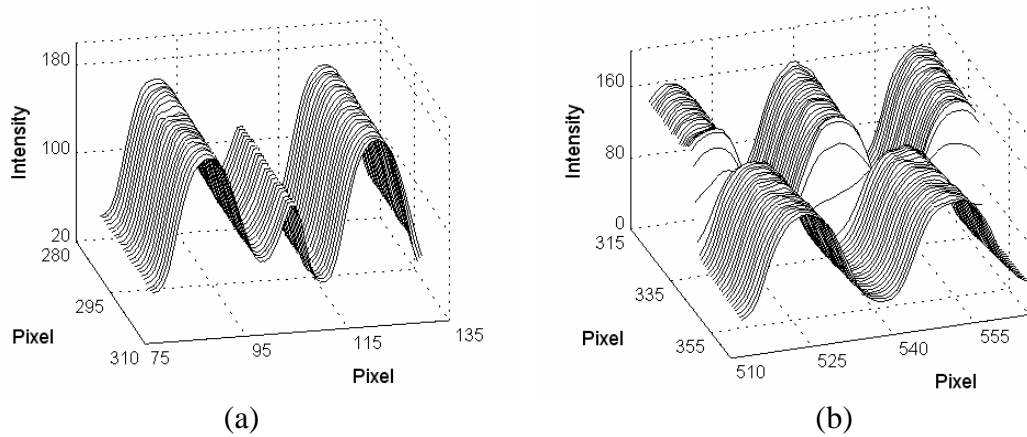


Fig. 5.22 3-D plot of region (a) ABCD x-direction pattern change, (b) EFGH y-direction pattern change, in Fig. 5.21

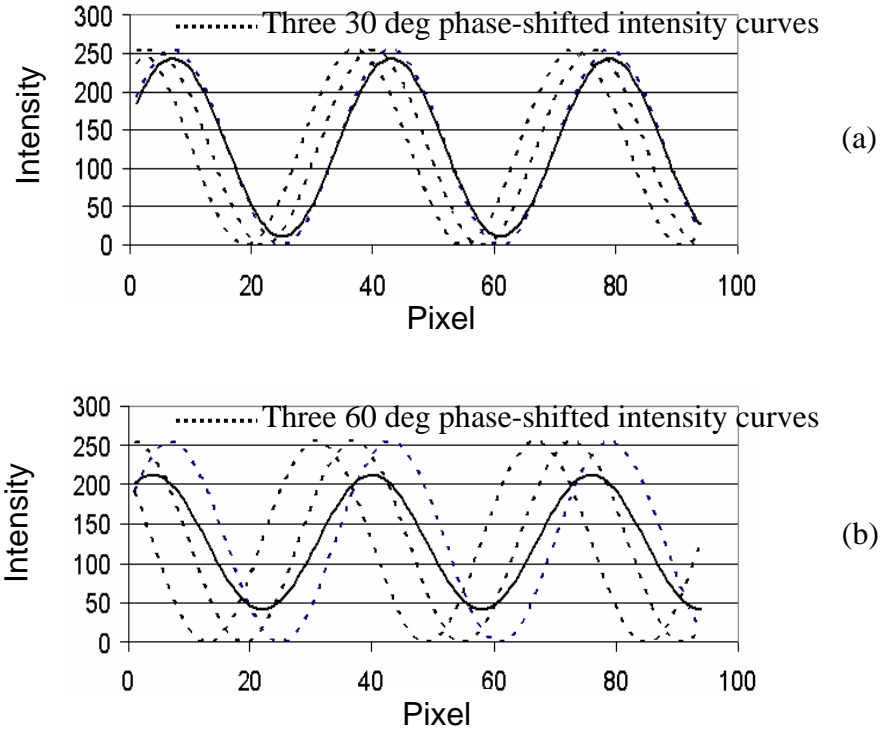


Fig. 5.23 The effect of (a) 30° , (b) 60° phase shift in y direction on SFC

The effect of x direction phase shift on SFC, however, is not as straight forward. Figure 5.24(a) shows a dotted sine curve with 60° phase shift introduced at $x = 10$ and the solid curve is sine-fitted. The SFC of the solid curve is about the same as the fringe contrast of the dotted curve. Therefore, it implies that SFC is not sensitive to the x direction phase shift. Li and Su (2002) proposed an effective fitting error-compensated quality criterion. The same idea is applicable to the current problem. It is seen in Fig. 5.24(b) that the maximal fitting error is exactly at $x = 10$, where the phase shift is introduced. Hence, integrating SFC with the fitting error, the phase quality identification can be more accurate.

Based on the above discussion, a guideline can be proposed for the selection of the processing window size ($M \times N$), where M and N specify respectively the width and height of the processing window. Since the SFC is sensitive to a y direction phase shift,

the height (N) of the window should be a small value. Otherwise, the accumulated phase shift in the y direction will be significant and a low SFC value will be subsequently produced even in a good quality area. Region IJKL in Fig. 5.21 can be used to exemplify the drawbacks of a large N . The fringe pattern in IJKL is of good quality. However, the phase shift from line IJ to LK is significant, which would result in an erroneously small SFC value.

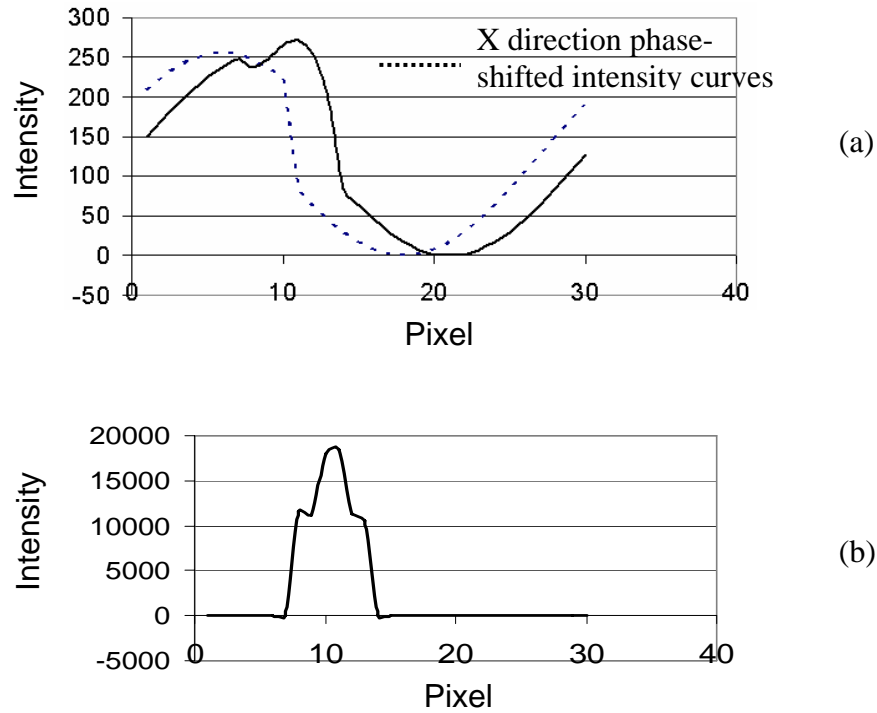


Fig. 5.24 (a) Effect of x direction phase shift on SFC; (b) fitting error

As the phase quality criterion essentially relies on a fitting error to detect an x direction phase shift, the width (M) of a window should be relatively large. The minimum value of M is three so as to solve the three unknowns in Eq. (3.22); whereas in this case the fitting error is zero. Only when more data points are used in the least squares fitting, does the fitting error represents the actual discrepancy more accurately. Hence, M should be a large value to ensure sufficient sampling in the x direction. In this study, a 9×3 processing window is used to calculate the SFC and fitting error.

5.2.1.2 Performance comparison of unwrapping algorithms

Figure 5.25 shows the wrapped phase map of specimen D. The top and bottom areas of the groove contain broken phase fringes, which is a challenge for a phase unwrapping algorithm. In this section, several unwrapping algorithms, namely the branch cut (Goldstein et al, 1988; Huntly and Buckland, 1995), temporal fringe contrast (TFC)-guided (Strobel, 1996), SFC-guided and SFC (with fitting error) guided algorithms, are used to retrieve the profile of the specimen.

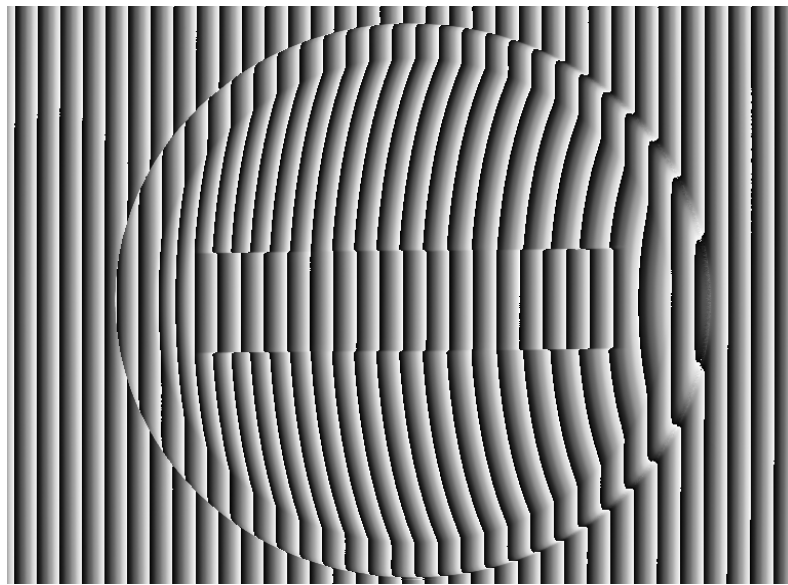


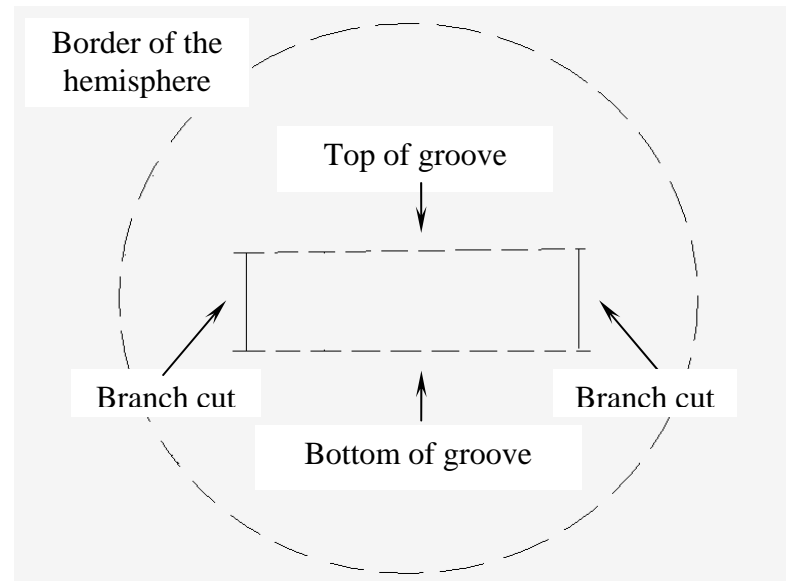
Fig. 5.25 Wrapped phase map of specimen D

Figure 5.26(a) shows several branch-cuts generated by the branch cut algorithm. Two branch-cuts are generated to balance four residues at the top and bottom of the groove. The branch-cuts are placed vertically instead of horizontally because shorter branch-cut is generated in the implementation of the algorithm. However, they prevented an unwrapping path from crossing the groove horizontally; and subsequently the path is forced to unwrap across the groove from the top and bottom. As phase data in these regions are discontinuous and unreliable, an erroneous surface profile is produced, as shown in Fig. 5.26(b). The results indicate that, although branch-cuts

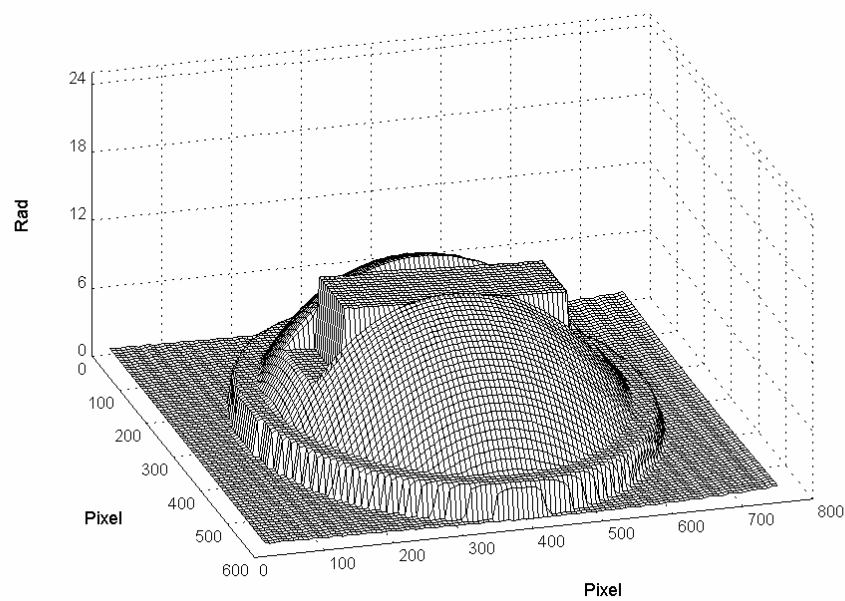
generated based on the shortest distance are statistically the best approach for the elimination of residues, they do not take into consideration of the phase quality and are unable to detect the structure of a test specimen.

Figure 5.27(a) is a TFC map derived from a four-frame phase-shifting algorithm (Strobel, 1996). The TFC map accurately identifies the phase quality in most parts of the specimen so that the reference plane is of high quality and the border of the hemisphere is of low quality. However, TFC is not able to detect the unreliable phase data at the top step of the groove (highlighted by arrow pointers). This is because TFC is most sensitive to projection shadow and it largely relies on a shadow area to sense an object surface structure. However, in this experiment, the illumination geometry is arranged such that there is little shadow cast on the top edge of the groove. Hence, TFC does not identify the drastic change in the surface profile. A misleading unwrapping path is chosen and erroneous results are generated, as shown in Fig. 5.27(b). It is seen that the errors in Fig. 5.26(b) and that in Fig. 5.27(b) are similar. The former is caused by the branch-cuts being misplaced and the latter is due to erroneous identification of phase quality.

Figure 5.28(a) shows an SFC map derived without the use of fitting error. The SFC clearly detects profile changes in the y direction at the top and bottom of the groove but encounters problems in detecting structure changes in the x direction, such as those at the border of the hemisphere. In these regions, the value of SFC fluctuates drastically and inaccurate identification of the phase quality resulted, indicated by arrow pointers. The deficiency of SFC in detecting the x direction phase shift shown is in agreement with the theoretical analysis. The unwrapped results given in Fig. 5.28(b) illustrate that errors occur at places where the phase quality is wrongly identified.

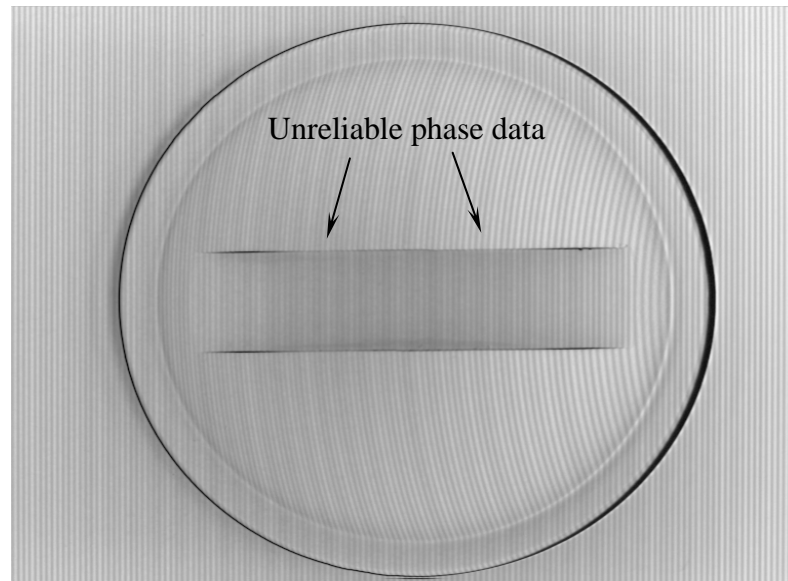


(a)

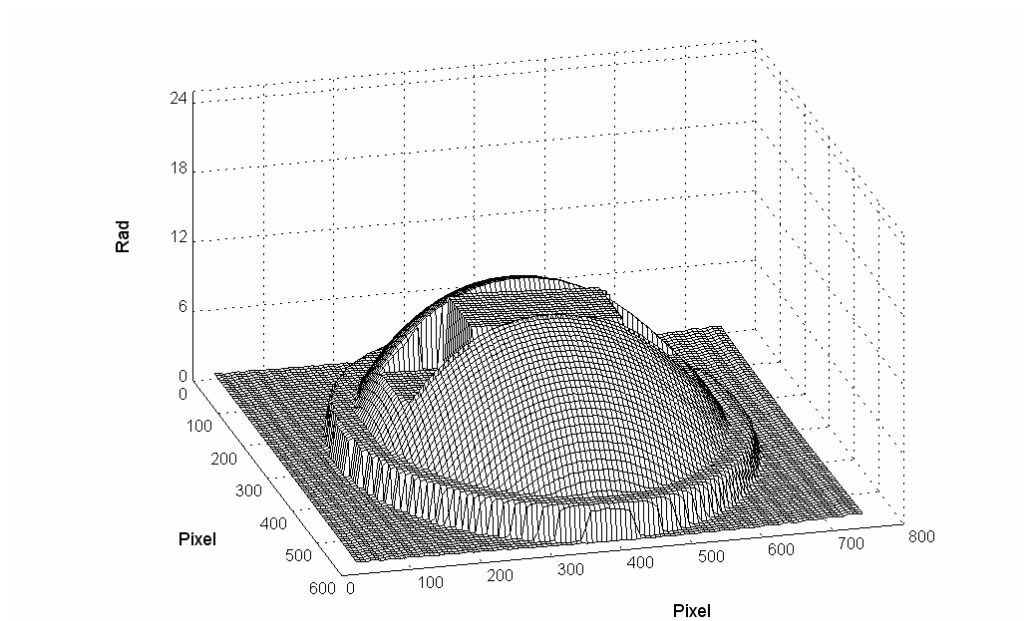


(b)

Fig. 5.26 (a) Branch-cuts generated by the branch cut algorithm;
(b) results of the branch cut unwrapping algorithm

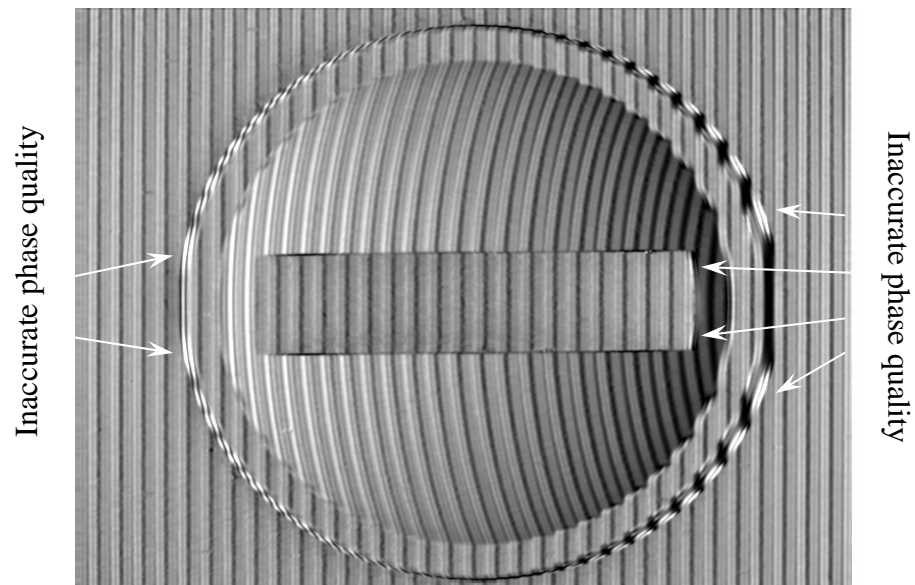


(a)

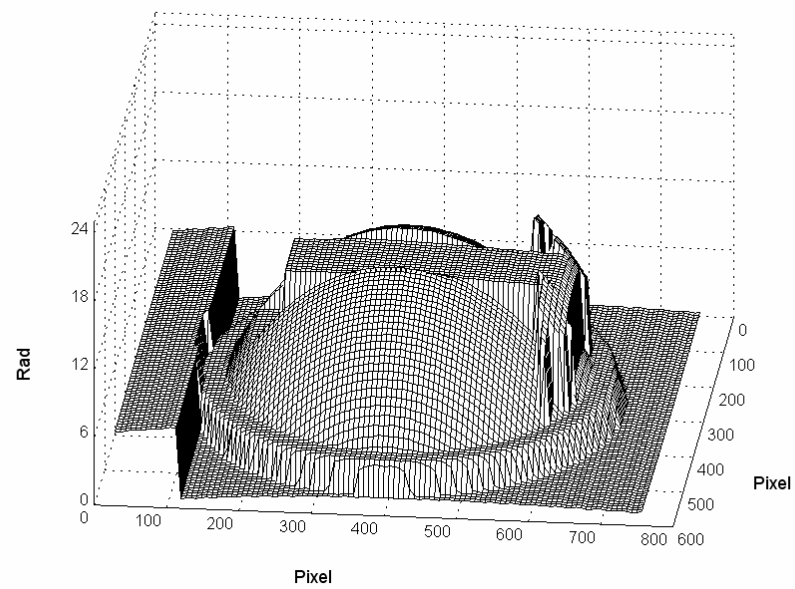


(b)

Fig. 5.27 (a) TFC map; (b) results by TFC-guided unwrapping

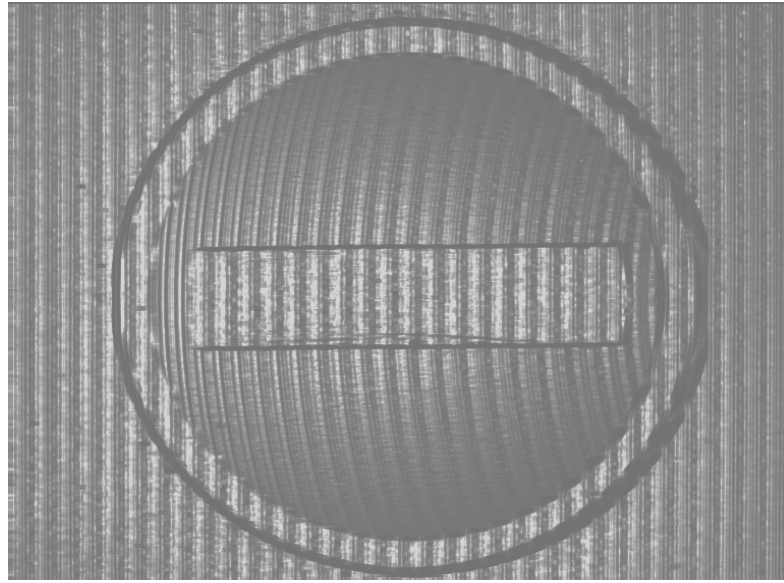


(a)

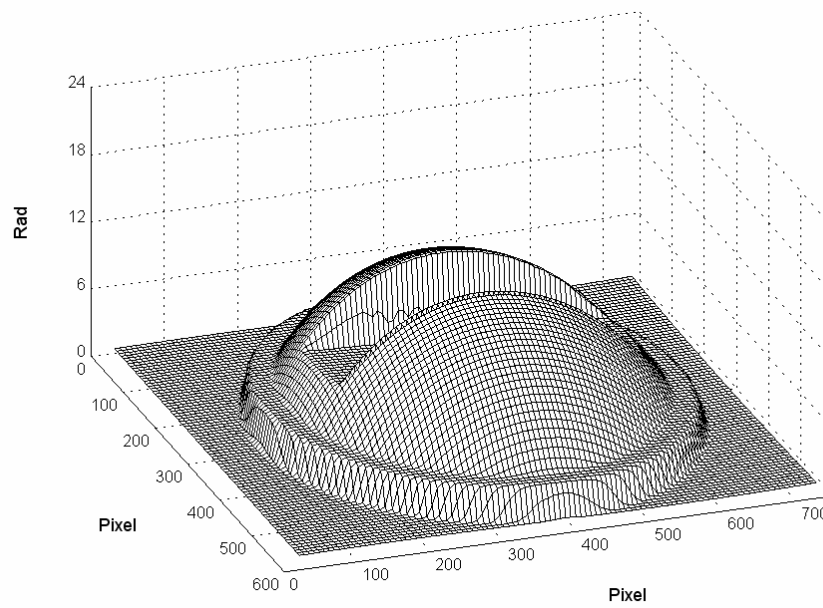


(b)

Fig. 5.28 (a) SFC map (without fitting error);
 (b) results by SFC-guided unwrapping (without fitting error)



(a)



(b)

Fig. 5.29 (a) SFC map (with fitting error);
(b) results by SFC-guided unwrapping (with fitting error)

Finally, Fig 5.29(a) shows a fitting error modified SFC map. As can be seen, both the x and y direction structure changes are detected. Compared with Fig. 5.28(a), the SFC values at the border of the specimen decrease substantially. Figure 5.29(b) shows the surface profile obtained. It is seen that the profile is correctly retrieved without the errors that are present in the above mentioned methods. The major advantage of SFC over TFC is that it is not only sensitive to the fringe contrast parameter but also is able to deduce the structural information from fringe pattern changes.

5.2.2 Comparison of conventional and plane-fitting quality criteria

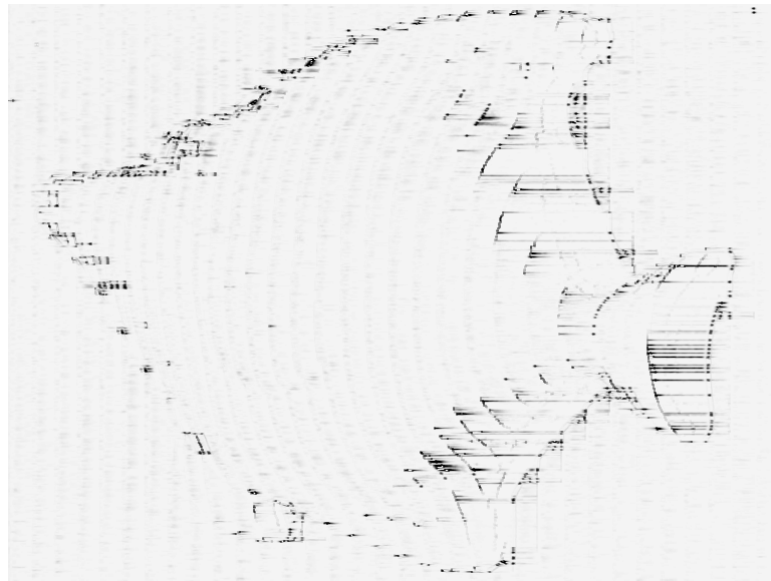
Phase quality criteria including phase derivative variance (Pritt, 1996), pseudo-correlation (Roth, 1995), and the proposed plane-fitting are applied on the wrapped phase map (Fig. 5.19) of specimen C. The specimen's edge, fin, and tail regions receive low illumination intensity, as shown in Fig. 4.8 (see section 4.3), and hence they are of bad quality. Phase data in these regions should be unwrapped at a later stage so that unwrapping errors can be confined to a minimum. Otherwise, if the shadow areas are erroneously labeled as having high quality and unwrapped at an early stage, errors would begin to accumulate and affect all subsequent results.

Normally, a phase derivative variance map is sensitive to noise. The larger the noise, the larger is the variance and hence low quality. However, the variance map shown in Fig. 5.30(a) is not able to identify the low quality data at the fin and tail of the specimen. This is due to the small variance of shadowed phases. Furthermore, although the variance map detects some unreliable data at the specimen edge, the low quality regions are disconnected, making it possible for an unwrapping path to move in and out of the fish model from the gaps. This drawback would inevitably bring in

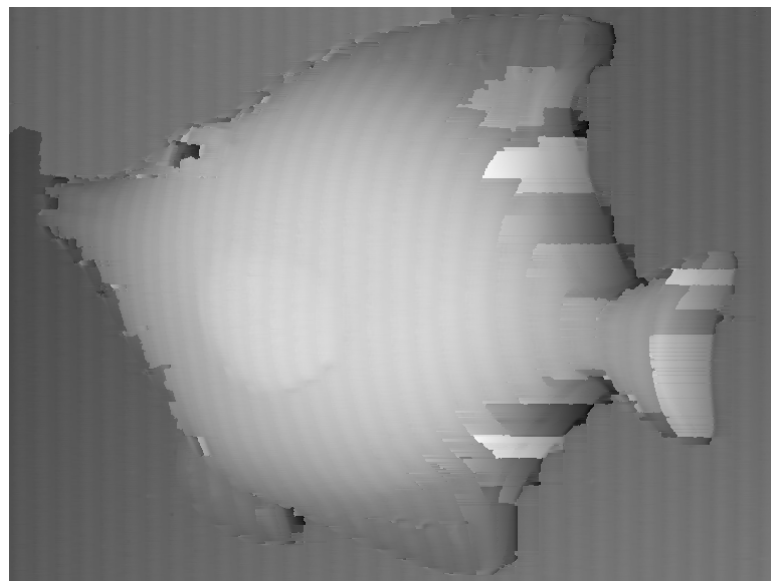
errors. The unwrapped results (after carrier removal) guided by a variance map is shown in Fig. 5.30(b). There is a large discontinuous area at the top left corner on the reference plane. Intuitively, the error must have originated from the edge of the fish model and spread into the reference plane. It is worth noting that the variance map would have better performance if a phase-shifting algorithm is used to extract the wrapped phase data, since shadow areas would become noise data after being processed by a phase-shifting algorithm.

The second quality criterion tested is the pseudo-correlation map (Roth, 1995). The quality of a pixel is related to a correlation coefficient that describes the degree of self-similarity of a region. A noise corrupted region is poorly self-similar, hence low quality; and vice versa. Theoretically, the pseudo-correlation is not sensitive to shadowed phases with good self-similarity but, as shown in Fig. 5.31(a), the pseudo-correlation map accurately identifies the border of the shadow on the fin and tail of the fish model. This is owing to the drastic change in pattern between the shadow and the reference plane. As a result, the unwrapped phase data in Fig. 5.31(b) at the fin and tail regions show improvement compared to those in Fig. 5.30(b). However, the quality of the specimen edge was still not accurate, rendering errors to penetrate into the reference plane and the specimen.

The proposed plane-fitting quality criterion evaluates the quality of a fitted plane in the neighborhood of a pixel under consideration. The quality is related to the normal vector of the plane and the fitting error. Figure 5.32(a) shows a plane-fitting quality map. The phase data on the edge, fin and tail of the specimen are correctly labeled as low quality. The quality criterion also produces periodically changing quality stripes on the reference plane and the fish model body, where uniform quality distribution is supposed to be present.

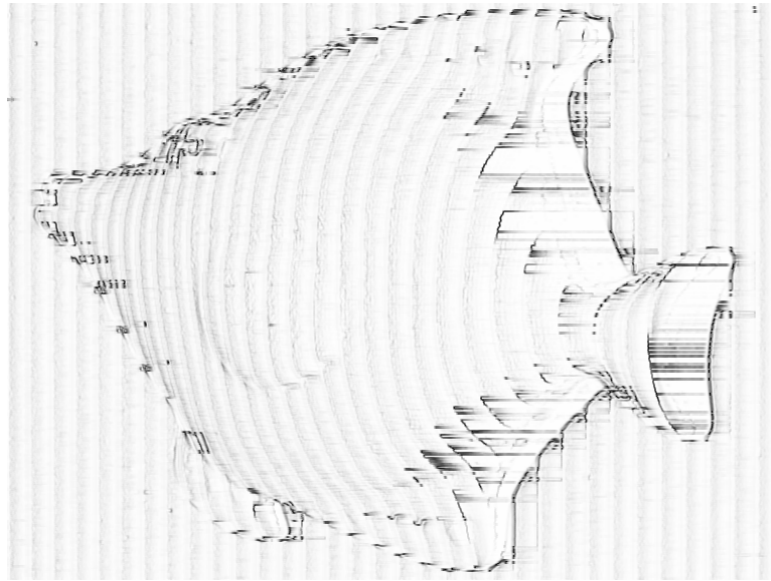


(a)

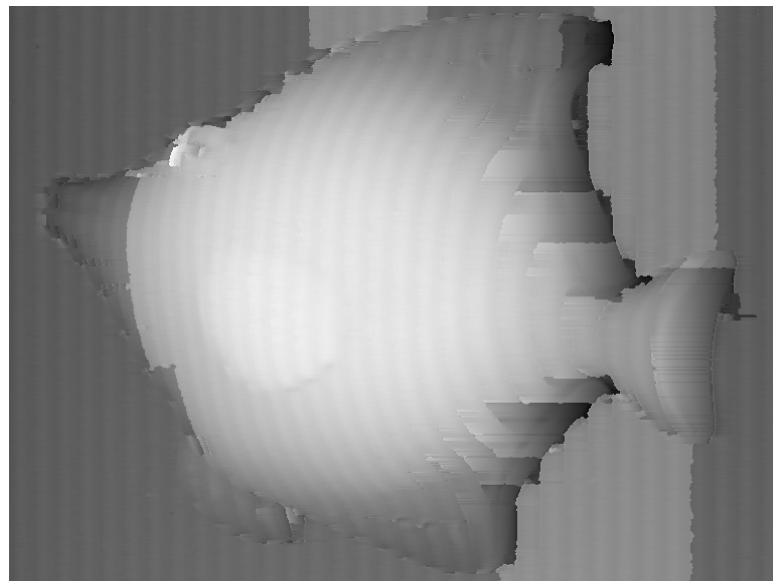


(b)

Fig. 5.30 (a) Phase derivative variance map;
(b) unwrapped results guided by variance map.

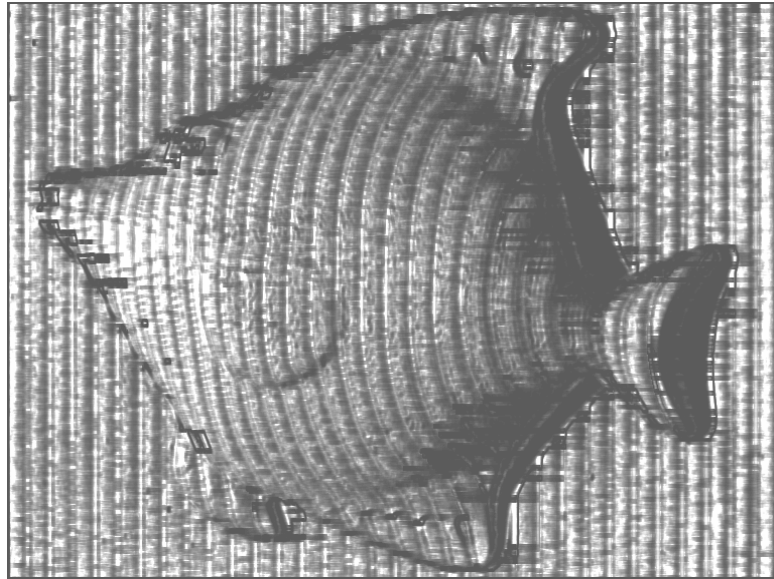


(a)

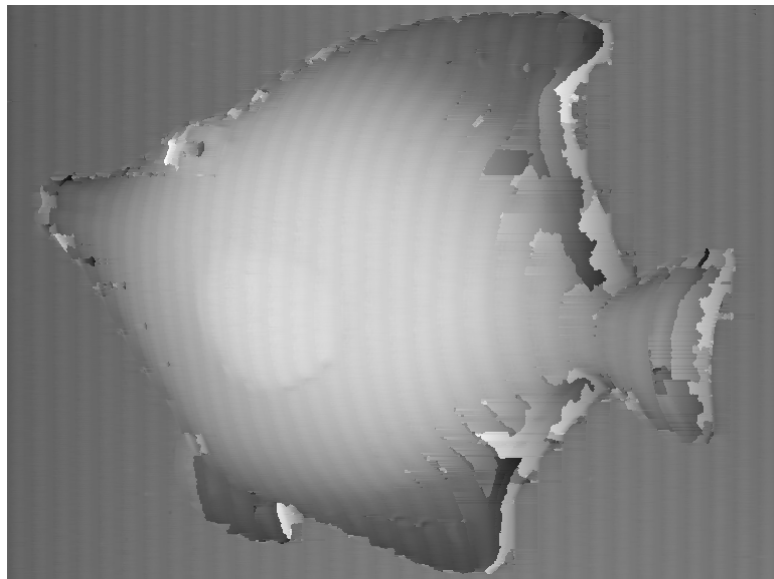


(b)

Fig. 5.31 (a) Pseudo-correlation quality map;
(b) Unwrapped results guided by pseudo-correlation map.



(a)



(b)

Fig. 5.32 (a) Plane-fitting quality map;
(b) Unwrapped results guided by plane-fitting map.

These stripes are caused by the system nonlinearity. Although the data plane of a computer-generated sawtooth pattern has an identical normal vector, the plane is curved when the sawtooth pattern is projected. The curvature of each period is similar resulting in a periodically changing slope of the fitted plane. Therefore, a periodically changing quality stripes are formed. However, since the quality stripes achieve higher quality than those of the shadow, they would be unwrapped earlier. Consequently, the unwrapping errors are confined to shadow areas, as shown in Fig. 5.32(b). In general, the plane-fitting scheme is analogous to the SFC criterion. Both are based on a fitting approach and hence they share the advantage in detecting object structure information.

5.2.3 Fringe density estimation

5.2.3.1 1-D fringe density estimation

A 1-D signal shown in Fig. 5.33(a) is processed by the proposed density estimation algorithm. Figure 5.33(b) shows the fringe density distribution obtained by setting a scale increment step to 1 unit. It is seen that, instead of a continuous distribution, the estimated fringe density curve contains undesirable steps. The reason is revealed as follows: In an ideal CWT process, the scale and shift parameters should change continuously; however, this is impossible in practical computation, where discrete steps must be used to balance between computation time and resolution. Hence, a theoretical fringe density value would be approximated to the nearest retrievable density level, which results in undesirable steps. If the increment step is reduced to 0.2 units, a density curve with smaller steps would be produced, as shown in Fig. 5.33(c). Nevertheless, this is not an optimal solution, since the computation time is increased by five times. An alternative approach is to process the density curve with a mean filter and Fig. 5.33(d) shows the results obtained (increment step of 1 unit).

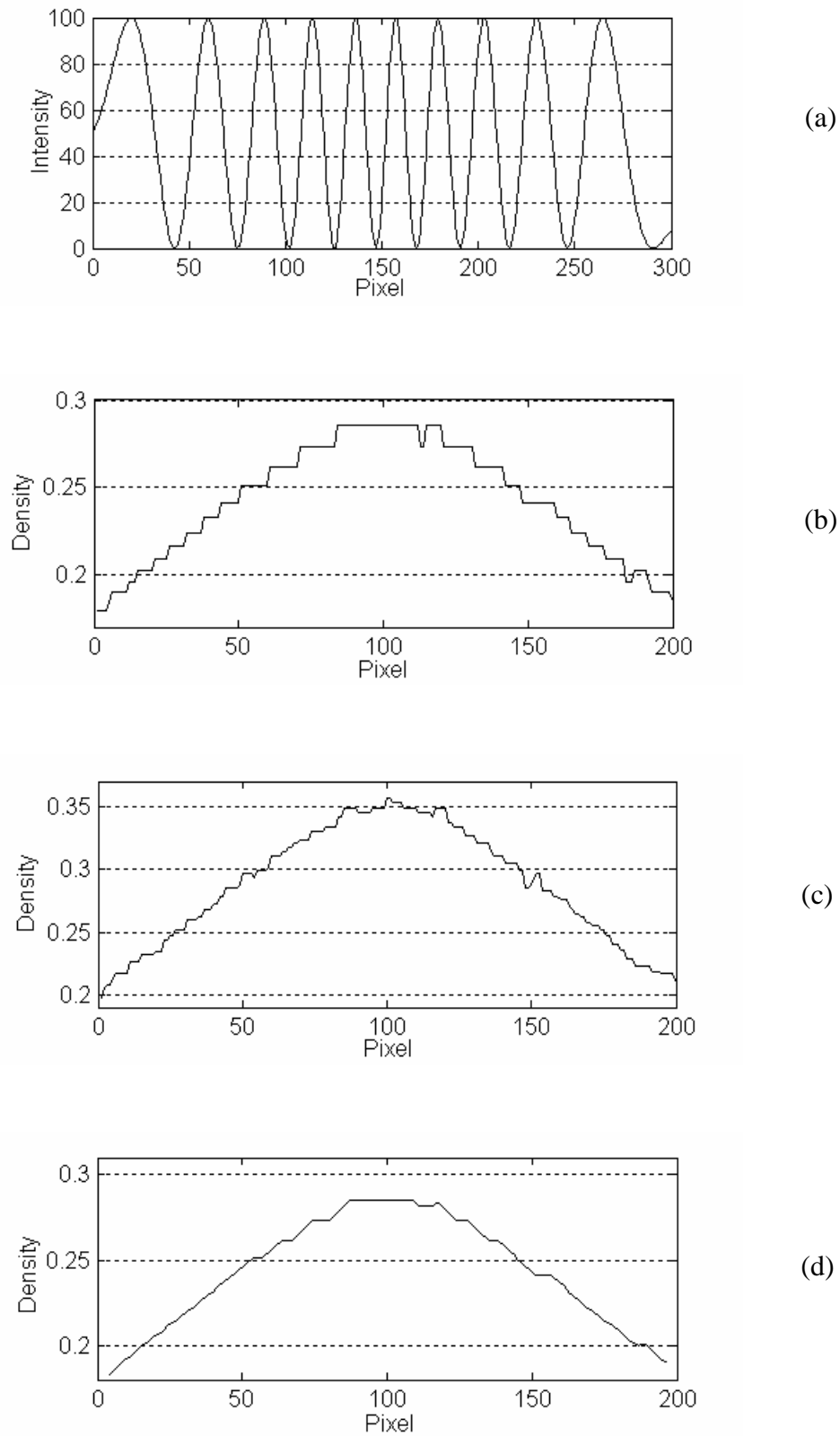


Fig. 5.33 (a) Sinusoidal signal with high frequency at the center;
 Density curve obtained by setting the scale increment step
 (b) with 1.0; (c) with 0.2; (d) with 1.0 and a mean filter

The smoothness of the curve is better than that shown in Fig. 5.33(c); while the additional computation time is almost negligible.

The fringe density estimation for 1-D signal with additive noise is also studied. Figure 5.34(a) shows a corresponding signal in Fig. 5.33(a) with a 50% additive noise. Since noise-related CWT magnitudes are smaller than those of the signal-related, the CWT ridge still represents the instantaneous frequency of the signal; and hence density estimation remains accurate. A density curve obtained by setting a scale increment step to 1 unit without using a mean filter is shown in Fig. 5.34(b). Compared with Fig. 5.33(b), it is seen that the undesirable steps are replaced by rapidly changing density values. This is due to a noise-related random shift in the ridge points which makes the density curve oscillate near a theoretical value, but the overall fringe density distribution is maintained. To eliminate the noise effect, a computationally expensive method, in which the scale increment step is set to 0.2 units, is used. Although such approach reduces the undesirable steps (Fig. 5.33(c)), it is found not effective for noise reduction. The resultant density curve in Fig. 5.34(c) does not show much improvement, indicating that increasing the resolution of the scale could not eliminate the random shift in the ridge points. Another approach is to process the noisy density curve in a mean filter. With negligible additional computation time, the method produces significantly improved results (Fig. 5.34(d)). It is implied that regardless of the noise level, pre-processing of a signal is not required. For a clean signal the mean filter removes undesirable steps; while for a noisy signal the procedure is able to reduce the noise.

In cases where multiplicative noise is present, the original density information would be completely changed and therefore preprocessing to recover the density information is necessary.

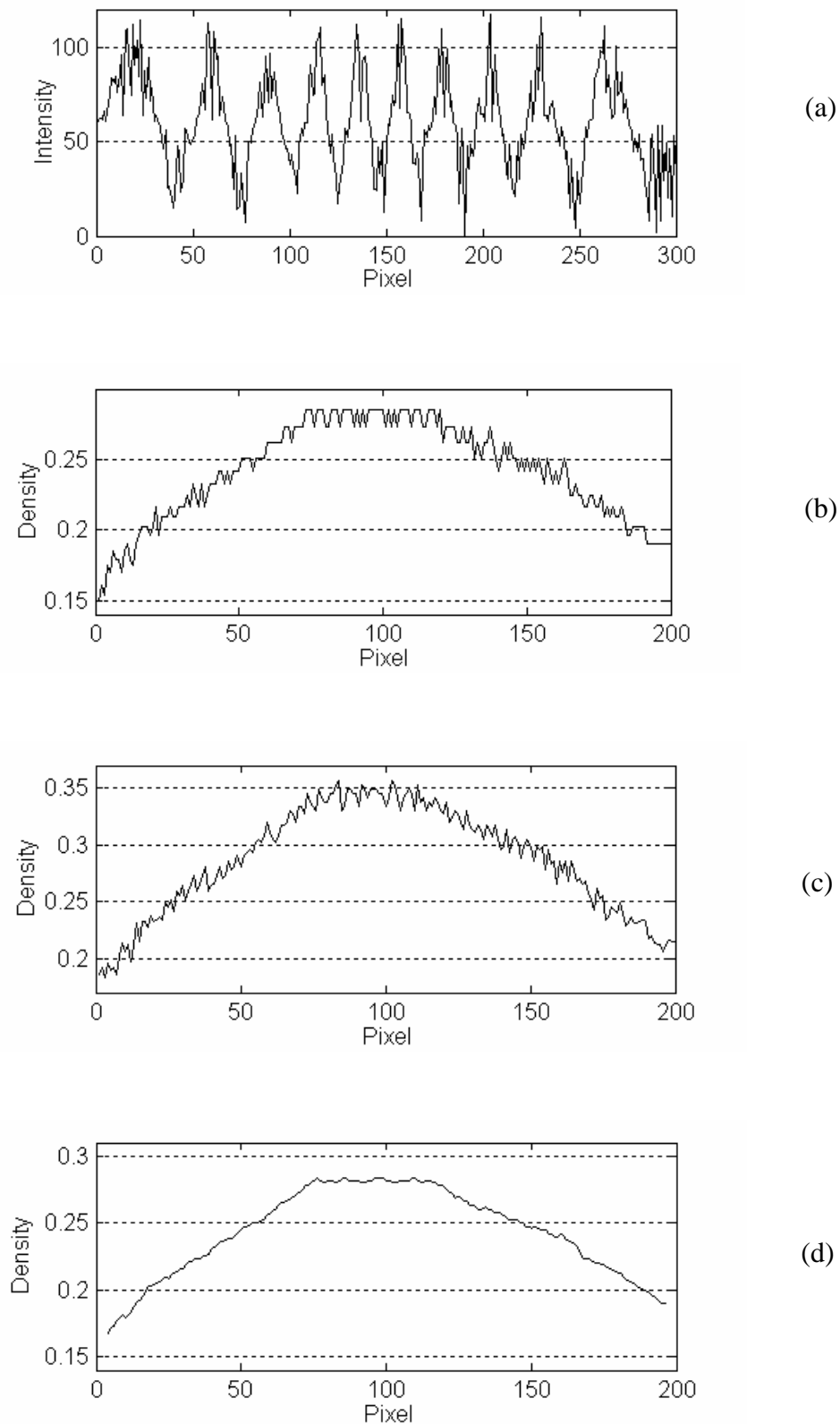


Fig. 5.34 (a) Sinusoidal signal with additive noise;
Density curve obtained by setting the scale increment step
(b) with 1.0; (c) with 0.2; (d) with 1.0 and a mean filter

5.2.3.2 2-D fringe density estimation

For a 2-D fringe pattern with additive noise, shown in Fig. 5.35 (400×300 pixels), the fringe density components in both the x and y directions should be calculated to estimate the overall density distribution.

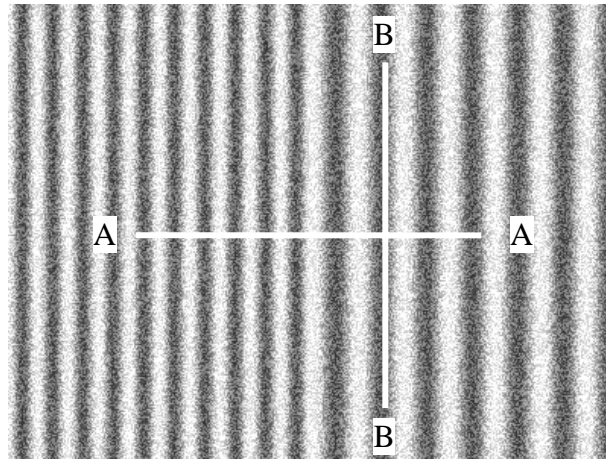


Fig. 5.35 Vertical fringe pattern

In this process, the CWT magnitude used as a weight is of significant importance. The CWT magnitude is proportional to the fringe modulation, a parameter widely used to describe the quality of a fringe pattern. A remarkable feature gained by using the weight is the noise reduction capability, which is different from the inherent noise reduction feature of the global maximum ridge detection method mentioned in 1-D signal processing. Furthermore, for a 1-D signal the problem of fringe direction determination does not arise. However, for a 2-D signal the fringe density should be measured in the fringe direction. (For instance, the fringe direction is in A-A, as indicated in Fig. 5.35.) In the proposed method, although the fringe direction is not explicitly measured, it is related to the CWT magnitude. If the fringe direction is closer to the direction of the x axis, higher fringe modulation would be measured in the x

direction and the overall density value would be more dependent on the density component in the x direction, and vice versa.

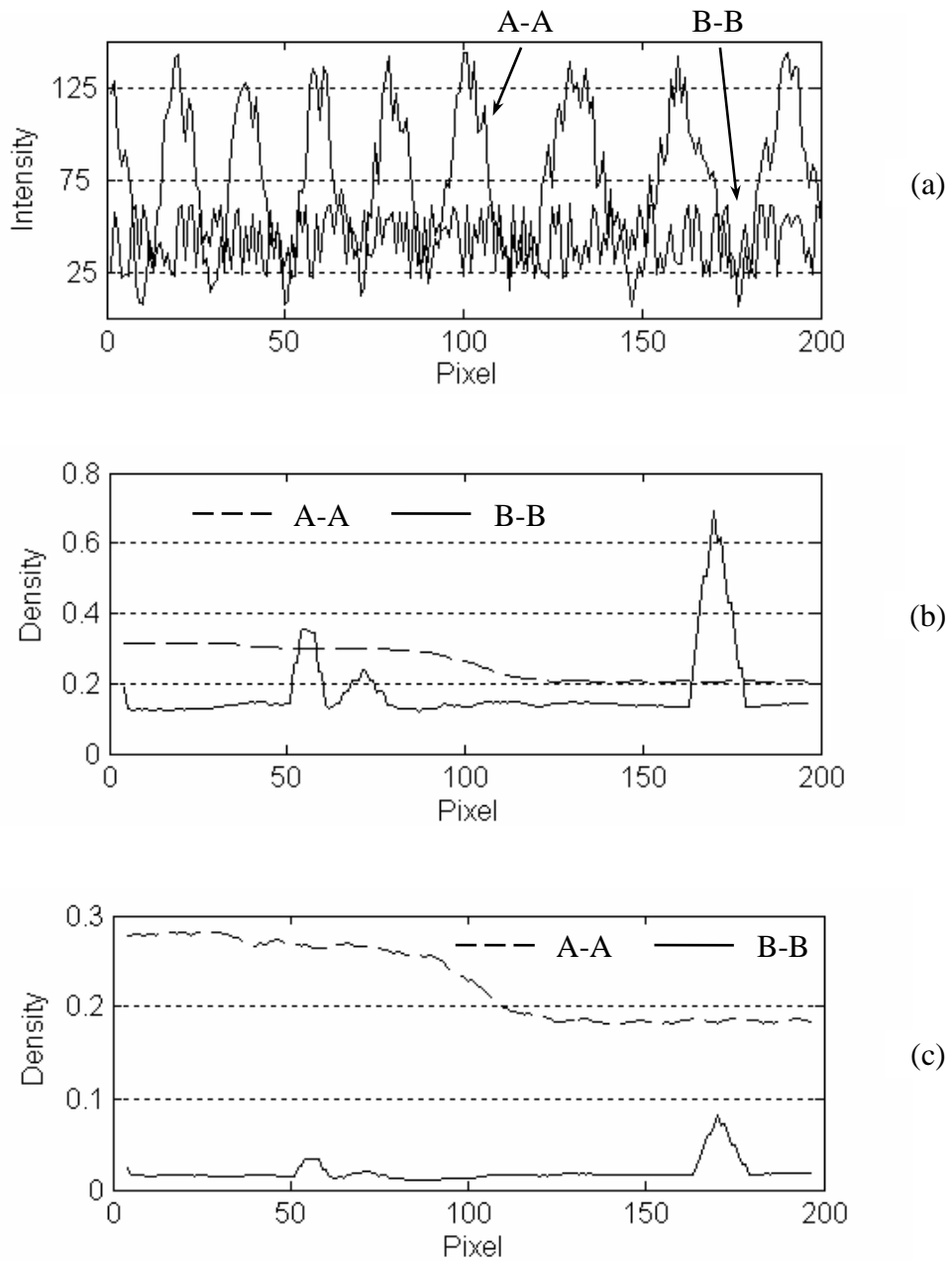


Fig. 5.36 (a) Intensity along sections A-A and B-B;
Density curve along A-A and B-B (b) without noise reduction weight;
(c) with weight

Figure 5.36(a) shows intensity of sections A-A and B-B, as indicated in Fig. 5.35. It can be seen that A-A consists of the sinusoidal fringe signal with added noise;

while B-B contains noise only. The noise reduction functionality of the weight is presented by using Figs. 5.36 (b) and (c). Figure 5.36(b) shows the detected density curve along section A-A (dashed line) and B-B (solid line) without the noise reduction weight. Along section B-B, the actual signal intensity is constant but corrupted by noise. Hence, the detected instantaneous frequency does not show correlation to the actual signal and drastically changing density values are produced. In section A-A, the actual signal is dominant and a correct density curve, which shows high density on the left section and low density on the right, is obtained. However, if the two density curves are added, the density information of section A-A would be corrupted by that of section B-B. Figure 5.36(c) shows the corresponding density curves obtained with the noise reduction weight. Since section A-A has a higher fringe modulation, its weighted density values remain about the same; whereas those of section B-B are reduced. This indicates that the noise related density only accounts for a small influence on the results.

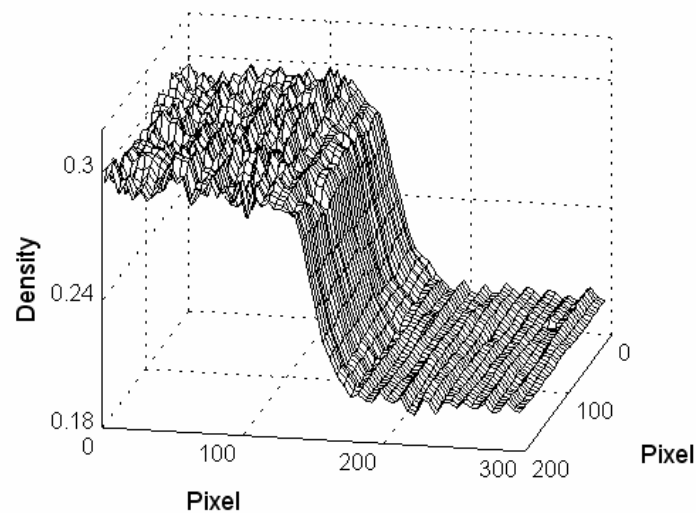


Fig. 5.37 Fringe density map of the vertical fringe pattern

Consequently, despite the noise, a correct density distribution shown in Fig. 5.37 is obtained by combining the weighted density components in both the x and y directions, (To avoid edge distortion, 50 pixels at the boundary are excluded.)

5.2.3.3 Accuracy analysis

Figure 5.38 shows a circular fringe pattern with a parabola density distribution. The fringe density map in Fig. 5.39 shows that the distribution is not smooth and contains many local minima. Although the proposed 2-D fringe density estimation algorithm is insensitive to noise, its accuracy is limited by several factors.

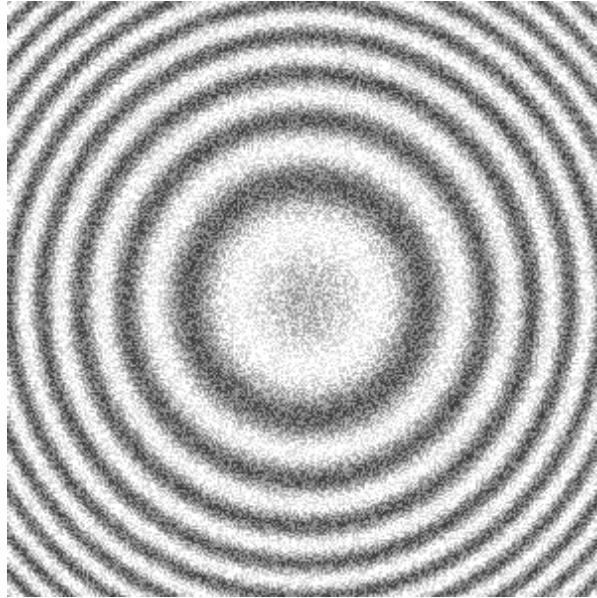


Fig. 5.38 Circular fringe pattern with a parabola density distribution

Firstly, the fringe density is not measured in the fringe direction; instead an approximate density is calculated from the x and y direction density components. This scheme would introduce maximum system error when the fringe direction is at 45° or 135° . In these cases, the theoretical density components in both the x and y directions are $1/\sqrt{2}$ of the actual density; however, the CWT weight brings another factor of

$1/\sqrt{2}$ into the density components. Subsequently, the calculated density would be lower than the actual value, as shown by the local minima along the 45° and 135° lines in Fig. 5.39. If the fringe direction is closer to the direction of x or y axis, the system error would be smaller. Secondly, errors might occur in local areas where a dominant frequency of the fringe pattern undergoes considerable changes. This is analogous to analyzing a signal with multiple dominant frequencies. Ambiguity might occur in identification of the local fringe density. Thirdly, if a scale parameter is not accurately measured, errors would be accumulated in the CWT weight and the overall accuracy would be reduced.

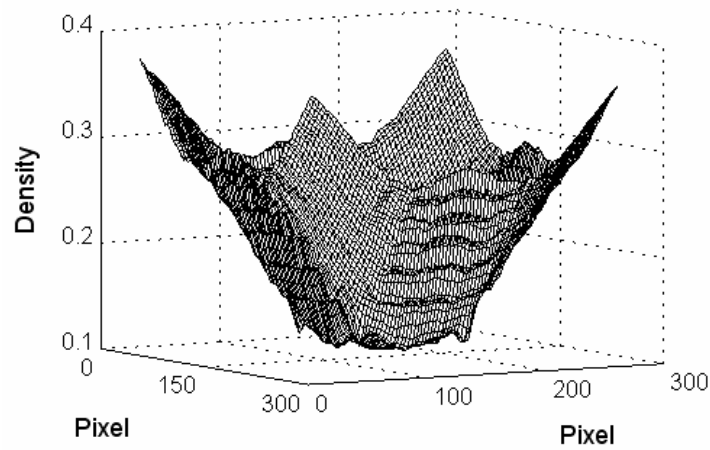


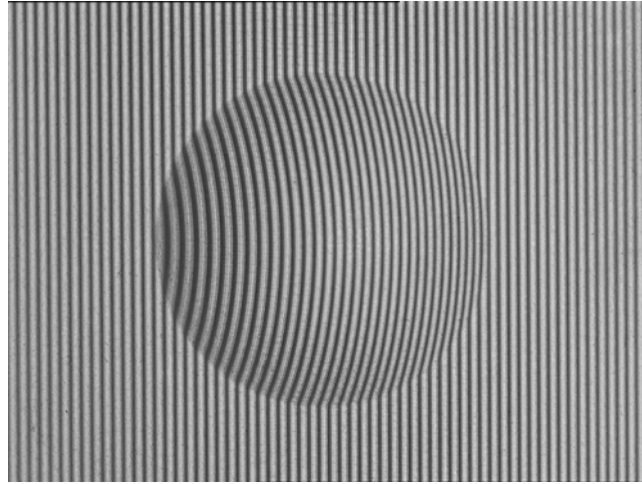
Fig. 5.39 Density map of a circular fringe pattern

5.3 Carrier phase component removal

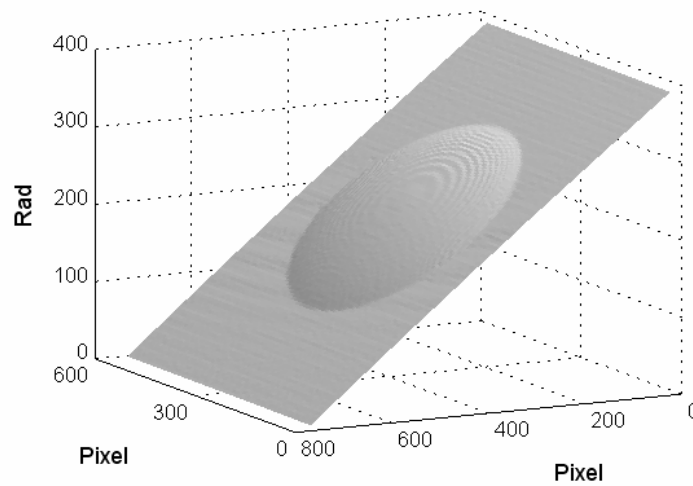
The carrier phase removal technique addresses the issue of post-processing an unwrapped phase map. It aims to retrieve a linear relationship between a phase value and the height of an object point.

5.3.1 Carrier fringes in the x direction

Figure 5.40(a) shows a fringe pattern projected on specimen E (see section 4.3). The carrier fringes are generated in the x direction in accordance with the curved line-fitting theory (section 3.3.1).



(a)



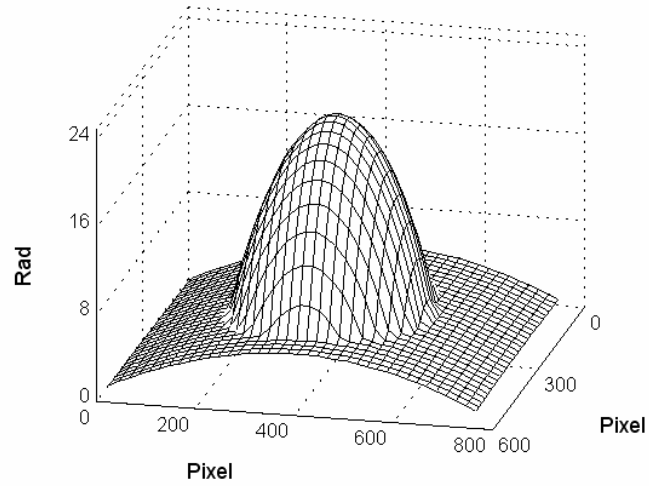
(b)

Fig. 5.40 (a) Specimen E with projected carrier fringes in the x direction;
(b) unwrapped phase map.

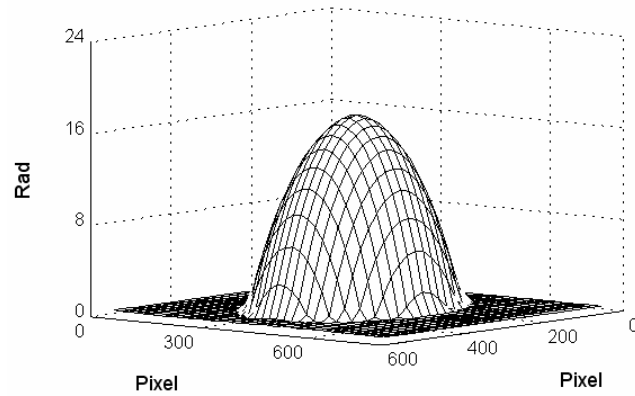
A wrapped phase map is extracted by a phase-shifting algorithm (Morgan, 1982; Greivenkamp, 1984) and an unwrapping process is incorporated to retrieve a

continuous phase distribution. Figure 5.40(b) shows a 3-D plot of an unwrapped phase map. As can be seen, the phase distribution consists of both carrier fringe-related and shape-related phase components.

If one only removes a linear phase component by setting N to 1 in Eq. (3.49), a curve in the reference plane would be produced, as shown in Fig. 5.41(a).



(a)



(b)

Fig. 5.41 Phase distribution after removal of (a) a linear carrier;
(b) a carrier by 2nd-order curve-fitting.

This shows that a 1st-order curve-fitting is not sufficiently accurate in approximating the actual carrier function and a higher value of N is required to produce a better

approximation to the nonlinear carrier. Figure 5.41(b) shows a significantly improved result when N is set to 2. However, up to a certain value of N , the carrier-estimation accuracy would not be improved any further, since subsequent improvement would be smaller than phase measurement uncertainty. Figure 5.42 shows that results of 2nd-order ($N = 2$) curve-fitting differ from those of contact profiler by less than 1%; while results of the linear carrier removal method shows more than 15% deviation. It is important to note that data points used for the estimation of the carrier function should be in the vicinity of the reference plane. Hence, this would require a certain degree of human intervention to distinguish the reference plane from the test object. With advanced graphics-based human-computer interface, a user-friendly program could make the region-selection easily. Furthermore, for objects that have an inherent base plane, manual identification of the reference plane is unnecessary. An example of this case is shown later.

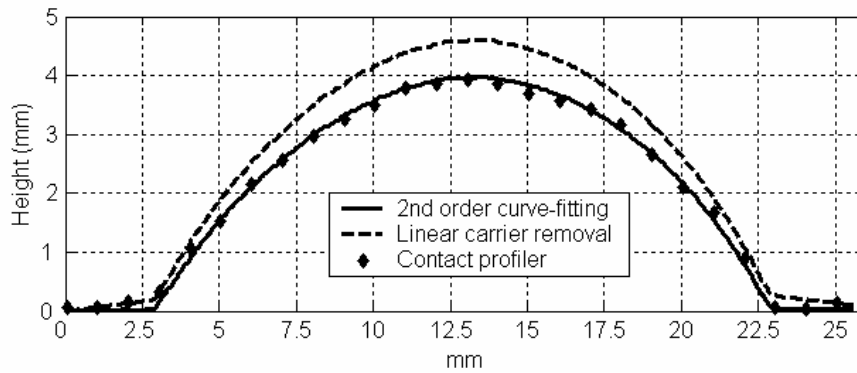
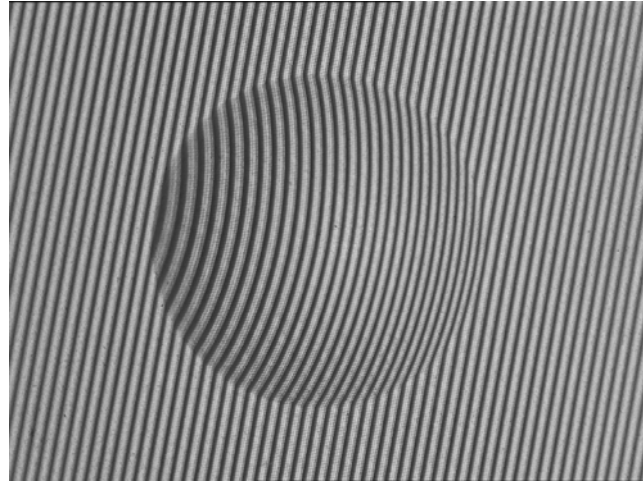


Fig. 5.42 Comparison of results obtained by 2nd order curve-fitting, linear carrier removal, and contact profiler

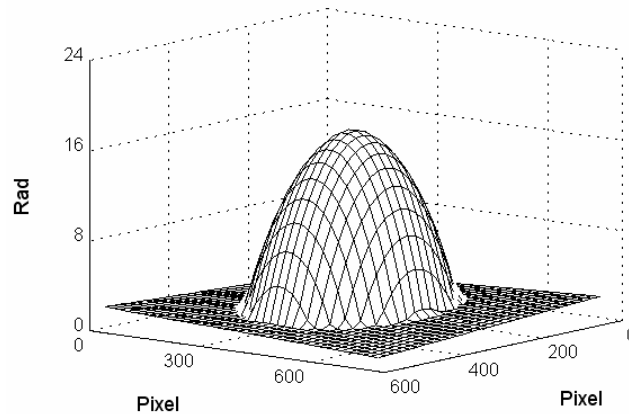
5.3.2 Carrier fringes in an arbitrary direction

Figure 5.43(a) shows specimen E with carrier fringes generated in an arbitrary direction. In this case, the spatial nonlinearity of the carrier is extended to the y direction. To remove the arbitrary-direction carrier, a combination of the individual

line-fitting in the x and y directions is first tested. It is seen from the results in Fig. 5.43(b) that, although the main part of the curve is removed from the reference plane, it still contains a residual curvature.



(a)



(b)

Fig. 5.43 (a) Specimen E with carrier fringes in an arbitrary direction;
(b) phase distribution after the removal of a carrier obtained by independent line-fitting in the x and y directions.

This is because the combination of the line-fitting in the x and y directions could only provide estimate on the orthogonal components of the nonlinear carrier, which would leave some carrier phases unaffected. To overcome the problem, the carrier is estimated by a generalized surface-fitting approach, as described in section 3.5.2. In

this method, a 2nd-order series expansion is used and the results obtained are similar to those shown in Fig. 5.41(b).

Comparing with Takeda and Mutoh's reference phase map-subtraction method (1983), which is also applicable to the current problem, the proposed least squares approach has two advantages. Firstly, only one measurement is needed. Secondly, the nonlinear carrier is obtained by a series expansion that does not introduce random errors, which are present in Takeda's method. Hence, the subtraction of the carrier function would not magnify the overall phase measurement uncertainty. The proposed method also shares the same advantage as Li et al's average-slope method (1998). Both techniques do not rely on the subtraction of the actual measurement phase values to remove the carrier; instead a carrier function is generalized from the experimentally obtained phases to eliminate measurement uncertainty. However, since Li's average-slope method only handles a linear carrier, the proposed higher-order curve-fitting approach is considered to be more flexible.

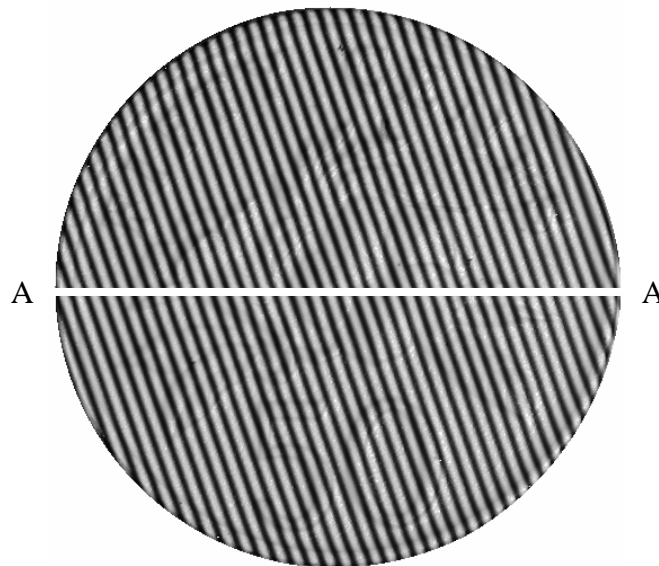


Fig. 5.44 Specimen F with carrier fringes in an arbitrary direction

In the experiment on specimen E, since the specimen does not have an inherent base plane, a reference plate serves as the source of the phase data for the curve-fitting. This limitation could be avoided for other kinds of object having a self-reference, such as specimen F (see section 4.3) shown in Fig. 5.44. The fringe pattern outside of the coin region has been masked. Phase data, including the wording, icon and the base plane on the specimen, are processed by the surface-fitting algorithm.

If one only removes a linear carrier or applies the independent line-fitting in the x and y directions, results similar to those shown in Fig. 5.45(a) would be obtained. It can be seen that residual curvature actually distorts the shape of the specimen. The results also imply that the nonlinearity of the carrier could not be easily eliminated by manual adjustment of the experimental setup because, as seen from the fringe pattern in Fig. 5.44, it is almost impossible for the naked eye to differentiate if the fringe spacing is a constant or not. Figure 5.45(b) shows the profile of specimen F obtained by the generalized surface-fitting carrier-removal process. The base plane of the coin is retrieved (error less than 3%) and hence subsequent evaluation of the specimen height would have sufficient reliability.

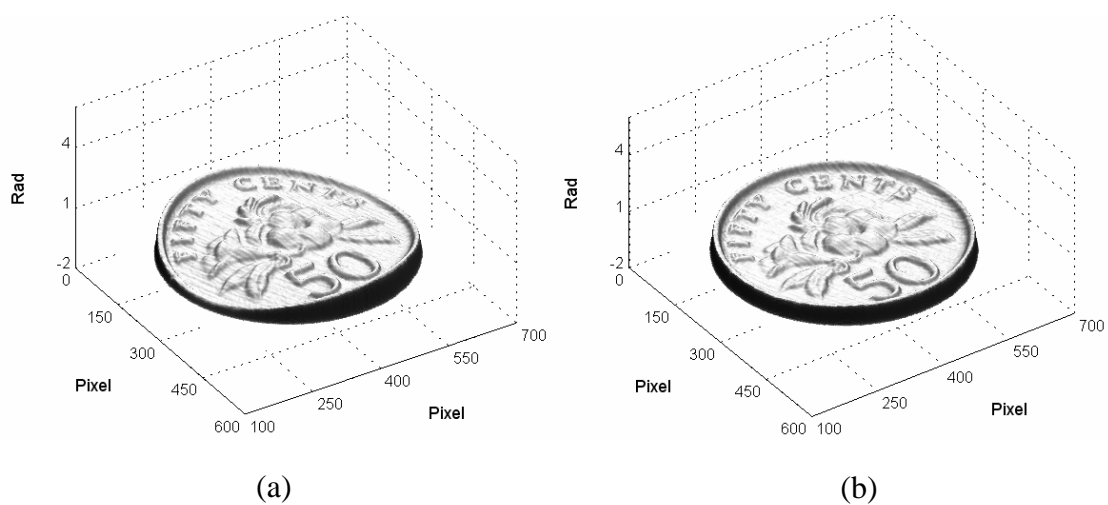


Fig. 5.45 Phase distribution after the removal of (a) a linear carrier;
(b) a carrier obtained by 2nd-order surface fitting.

In Fig. 5.46, measurement of section A-A (indicated in Fig. 5.44) obtained by the 2nd order surface-fitting method, linear carrier removal, and contact profiler are presented. The dashed line (linear carrier removal) shows large values at the center and small values at two sides. This indicates the residual carrier phase component remaining in the measured profile. Results of the 2nd order surface-fitting and the contact profiler agree in the overall distribution. However, the contact measurement shows larger values than the optical measurement in more than 80% data points. This could be due to the misalignment of the section measured by the contact profiler with the section on the optical image. For this particular specimen, the phase data for carrier-estimation are not confined to the base plane, since profile variations at other parts of the specimen are cancelled in the least squares process. This is an additional advantage of the proposed method, which also ensures a higher tolerance to random errors.

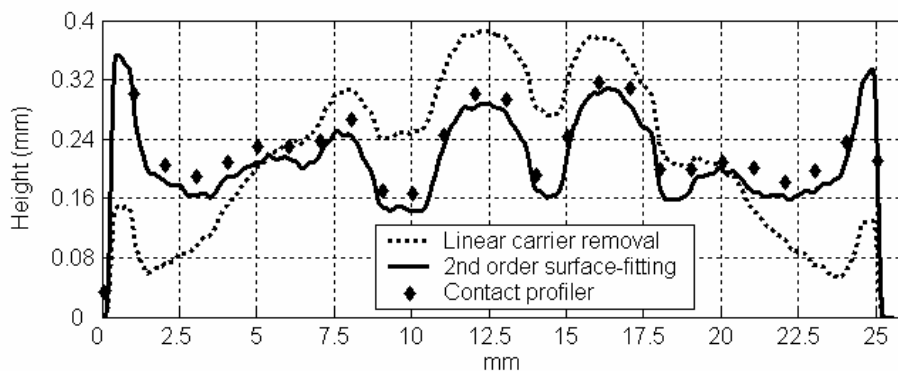


Fig. 5.46 Comparison of results obtained by 2nd order surface-fitting, linear carrier removal, and contact profiler

CHAPTER SIX

CONCLUSIONS AND RECOMMENDATIONS

This thesis mainly focuses on the optical phase evaluation techniques for fringe projection profilometry and digital speckle interferometry. It covers existing problems in three stages of optical fringe processing, namely wrapped phase extraction, phase quality identification, and post-processing of an unwrapped phase map.

A three-frame phase-shifting algorithm (with an unknown phase shift) and a sawtooth pattern profilometry method have been proposed. The three-frame algorithm can be used to reduce the phase-shifting steps in Carré's technique and this has been validated. A limitation of the method in its application on speckle pattern analysis is that the phase measurement accuracy is dependent on the phase shift. An optimal phase shift of 120° would result in accurate measurement. However, other values of phase shift would produce some system errors.

The novelty of the sawtooth pattern profilometry method lies in the fact that phase extraction is not dependent on the process of phase-shifting or Fourier transform as in conventional methods. Since only one frame sawtooth pattern is needed to retrieve an object profile, the method is useful for dynamic measurement. However, compared with phase-measuring profilometry (PMP), the proposed method is sensitive to projection shadow and the experimental setup need careful alignment to reduce defocus of the system.

In order to improve the reliability of the sawtooth pattern profilometry method, a phase quality criterion based on the least squares plane-fitting scheme is proposed. It

is found that, guided by the new criterion, the phase unwrapping process can bypass projection shadow and phase unwrapping errors are confined in small areas.

The limitation of conventional temporal fringe contrast (TFC) quality criterion is also studied. Although it is computationally effective in generating a TFC quality indicator, researchers realized that TFC is not suitable for detecting surface structure. In this thesis, a phase quality criterion based on the spatial fringe contrast (SFC) has been constructed. Results have shown that SFC is not only equally effective as TFC in detecting shadows, it is also able to identify fringe pattern changes due to an object profile variation. The superiority of SFC to TFC can be explained by referring to the schemes generating the two quality criteria. As TFC is generated by evaluating the phase shifted intensities of a pixel, the spatial connection between this pixel and its neighbors are not reflected. On the contrary, SFC is obtained by evaluating the neighborhood of a pixel and hence, it is able to detect the spatial structure. Another advantage of SFC is that the quality criterion is generated from one fringe pattern instead of several as for TFC. However, since SFC is more dependent on spatial intensities than TFC, the criterion requires relatively uniform illumination and surface reflectance. For this reason, it is suggested that high quality projection and imaging device be used for SFC-based shape measurement.

The phase evaluation study in relation to the fringe density has been focused on a common problem for many spatial filters. Based on the literature review, it is found that most spatial analysis techniques, such as the spatial noise filter, spatial correlation, and spatial phase extraction, rely on a priori selected parameter of the processing window (kernel) size. This parameter is related to the fringe density of a fringe pattern and is conventionally determined by subjective experience of an operator. In this thesis, an automatic fringe density estimation method is described. Simulated results have

demonstrated that the proposed algorithm is able to estimate the density distribution of a fringe pattern with additive noise. However, for a signal with multiplicative noise, pre-processing is required because multiplicative noise may severely distort a signal's probability function. The implication of the fringe density estimation method is far reaching. The density information can be incorporated into many spatial analysis algorithms to enhance their automation and achieve fully adaptive signal processing. The conventional concept of using a constant window size throughout the analysis of a fringe pattern could be innovatively updated to use an adaptive window size automatically determined by the local fringe density. This implies that optical data-processing software for industrial use may no longer rely on an experienced operator who needs long time training.

Lastly, in the post-processing of an unwrapped phase map, a generalized least squares approach for the removal of a nonlinear carrier is proposed. Though the theoretical development is based on fringe projection profilometry under a divergent illumination condition; the approach is generally applicable to various measurement geometries. The rigorous expression of the carrier function derived shows the theoretical viability of the series expansion analysis; but the implementation of the proposed method can be fully-automated by a computer program without the necessity of deriving the carrier function for a specific experimental setup. Compared with existing methods, the least squares approach simplifies the data-recording procedure, with relatively less manual intervention in data-processing, and ensures high tolerance to random errors. Hence, it shows high potential for practical phase evaluation applications. Although the present method does not directly address the issue of phase-to-height conversion, it could significantly facilitate a calibration process. With the elimination of the nonlinear carrier, the relationship between the phase and height

would be linear and therefore the calibration process is reduced to one of finding a linear translation coefficient for the phase-to-height conversion. This would lead to a great saving in time and effort.

In conclusion, this thesis has contributed significantly to the fundamental knowledge of several phase evaluation techniques. The algorithms described are validated with experiments and simulations. It is recommended that future work be carried out in improving the adaptability and reliability of the proposed techniques. Specifically, the following problems can be further investigated.

1. Accuracy enhancement for the sawtooth pattern profilometry method. Since only one frame sawtooth pattern is used for phase extraction, the accuracy of the proposed method is lower than PMP. In order to adapt the technique for actual industrial applications, the accuracy problem must be properly addressed.
2. The possibility of extracting SFC from a fringe pattern with nonlinear carrier. As presented in the theoretical development, the current SFC algorithm depends on a constant frequency of the carrier fringes. A more robust algorithm would be useful to extract SFC from nonlinear carrier fringes. This could probably be achieved through the series expansion approach used in the nonlinear carrier removal technique. If this is achieved, SFC would be able to completely replace TFC in guiding a phase unwrapping process.
3. The density estimation for signals with multiplicative noise. The proposed fringe density estimation method is only applicable to a fringe pattern with additive noise at the present stage. As a speckle fringe pattern is inherently corrupted by multiplicative noise, an improved algorithm could broaden the applications of fringe density estimation for speckle pattern analysis.

REFERENCES

1. Aebischer, H. A. and S. Waldner, A simple and effective method for filtering speckle-interferometric phase fringe patterns, *Opt. Comm.*, 162, pp. 205-210. 1999.
2. Baik, S. H., S. K. Park, C. J. Kim, and S. Y. Kim, Two-channel spatial phase shifting electronic speckle pattern interferometer, *Opt. Comm.*, 192, pp. 205-211. 2001.
3. Berryman, F., P. Pynsent, and J. Cubillo, A theoretical comparison of three fringe analysis methods for determining the three-dimensional shape of an object in the presence of noise, *Opt. Lasers Eng.* 39, pp. 35-50. 2003.
4. Bone, D. J., Fourier fringe analysis: the Two-dimensional phase unwrapping problem, *Appl. Opt.*, 30, pp. 3627-3632. 1991.
5. Brug, H. and P. A.A.M. Somers, Temporal phase unwrapping with two or four images per time frame: A comparison, *Proc. SPIE.* 3744, pp. 358-365. 1999.
6. Brug, H. V., Phase-step calibration for phase-stepped interferometry, *Appl. Opt.*, 38, pp. 3549-3555. 1999.
7. Burch, J. M. and J. M. J. Tokarski, Production of multi-beam fringes from photographic scatters, *Opt. Acta*, 15, pp. 101-111. 1968.
8. Butters, J. N. and J. A. Leendertz, Seckle pattern and holographic techniques in engineering metrology, *Opt. Laser Technol*, 3, pp. 26-30. 1971.
9. Butters, J. N., R. C. Jones, and C. Wykes, Electronic speckle pattern interferometry. In *Speckle Metrology*, Ed. R. K. Erf, Academic Press, New York, pp. 111-158. 1978.
10. Carré, P., Installation et utilisation du compateur photoelectrique et interferential du Bureau International des Poids et Mesures, *Metrologia*, 2, pp. 13-20 1966.
11. Chen, F., G. M. Brown, and M. Song, Overview of three-dimensional shape measurement using optical methods, *Opt. Eng.* 39, 10-22. 2000.
12. Chen, X., M. Gramaglia, and J. A. Yeazell, Phase-shift calibration algorithm for phase-shifting interferometry, *Opt. Soc. Am.*, 17, pp. 2061-2066. 2000.
13. Cheng, Y. Y. and J. C. Wyant, Phase shifter calibration in phase-shifting interferometry, *Appl. Opt.*, 24, pp. 3049-3052. 1985.

-
14. Cherbuliez, M., P. Jacquot, and X. Colonna de Lega, Wavelet processing of interferometric signals and fringe patterns, *Proc. SPIE.* 3813, pp. 692-702. 1999.
 15. Chu, T. C., W. F. Ranson, M. A. Sutton, and W. H. Peters, Application of Digital Image-Correlation Techniques to Experimental Mechanics, *Experimental Mech.*, 26, pp. 230-237. 1986.
 16. Creath, K., Phase-shifting speckle interferometry, *Appl. Opt.*, 24, pp. 3053-3058 1985.
 17. Creath, K., Temporal Phase Measurement Methods, In *Interferogram Analysis: Digital Fringe Pattern Measurement Techniques*, ed by D. W. Robinson and G. T. Reid, IOP Publishing, Ltd, pp. 94-140. 1993.
 18. Crimmins, T. R., Geometric filter for speckle reduction, *Appl. Opt.*, 24, pp. 1438-1443, 1985.
 19. Cuellar S. A. and D. M. Hernandez, Two-step phase-shifting algorithm, *Opt. Eng.* 42, pp. 3524-3531. 2003.
 20. Dainty, J. C. *Topics in Applied Physics Vol. 9, Laser Speckle and Related Phenomenon*. Berlin Heidelberg New York: Springer Verlag. 1975.
 21. Dainty, J. C., *Laser Speckle and Related Phenomenon* (2nd ed.). New York: Springer Verlag. 1984.
 22. Davila, A., D. Kerr, and G. H. Kaufmann, Digital processing of electronic speckle pattern interferometry addition fringes, *Appl. Opt.*, 33, pp. 5964-5969, 1994.
 23. Davila, A., G. H. Kaufmann, and D. Kerr, An evaluation of synthetic aperture radar noise reduction techniques for the smoothing of electronic speckle pattern interferometry fringes, *J. Mod. Opt.*, 42, pp. 1795-1804. 1995.
 24. Davila, A., G. H. Kaufmann, and D. Kerr, Scale-space filter for smoothing electronic speckle pattern interferometry fringes, *Opt. Eng.*, 35, pp. 3549-3554. 1996.
 25. Dirksen, D. X. Su, D. Vukicevic, and G. von Bally, Optimized phase shifting and use of phase modulation function for high resolution phase evaluation, In *Fringe'93, Proceedings of Second International Workshop on Automatic Processing of Fringe Patterns*, ed. By W. Juptner and W. Osten, Akademie, Berlin, pp. 148-153. 1993
 26. Durelli, A. J. and V. J. Parks, *Moiré analysis of strain*. Englewood Cliffs, N.J., Prentice-Hall. 1970.
 27. Fang, Q. and S. Zheng, Linearly coded profilometry, *Appl. Opt.* 36, pp. 2401-2407. 1997.
-

-
28. Federico, A. and G. H. Kaufmann, Comparative study of wavelet thresholding methods for denoising electronic speckle pattern interferometry fringes, *Opt. Eng.*, 40, pp. 2598-2604. 2001.
 29. Flynn, T. J., Consistent 2-D phase unwrapping guided by a quality map, *Proceedings of the 1996 International Geoscience and Remote Sensing Symposium*, Lincoln, NE, May 27-31, IEEE, Piscataway, NJ, pp. 2057-2059, 1996.
 30. Frost, V. S., J. A. Stiles, K. S. Shanmugan, and J.C. Holtman, A Model for Radar Images and Its Application to Adaptive Digital filtering of Multiplicative Noise, *IEEE. Trans. Pattern Analysis and Machine Intelligence*, 4, pp. 157-166. 1982,
 31. Gabor, D. A New microscopic principle, *Nature*, 161, pp. 777-778. 1948.
 32. Ganesan, A. R., D. K. Sharma, and M. P. Kothiyal, Universal digital speckle shearing interferometer, *Appl. Opt.*, 27, pp. 4731-4734. 1988.
 33. Ghiglia, D. C. and L. A. Romero, Robust two-dimensional weighted and unweighted phase unwrapping that uses fast transforms and iterative methods, *J. Opt. Soc. Am. A*, 11, pp. 107-117, 1994.
 34. Ghiglia, D. C. and D. Mark. *Two-Dimensional Phase Unwrapping*. New York: Wiley, 1998.
 35. Goldstein, R. M., H. A. Zebker, and C. L. Werner, Satellite radar interferometry: two-dimensional phase unwrapping. *Radio Science*, 23, pp. 713-720. 1988.
 36. Goodman, J. W. Statistical properties of laser speckle patterns. In *Topics in Applied Physics*, Vol 9, *Laser Speckle and Related Phenomena*, ed by J. C. Dainty, pp. 9-75. Berlin; New York: Springer-Verlag. 1975.
 37. Greivenkamp, J. E., Generalized data reduction for heterodyne interferometry, *Opt. Eng.* 23, pp. 350-352. 1984.
 38. Hariharan, P., B. F. Oreb, and T. Eiju, Digital phase-shifting interferometry: a simple error-compensating phase calculation algorithm, *Appl. Opt.* 26, pp. 2504-2506. 1987.
 39. Hearn, E. J. *Photoelasticity*. Watford, Merrow Publishing Co. ltd., 1971.
 40. Hecht, E. *Optics* (4th ed.). Reading, Mass: Addison-Wesley, 2002.
 41. Huang, P. S., Q. Hu, F. Jin, and F. P. Chiang, Color-encoded digital fringe projection technique for high-speed three-dimensional surface contouring. *Opt. Eng.* 38, pp. 1065-1071 1999.
 42. Hung, Y. Y. A Speckle-Shearing Interferometry: A Tool For Measuring Derivatives of Surface Displacements, *Opt. Comm.*, 11, pp. 132-135. 1974.
-

-
43. Hung, Y. Y., Shearography: a novel and practical approach to nondestructive testing, *J. Nondestruct. Eval.*, 8, 55-68, 1989.
 44. Huntley J. M. and J. R. Buckland, Characterization of sources of 2π phase discontinuity in speckle interferograms, *J. Opt. Soc. Am. A*, 12, pp. 1990-1996. 1995.
 45. Idesawa, M., T. Yatagai, and T. Soma, Scanning moire method and automatic measurement of 3-D shapes, *Appl. Opt.* 16, pp. 2152-2162. 1977.
 46. Jambunathan, K., L. S. Wang, B. N. Dobbins, and S. P. He, Semi-automatic phase shift calibration using digital speckle pattern interferometry, *Opt. Laser Tech.*, 27, pp. 145-151. 1995.
 47. Joenathan, C. and B. M. Khorana, Phase-measuring fiber optic electronic speckle pattern interferometer: phase step calibration and phase drift minimization, *Opt. Eng.*, 31, pp. 315-321. 1992.
 48. Joenathan, C. Phase-measuring interferometry: new methods and error analysis, *Appl. Opt.* 33, pp. 4147-4155. 1994
 49. Judge, T. R. and P. J. Bryanston-Cross, A review of phase unwrapping techniques in fringe analysis, *Opt. Lasers Eng.*, 21, pp. 199-239. 1994.
 50. Kao, C. C., G. B. Yeh, S. S. Lee, C. K. Lee, C. S. Yang, and K. C. Wu, Phase-shifting algorithms for electronic speckle pattern interferometry, *Appl. Opt.*, 41, pp. 46-54, 2002.
 51. Kaufmann, G. H., A. Davila, and D. Kerr, Speckle noise reduction in TV holography. In *Second Iberoamerican Meeting on Optics*, Pro. SPIE 2730, pp. 96-100, 1995.
 52. Kerr, D., F. M. Santoyo, and J. R. Tyrer, Manipulation of the Fourier components of speckle fringe patterns as part of an interferometric analysis process, *J. Mod. Opt.*, 36, pp. 195-203. 1989.
 53. Kerr, D., F. M. Santoyo, and J. R. Tyrer, Extraction of phase data from electronic speckle pattern interferometric fringes using a single-phase-step method: a novel approach, *J. Opt. Soc. Am. A*, 7, pp. 820-826. 1990.
 54. Kozlowski, J. and G. Serra, A novel complex phase tracing (CPT) method for fringe pattern analysis with reduced phase errors. In: J. Uptner W, editor. *Fringe 97, Workshop on Automatic Processing of Fringe Patterns*. Berlin: Akademie Verlag, 1997.
 55. Kreis, T. Digital holographic interference-phase measurement using the Fourier-transform method, *J. Opt. Soc. Am. A*, 3, pp. 847-855. 1986.
-

-
56. Kujawinska, M. Spatial Phase Measurement Methods, In *Interferogram Analysis: Digital Fringe Pattern Measurement Techniques*, ed by D. W. Robinson and G. T. Reid, IOP Publishing, Ltd, pp. 94-140. 1993.
 57. Kwon, O. Y., Advanced wavefront sensing at Lockheed, In *Interferometric Metrology*, ed. by N. A. Massie, Proc. SPIE 816, 196–211. 1987.
 58. Lee, J. S., Speckle suppression and analysis for synthetic aperture radar images, *Opt. Eng.*, 25, pp. 636-643. 1986.
 59. Leendertz, J. A. and J. N. Butters, An Image-Shearing Speckle Pattern Interferometer for Measuring Bending Moments, *J. Phys. E Scientific Instr.* 6, pp. 1107-1110. 1973.
 60. Lehman, M. Speckle Statistics in the Context of Digital Speckle Interferometry, In *Digital speckle pattern interferometry and related techniques*, ed by P. K. Rastogi. pp. 1-58. John Wiley & Sons, Ltd., 2001
 61. Li, J. F., X. Y. Su, and L. R. Gou, An improved Fourier transform profilometry for automatic measurement of 3-D object shapes, *Opt. Eng.* 29, pp. 1439-1444. 1990.
 62. Li, J. F. and X. Y. Su, Two-dimensional Fourier transform profilometry for the automatic measurement of three-dimensional object shapes, *Opt. Eng.* 34, pp. 3297-3302. 1995.
 63. Li, J. L., X. Y. Su, H. J. Su, and S. S. Cha, Removal of carrier frequency in phase-shifting techniques, *Opt. Lasers Eng.* 30, pp. 107-115. 1998.
 64. Li, W. and X. Y. Su, Phase unwrapping algorithm based on phase fitting reliability in structured light projection, *Opt. Eng.*, 41, pp. 1365-1372. 2002.
 65. Lim, H, W. Xu, and X. Huang Two new practical methods for phase unwrapping, *Proceedings of the 1995 International Geoscience and Remote Sensing Symposium*, Tokyo, Japan, IEEE, Piscataway, pp. 196-198. 1995.
 66. Liu, H., A. N. Cartwright, and C. Basaran, Sensitivity improvement in phase-shifted moiré interferometry using 1-D continuous wavelet transform image processing, *Opt. Eng.*, 42, pp. 2646-2652. 2003.
 67. Malacara, D. *Optical shop testing* (2nd ed.). New York: Wiley. 1991.
 68. Mallat, S., *A wavelet tour of signal processing*, Academic Press, San Diego, 1999.
 69. Marklund, O. Robust fringe density and direction estimation in noisy phase maps, *J. Opt. Soc. Am. A*, 18, pp. 2717-2727. 2001.
-

-
70. Marroquin, J. L. R. Rodriguez-Vera, and M. Servin, Adaptive quadrature filters and the recovery of phase from fringe pattern images, *J. Opt. Soc. Am. A.* 14, pp. 1742-1753. 1997.
 71. Marroquin, J. L. R. Rodriguez-Vera, and M. Servin, Local phase from local orientation by solution of a sequence of linear systems, *J. Opt. Soc. Am. A.* 15, pp. 1536-1544. 1998.
 72. Marroquin, J. L., M. Rivera, S. Botello, R. Rodriguez-Vera, and M. Servin, Regularization methods for processing fringe-pattern images, *Appl. Opt.* 38, pp. 788-794. 1999.
 73. McKechnie, T. S. Speckle reduction. In *Topics in Applied Physics, Vol 9, Laser Speckle and Related Phenomena*, ed by J. C. Dainty, pp. 123-170. Berlin; New York: Springer-Verlag. 1975.
 74. Morgan, C. J., Least-squares estimation in phase-measurement interferometry, *Optics Letters*, 7, pp. 368-370. 1982.
 75. Nakadate, S. and H. Saito, Fringe scanning speckle-pattern interferometry, *Appl. Opt.*, 24, pp. 2172-2180, 1985.
 76. Novak, J., Five-step phase-shifting algorithms with unknown values of phase shift, *Optik*, 114, pp. 63-68. 2003.
 77. Ochoa, N. A. and J. M. Huntley, Convenient method for calibrating nonlinear phase modulators for use in phase-shifting interferometry, *Opt. Eng.*, 37, pp. 2501-2505. 1998.
 78. Pavageau, S., R. Dallier, N. Servagent, and T. Bosch, A new algorithm for large surfaces profiling by fringe projection, *Sensors and Actuators A* 115, pp. 178-184. 2004.
 79. Pfister, B. P., *Speckle interferometric mit neuen Phasenschiebemethoden*, PhD. Thesis, Universitat Stuttgart 18, 1993.
 80. Pritt, M. D., Phase unwrapping by means of multigrid techniques for interferometric SAR, *IEEE Transactions on Geoscience and Remote Sensing*, 34, pp. 728-738. 1996.
 81. Quan, C., X. Y. He, C. F. Wang, C. J. Tay, and H. M. Shang, Shape measurement of small objects using LCD fringe projection with phase shifting, *Opt. Comm.* 189, pp. 21-29. 2001.
 82. Quan, C., C. J. Tay, X. Y. He, X. Kang, H. M. Shang, Microscopic surface contouring by fringe projection method, *Optics & Laser Technology*, 34, pp. 547-552. 2002.
 83. Quiroga, J. A., A. Gonzalez-Cano, and E. Bernabeu, Phase-unwrapping algorithm based on an adaptive criterion, *Appl. Opt.*, 34, pp. 2560-2563. 1995.
-

- 84. Rastogi, P. K. Digital speckle pattern interferometry and related techniques, John Wiley & Sons, Ltd., 2001.
- 85. Robinson, D. W. and D. C. Williams, Digital phase stepping speckle interferometry, *Opt. Comm.*, 57, pp. 26-30. 1986.
- 86. Rodriguez-Vera, R. and M. Servin, Phase locked loop profilometry, *Opt. Laser Tech.* 26, pp. 393–398. 1994.
- 87. Roth, M. W., Phase unwrapping for interferometric SAR by the least-error path, Johns Hopkins University Applied Physics Lab Technical Report, Laurel, MD, March 30, 1995.
- 88. Ruiz, P. D. and G. H. Kaufmann, Evaluation of a scale-space filter for speckle noise reduction in electronic speckle pattern interferometry, *Opt. Eng.*, 37, pp. 2395-2401. 1998.
- 89. Salas, L., E. Luna, J. Salinas, V. Garcia, and M. Servin, Profilometry by fringe projection, *Opt. Eng.* 42, pp. 3307-3314. 2003.
- 90. Santoyo, F. M., D. Kerr, and J. R. Tyrer, Interferometric fringe analysis using a single phase step techniques, *Appl. Opt.*, 27, pp. 4362-4364, 1988.
- 91. Schmitt, D. R. and R. W. Hunt, Optimization of fringe pattern calculation with direct correlations in speckle interferometry, *Appl. Opt.*, 36, pp. 8848-8857, 1997.
- 92. Schwider, J., R. Burow, K. E. Elssner, J. Grzanna, R. Spolaczyk, and K. Merkel, Digital wave-front measuring interferometry: some systematic error sources, *Appl. Opt.*, 22, pp. 3421-3432. 1983.
- 93. Servin, M., J. L. Marroquin, and F. J. Cuevas, Demodulation of a single interferogram by use of a two-dimensional regularized phase-tracking technique, *Appl. Opt.* 36, pp. 4540-4548. 1997.
- 94. Servin, M., J. L. Marroquin, and F. J. Cuevas, Fringe-follower regularized phase tracker for demodulation of closed-fringe interferograms, *J. Opt. Soc. Am. A*, 18, pp. 689-695. 2001.
- 95. Sesselmann, M. and G. A. J. Albertazzi, Single phase-step algorithm for phase difference measurement using ESPI, *Proc. SPIE.* 3478, pp. 153-159. 1998.
- 96. Sjudahl, M. and P. Synnergren, Measurement of shape by using projected random patterns and temporal digital speckle photography, *Appl. Opt.* 39, pp. 1990-1997. 1999.
- 97. Srinivasan, V., H. C. Liu, and M. Haliou, Automated phase-measuring profilometry of 3-D diffuse objects. *Appl. Opt.* 23, pp. 3105-3108. 1984.

-
98. Srinivasan, V., H. C. Liu, and M. Halioua, Automated phase-measuring profilometry: a phase mapping approach, *Appl. Opt.* 24, pp. 185-188. 1985.
 99. Stephenson, P., D. R. Burton, and M. I. Lalor, Data validation techniques in a tiled phase unwrapping algorithm, *Opt. Eng.*, 33, pp. 3703-3708. 1994.
 100. Strobel, B., Processing of interferometric phase maps as complex-valued phasor images, *Appl. Opt.*, 35, pp. 2192-2198. 1996.
 101. Su. X. Y., M. R. Sajan, and A. Asundi, Fourier transform profilometry for 360-degree shape using TDI camera. In *Proc. International Conference on Experimental Mechanics Advances and Applications*, December 1996, Singapore.
 102. Takeda, M., H. Ina, and S. Kobayashi, Fourier-transform method of fringe-pattern analysis for computer-based topography and interferometry, *J. Opt. Soc. Am.*, 72, pp. 156-160. 1982.
 103. Takeda, M. and K. Mutoh, Fourier transform profilometry for the automatic measurement of 3-D object shapes, *Appl. Opt.*, 22, pp. 3977-3982. 1983.
 104. Takeda, M., Q. Gu, M. Kinoshita, H. Takai, and Y. Takahashi, Frequency-multiplex Fourier-transform profilometry: a single-shot three-dimensional shape measurement of objects with large height discontinuities and/or surface isolations, *Appl. Opt.* 36, pp. 5347-5354. 1997.
 105. Toyooka, S. and M. Tominaga, Spatial fringe scanning for optical phase measurement, *Opt. Comm.* 51, pp. 68-70. 1984.
 106. Toyooka, S. and Y. Iwaasa, Automatic profilometry of 3-D diffuse objects by spatial phase detection, *Appl. Opt.* 25, pp. 1630-1633. 1986.
 107. Varman, P. and C. Wykes, Smoothing of speckle and moiré fringes by computer processing, *Opt. Lasers Eng.* 3, pp. 87-100. 1982.
 108. Vetterling, W. T., W. H. Press, S. A. Teukolsky, and B. P. Flannery, *Numerical Recipes Example Book (C++)*. 2nd, Cambridge, New York: Cambridge University Press, 2002.
 109. Villa, J., M. Servin, and L. Castillo, Profilometry for the measurement of 3-D object shapes based on regularized filters, *Opt. Comm.* 161 pp. 13-18. 1999.
 110. Witkin, A. P., Scale-space filtering, In *Proc. Int. Joint Conf. on Artificial Intelligence*, pp. 1019-1022, Karlsruhe, German. 1983.
 111. Wyant, J. C., B. F. Oreb, and P. Hariharan, Testing aspherics using two-wavelength holography: use of digital electronic techniques, *Appl. Opt.* 23, pp. 4020-4023. 1984.
 112. Xu, W. and I. Cumming, A region growing algorithm for InSAR phase unwrapping, *Proceedings of the 1996 International Geoscience and Remote*
-

- Sensing Symposium, Lincoln, NE, May 27-31, IEEE, Piscataway, NJ, pp. 2044-2046. 1996.
113. Xu, Y. and C. Ai, Simple and effective phase unwrapping technique, Interferometry IV: Techniques and Analysis, Proc. SPIE, 2003, Society of Photo-Optical Instrumentation Engineers, Bellingham, WA, pp. 254-263. 1993.
114. Zhi, H. and R. B. Johansson, Adaptive filter for enhancement of fringe patterns, Opt. Lasers Eng. 15, pp. 241-251. 1991.
115. Zhou, W. S. and X. Y. Su, A direct mapping algorithm for phase-measuring profilometry, J. Mod. Opt, 41, pp. 89-94. 1994.

APPENDICES

Appendix A. C++ source code for N th-order surface-fitting

The partial derivative equations of the error function in Eq. (3.50) can be written in a matrix form, similar as that in Eq. (3.49).

$$\mathbf{X}_{[(N+1)(N+2)/2] \times [(N+1)(N+2)/2]} \cdot \mathbf{A}_{[(N+1)(N+2)/2] \times 1} = \mathbf{B}_{[(N+1)(N+2)/2] \times 1} \quad (\text{A1})$$

where \mathbf{X} is the matrix composed of the product of x^{px} and y^{py} (px and py represent the power of x and y , respectively); \mathbf{A} is the vector of unknowns; and \mathbf{B} is the vector containing the product of x^{px} or y^{py} with the experimentally obtained phase data $\phi_{r,\text{exp}}(x, y)$.

As each element of \mathbf{X} carries the form of $x^{px} y^{py}$, the C++ source code begins with such a function that calculates the product $x^{px} y^{py}$ for given x , y , px , and py .

```
float fxy(float x, float y, int px, int py)
{
    return( pow(x, px)*pow(y, py) );
}
```

where `pow(x, px)`, a math function of C++, calculates x^{px} .

The main function for the surface-fitting incorporates a standard numerical analysis method for solving linear equations (Vetterling et al, 2002). Given a matrix \mathbf{X} and a vector \mathbf{B} , the function `NR::gaussj(...)` calculates the corresponding solutions and return them in each element of \mathbf{B} . Therefore, one only need prepare the elements of \mathbf{X} and \mathbf{B} based on the input data. There are six inputs for the function `Surfacefitting(...)`. The `Dx`, `Dy` and `Dz` are data arrays containing values of x , y and $\phi_{r,\text{exp}}(x, y)$, respectively. The variable “size” is the size of `Dx`, `Dy` and `Dz`; and it tells

the function the number of data points used for surface-fitting. The array **A** is the solution vector. The constant N defines the order of curve surface-fitting.

```
bool Surfacefitting(float *Dx, float *Dy, float *Dz, int size, float *A, const int N)
{
    // "num" is the number of unknowns.
    int i, j, s, power, c, num=(N+1)(N+2)/2;
    /* if the number of data points (size) is less than the number of unknowns
    (num), the linear equations cannot be solved. */
    if(size<num) return false;
    valarray<int> px(num), py(num);          // Power of  $x$  and  $y$ , respectively.
    Mat_IO_DP X(num,num), B(num,1);        // Matrix X and vector B
    for(c=power=0, i=0; i<num; i++, c++)    // Fill in the power of  $x$  and  $y$ .
    {
        if(c>power)
        {
            c=0;
            power++;
        }
        px[i]=c;
        py[i]=power-c;
    }
    for(j=0; j<num; j++)                    // Fill in the matrix X and the vector B
    {
        for(i=0; i<num; i++)
            for(X[j][i]=0, s=0; s<size; s++)
                X[j][i]+=fxy(Dx[s], Dy[s], px[j]+px[i], py[j]+py[i]);
        for(B[j][0]=0, s=0; s<size; s++)
            B[j][0]+=Dz[s]*fxy(Dx[s], Dy[s], px[j], py[j]);
    }
    NR::gaussj(X, B);                       // Calculate solutions of the linear equations
    for(j=0; j<num; j++) A[j]=B[j][0];      // Put the solution in the vector A
    return true;
}
```

After surface-fitting, one can use the function `CarrierPhase(..)` to retrieve a carrier phase value at point (x, y) .

```
float CarrierPhase( int x, int y, float *A, const int N)
{
    // "num" is the number of unknowns.
    int i, j, s, power, c, num=(N+1)(N+2)/2;
    valarray<int> px(num), py(num);          // Power of x and y, respectively.
    float phase=0;                          // carrier phase value
    for(c=power=0, i=0; i<num; i++, c++)    // Fill in the power of x and y.
    {
        if(c>power)
        {
            c=0;
            power++;
        }
        px[i]=c;
        py[i]=power-c;
    }
    for(i=0; i<num; i++) phase+=A[i]*fxy(x,y,px[i],py[i]);
    return phase;
}
```

Appendix B. List of publications

Journal papers:

1. Lujie Chen, Cho Jui Tay, "Carrier phase component removal: a generalized least squares approach", *Journal of the Optical Society of America A*, 23, 435-443, (2006).
2. Lujie Chen, Chenggen Quan, "Fringe projection profilometry with non-parallel illumination: a least squares approach", *Optics Letters*, 30, 2101-2103, (2005).
3. Lujie Chen, Chenggen Quan, Cho Jui Tay, Yuanhao Huang, "Fringe contrast-based 3D profilometry using fringe projection", *Optik*, 116, 123-128, (2005).
4. Lujie Chen, Chenggen Quan, Cho Jui Tay, Yu Fu, "Shape measurement using one frame projected sawtooth fringe pattern", *Optics Communications*, 246, 275-284, (2005).
5. Chenggen Quan, Cho Jui Tay, Lujie Chen, "Fringe-density estimation by continuous wavelet transform", *Applied Optics*, 44, 2359-2365, (2005).
6. Cho Jui Tay, Chenggen Quan, Lujie Chen, "Phase retrieval with a three-frame phase-shifting algorithm with an unknown phase shift", *Applied Optics*, 44, 1401-1409, (2005).
7. Cho Jui Tay, Chenggen Quan, Lujie Chen, Yu Fu, "Phase extraction from electronic speckle patterns by statistical analysis", *Optics Communications*, 236, 259-269 (2004).
8. Chenggen Quan, Cho Jui Tay, Lujie Chen, Yu Fu, "Spatial-fringe-modulation-based quality map for phase unwrapping", *Applied Optics*, 42, 36, 7060-7065 (2003).

Conference papers:

9. Lujie Chen, Chenggen Quan, Cho Jui Tay, "Simplified Carré's method for phase extraction", *The 3rd International Conference on Experimental Mechanics*, 29, Nov. – 1, Dec. 2004, Singapore.

10. Lujie Chen, Chenggen Quan, Cho Jui Tay, “Fringe-projection-technique-oriented phase quality maps for phase unwrapping”, The 3rd International Symposium on Instrumentation Science and Technology, 18~22, Aug. 2004, Xi'an, China.
11. Lujie Chen, “Six-frame phase extraction algorithm for speckle patterns”, The 5th APRU Doctoral Students Conference, 9 - 13, Aug. 2004, Sydney, Australia.
12. Lujie Chen, Chenggen Quan, Cho Jui Tay, Yu Fu, “Phase shifting technique for closed-fringe analysis by Fourier transform method”, International Conference on Advanced Technology in Experimental Mechanics 2003, 10-12, Sep. 2003, Nagoya, Japan.